Università degli Studi dell'Insubria
Corso di Dottorato in Fisica - XIII Ciclo

Silicon Photomultipliers: characterization and application to Fluorescence Flucturation Spectroscopy

Author:
Marco Ramilli

Supervisor:
Prof. Massimo Caccia

Contents

List of Figures

List of Tables

Chapter 1

Introduction and outline

Among the wide-ranged zoology of silicon-based detectors (see for exemple [1]), a relatively novel class of devices called Silicon Photomultipliers (SiPMs henceover) gained importance in the last years. It had been originally invented in Russia [2] and the basic schematism of the device consists in an array of identical semiconductor diodes, working at high reverse bias, over the breakdown voltage, in a geiger-Müller regime. Each diode is indipendent from the others, but they all share a common output, so that the output current is proportional to the number of Geiger-Müller (sometimes in the text G-M) avalanches triggered. The SiPM construction technology grants them many features, as a rigorous linearity, gain values comparable to standard Photo-Multiplier Tubes, operability in magnetic fields, compactness, limited power consumption.
Thus, in these years, many fields of experimental physics looked at these devices with increasing attention.

In order to bring just a few exemples, it is worth mentioning that the first group in the high energy particle physics to consider the use of SiPM was the CALICE (CAlorimeter for the LInear Collider Experiment) group within the International Linear Collider collaboration [3] [4]: the aim is to produce a high-granularity calorimeter, in order to measure the details of an hadron shower, combining energy information with tracking information.
In the CMS at the Large Hadron Collider, due to the presence of an intense magnetic field within the solenoid, standard PMTs cannot operate. Thus, the use of SiPMs coupled with scintillating matherial for the upgrade of the experiment is under study [5] [6].
In medical physics blue sensive SiPMs are gaining importance, expecially as part of an innovative detecting technology in PET machines [7], [8]and axial PET [9].
In astrophisics, next generation of Cherenkov Array Telescopes are considering the use of SiPMs as possible candidates for the photo-detection component (see the design concepts [10])

The thesis originates from and develops around the SiPM technology.
Starting from the need for a characterization protocol, which arose within the RAPSODI[1] project (which will be described with more detail in Chapter 4), the first aim consisted in providing an exhaustive characterization protocol for SiPMs and a phenomenological model for their response.
Subsequentely, faseability studyes have been conducted on the performances of SiPMs as detectors in the biophysical techniques of Fluorescence Fluctuation Spectroscopy. In such experiments, proteins are ligated with fluorophores with decay time of the order of few nanoseconds and illuminated with pulsed laser light: informations about the parameters of the system under observation are obtained from the study of the fluctuation of the fluorescence intensity; the use SiPMs, which are endowed with both a sub-nanosecond temporal resolution and a high photon number resolution capabilities, could constitute an improvement of the experimental conditions, provided a consistent modelization of their response.

The thesis is organized as follows:

- in Chapter 2 basic principles of semiconductor devices physics will be recalled: attention will be focused on models descibing impact ionization and avalanche generation;
- in Chapter 3, Photo-Detection Efficiency, Gain and the other principal figures of merit used to describe SiPM performances will be introducted;
- the need for characterization of SiPM performances will be made explicit in Chapter 4, and principal results, with a particular attention to the characterization of the temperature behaviour will be presented;
- going further on the phenomenological description of SiPM response, a statistical model including crosstalk and dark count rate contribution will be presented in Chapter 5;
- therefore, in Chapter 6 a general introduction of the Fluorescence Fluctruation Spectroscopy techniques will be held, providing the background information for the Chapter 7, where results of application of SiPMs to Photon Counting Histogram will be presented.

[1] a European founded project, which had the aim of developing three innovative radiaton detection sensor, using the SiPM technology

Chapter 2

Are you experienced?

In this chapter, the essential properties of doped semiconductors will be recalled, with the aim to outline a first general sketch of the physical principles behind the operation of Silicon Photomultipliers (SiPMs hereafter).
In particular, after a brief introduction on intrinsic and extrinsic semiconductors, the chapter will focus on the properties of a highly reverse biased $p-n$ junction, providing a description of the *avalanche breakdown process*, which is the core of the SiPM concept.

2.1 General Properties of Semiconductors

2.1.1 Intrinsic semiconductors

Solid state matter with crystal structure can be described like a lattice of atoms[1]; in this model, the energy levels are N-fold degenerate (where N is the number of atoms forming the lattice), splitting into N different closely spaced energy levels, so that for extremely large N the separation between two adjacent levels becomes negligible: these structures are commonly addressed as *energy bands*; the energy level of the valence electrons form the so called *valence band*, while the immediately higher level degenerate into the *conduction band* and the difference between the the energy E_C of the bottom of the conduction band and the energy E_V of the top of the valence band is called *energy gap* corresponding to $E_G = E_C - E_V$.

If, for whatsoever reason, an electron in valence band gains enough energy to pass the energy gap, moves to conduction band, leaving behind a vacancy or a *hole*, as schematically depicted in Figure 2.1. For many puropses, electrons in conduction band and holes in valence band can be described as respectively negative and positive free particles with effective mass m_n and m_p.
The number of these free carriers in a semiconductor with very few impurities (called intrinsic semiconductor) can be extimated relying on the Fermi-Dirac

[1] For a more detailed description see fundamental textbooks, as Lutz [11] or Sze [12]

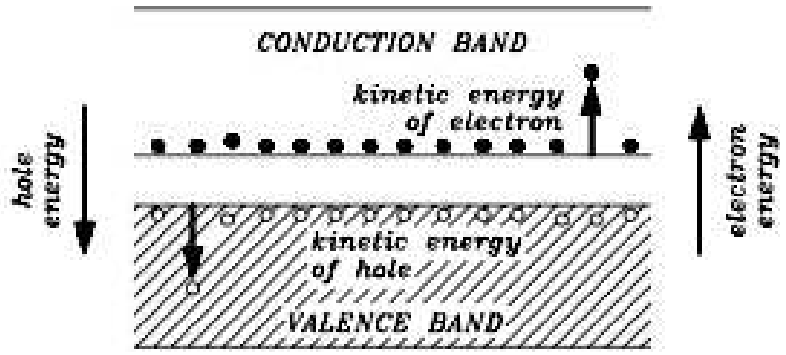

Figure 2.1: Pictorial view of the energy band in a semiconductor for electrons and holes[11].

function, which regulates the occupation probability for an electronic state:

$$F(E) \;=\; \frac{1}{1 \;+\; \exp\left(\frac{E-E_F}{k_B \cdot T}\right)}, \tag{2.1}$$

where E_F is the Fermi energy, defined as the energy corresponding to a level whith occupation probability of one half, k_B is the Boltzmann constant and T the absolute temperature.
If E_F is within the band gap and distant enough from the considered energy levels, such an expression can be approximated as

$$F_n(E) \;\approx\; \mathrm{e}^{-\frac{E-E_F}{k_B \cdot T}} \tag{2.2}$$

for the electrons and

$$F_p(E) \;=\; 1 \;-\; F(E) \approx \mathrm{e}^{-\frac{E_F-E}{k_B \cdot T}} \tag{2.3}$$

for the holes.

The density of states in each band can be obtained by the standar quantization using static waves in a unit of volume, obtaining

$$N(E_{kin})\mathrm{d}E_{kin} \;=\; 4\pi \left(\frac{2m}{h^2}\right)^{3/2} \; E_{kin}^{1/2}\mathrm{d}E_{kin}, \tag{2.4}$$

where h is the Planck's constant and m stands for the effective mass of the particle under considaration.
Integrating the probability distribution expressed in Equations 2.2 and 2.3 over

the energy bands using 2.4, the carrier density are obained, for electrons and holes respectively:

$$n = 2\left(\frac{2\pi m_n k_B T}{h^2}\right)^{3/2} \mathrm{e}^{-\frac{E_C - E_F}{k_B T}} = N_C \mathrm{e}^{-\frac{E_C - E_F}{k_B T}} \tag{2.5}$$

$$p = 2\left(\frac{2\pi m_p k_B T}{h^2}\right)^{3/2} \mathrm{e}^{-\frac{E_F - E_V}{k_B T}} = N_V \mathrm{e}^{-\frac{E_F - E_V}{k_B T}}, \tag{2.6}$$

where N_C and N_V are the effective density of states in the conduction and valence band respectively. The espression obtained from the product of the two carrier concentrations depends on the band energy gap $E_G = E_C - E_V$, being $n \cdot p = N_C N_V \mathrm{e}^{-\frac{E_C - E_V}{k_B T}}$.
It is useful calculating explicitly the Fermi energy level E_I for a intrinsic semiconductor and its carrier densities; with a negligible amount of impurities, their density should be the same: so setting $n = p = n_I$:

$$n_I = \sqrt{N_C N_V}\mathrm{e}^{-\frac{E_G}{2k_B T}} \tag{2.7}$$

and, using 2.5 and 2.6,

$$E_I = \frac{E_C + E_V}{2} + \frac{3k_B T}{4} \ln\left(\frac{m_p}{m_n}\right); \tag{2.8}$$

this energy level presents a deviation from the middle of the band gap, due to the difference in effective mass of the electron and the holes.

2.1.2 Extrinsic Semiconductors

In practice, intrinsic semiconductors are rarely used, since it is much more convenient to alter the properties of these materials by adding small fractions of specific impurities: this procedure is called *doping*.
If impurities possess one more valence electron in respect to the crystal atoms (e.g. adding As atoms in a Si crystal) the elctron which is not used for the valence bonding is free for conduction, thus obtaining an n-type semiconductor; on the other side, the crystal can be doped with atoms with one less valence electron (e.g. B in a Si crystal): as a result, one electron is missing in the covalent bond creating a hole, thus obtaining a p-type semiconductor.
In the band model, the presence of these impurities locally originates extra energy levels within the band gap, which can be of the donor type (E_D), in case of n-type doping, or acceptor (E_A), in case of p dopant.
Consequentely, dopants are chosen so that free carrier generation is made more probably than in the intrinsic semiconductor:

- E_D levels are such that $E_C - E_D \ll E_G$ and they are full of valence electrons of the donor atoms: in this situation, these electrons can easily pass in conduction band;

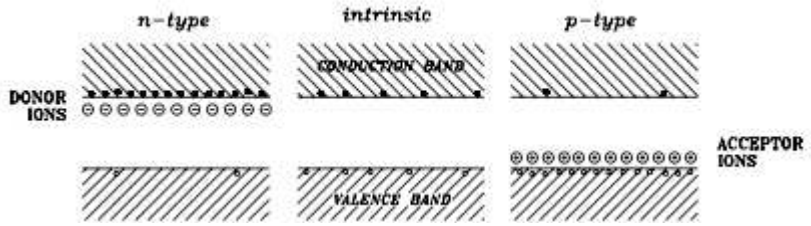

Figure 2.2: Simple schematics of the energy band representation of a n-doped semiconductor (left), a p-doped semiconductor (right), compared with an intrinsic semiconductor (middle); the picture had been taken from [11].

- E_A levels, instead, are empty levels very close to the valence band (i.e. $E_A - E_V \ll E_G$): in this case valence electrons of the crystal can easly pass in these levels, thus creating a hole in valence band.

This situation can be described by a shift of the Fermi level E_F from the intrinsic level E_I upward to the conduction band or downward to the valence band, respectively in the case of the n-type and of the p-type doping. Up to fairly high doping concentations, the respective Fermi energy levels can be obtained from Equations 2.5 and 2.6, by setting the respective carrier concentration equal to the donor (N_D) or acceptor (N_A) concentrations:

$$E_C - E_F = k_B T \ln\left(\frac{N_C}{N_D}\right) \tag{2.9}$$

$$E_F - E_V = k_B T \ln\left(\frac{N_V}{N_A}\right). \tag{2.10}$$

Therefore, Equations 2.5 and 2.6 can be rewritten, with the help of equation 2.7, into:

$$n = n_I \mathrm{e}^{\frac{E_F - E_I}{k_B T}} \tag{2.11}$$

$$p = n_I \mathrm{e}^{\frac{E_I - E_F}{k_B T}}. \tag{2.12}$$

These two equations, combined, state that an increase of majority carriers, is accompanied by a decrease of minority carriers, according to the following mass-action law:

$$n \cdot p = n_I^2. \tag{2.13}$$

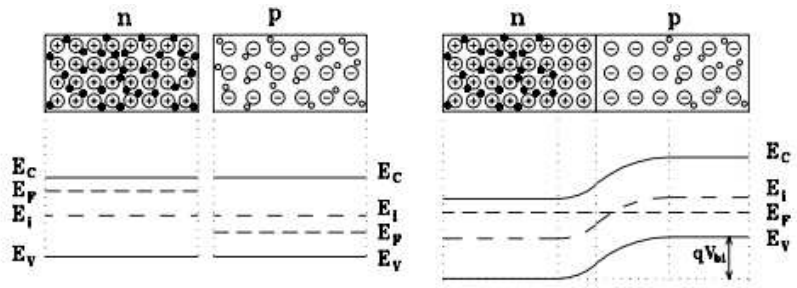

Figure 2.3: Band representation of a $p-n$ juntion at thermal equilibrium: on left energy bands for separated extrinsic n and p doped semiconductor are schematically depicted; on the right, the energy bands when the two parts are brought together; the picture had been taken from [11].

2.2 The $p-n$ junctions

One of the most relevant application of extrinsic semiconductors is the so called $p-n$ junction, a structure obtained by joining together opposite doped semiconductors.
To understand the physics of these device, a first description of the behaviour of this structure at the equilibrium will be provided, the under different biasing conditions.

2.2.1 A $p-n$ junction at the equilibrium

When two homogenuosly doped p and n regions, electrically neutral and at the equilibrium are brought into contact, electrons start to diffuse into the p region recombining with holes in the acceptor-doped region, thus creating a fix negative charge; in the same way, holes diffusing into the n region recombine with donor electrons, creating a region of positive charge; this *space charge region* creates an electric field opposing to the spontaneous diffusion of majority carriers (i.e. electrons from the n region and holes from the p region), thus reaching an equilibrium.

From the band model point of view, the generation of a built-in potential V_{bi} can be explained with the requirement for the Fermi level of the two extrinsic semiconductor to line up at thermal equilibrium, as schematically illustrated in Figure 2.3. The value of this voltage can be calculated from the difference of the intrinsic levels in the neutral p and n regions.
Infact, using Equations 2.11 and 2.12 setting the majority carrier concentration equal to the acceptor and donor concetation, we have:

$$N_D = n_I \mathrm{e}^{\frac{E_F - E_I^n}{k_B T}}$$

$$N_A \;=\; n_I \mathrm{e}^{\frac{E_I^p - E_F}{k_B T}},$$

which leads to

$$N_A \cdot N_D \;=\; n_I^2 \mathrm{e}^{\frac{E_I^p - E_I^n}{k_B T}};$$

the value of V_{bi} is obtained inverting the above relation:

$$V_{bi} \;=\; \frac{1}{q}\left(E_I^p - E_I^n\right) \;=\; \frac{k_B T}{q} \ln\left(\frac{N_A N_D}{n_I^2}\right). \tag{2.14}$$

Due to this built-in voltage, the space-charge region will be almost empty of free carriers, while majority carriers concentration in the neutral region will be large: it is a good approximation to assume a very thin transition region, so that one can assume an abrupt change between the neutral and the depleted region.
Under these approximations, a first calculation to find the depth of the depleted region may be carried on: infact, it can be assumed that the electic field is zero at the borders of the depleted region and outside it and that the potential difference equals the built-in voltage. This corrisponds to fixing the total charge in the depleted region equal to zero

$$N_D d_n = N_A d_p, \tag{2.15}$$

where d_n and d_p correspond to the extension of the depleted region respectively in the n and p region.
Consequentely, the electric field at the junction is given by

$$\mathcal{E}_{max} = \frac{1}{\varepsilon\varepsilon_0} q N_D d_n = \frac{1}{\varepsilon\varepsilon_0} q N_A d_p, \tag{2.16}$$

and the voltage steps are

$$V_n = \frac{\mathcal{E}_{max} d_n}{2} \qquad V_p = \frac{\mathcal{E}_{max} d_p}{2};$$

setting the voltage $V = V_n + V_p$ equal to V_{bi}, previous equations can be solved to find the depth of the depleted rigion $d = d_n + d_p$:

$$d \;=\; \sqrt{\frac{2\varepsilon\varepsilon_0 \left(N_A + N_D\right)}{q N_A N_D} V_{bi}}. \tag{2.17}$$

In case of very asymmetric doping, where $N_A \gg N_D$, the 2.17 can be approximated as

$$d \;\approx\; \sqrt{\frac{2\varepsilon\varepsilon_0}{q N_D} V_{bi}}. \tag{2.18}$$

It is useful to further analyze the situation of the equilibrium of an unbiased $p - n$ junction: under these conditions, the net current through the system has to be equal to zero. Nonetheless, carrier concentration are very different

in the two neutral regions; for exemple electron concentration is very high in the n region ($n_{n_0} \sim N_D$), while it is very low in the p region ($n_{p_0} \sim \frac{n_I^2}{N_A}$); this implies that diffusion current are expected from region with higher carrier density towards the others but, since the global net current has to be zero, this has to be counterbalanced by a current in the opposite direction: this balance should be valid in any point of the junction for electron and holes separately.
Equations 2.11 and 2.12 can be used to estimate the carrier concentration at an arbitrary position

$$n_n = n_I \mathrm{e}^{\frac{E_F - E_I^n}{k_B T}} \tag{2.19}$$

$$p_p = n_I \mathrm{e}^{\frac{E_I^p - E_F}{k_B T}}, \tag{2.20}$$

so that the ratio of carriers in the neutral regions can be expressed as

$$\frac{n}{n_n} = \mathrm{e}^{-\frac{E_I - E_I^n}{k_B T}} \tag{2.21}$$

$$\frac{p}{p_p} = \mathrm{e}^{-\frac{E_I^p - E_I}{k_B T}}, \tag{2.22}$$

and, similarly, the ratio of carriers of the same type is given by

$$\frac{n_p}{n_n} = \frac{p_n}{p_p} = \mathrm{e}^{-\frac{E_I^p - E_I^n}{k_B T}} = \mathrm{e}^{-q\frac{V_{bi}}{k_B T}}. \tag{2.23}$$

2.2.2 External Voltage

If an external voltage is applied to the junction, the system is no longer in thermal equilibrium and the relations found in previous section can be used only in an approximate way; nonetheless they are still useful in order to extimate the properties of a biased juncttion.
If a forward bias ($V > 0$) is applied, the voltage across the junction will decrease from the built-in value to $V_{bi} - V$; this will cause the width of the space-charge region to decrease, according to 2.17, to

$$d = \sqrt{\frac{2\varepsilon\varepsilon_0 \left(N_A + N_D\right)}{qN_A N_D} \left(V_{bi} - V\right)}; \tag{2.24}$$

if a high enough forward bias voltage is applied to the junction, the space-charge region finally disappear or, in other words, the barrier formed by the built-in potential is removed, allowing majority carriers to flow through the junction, which in the end loses its diode characteristics.
In any case, expression 2.23 can still be used to extimate minority carrier concentration at the edge of the depleted region, expecting

$$n_p = n_n \mathrm{e}^{-q\frac{V_{bi}-V}{k_B T}} = n_{p_0} \mathrm{e}^{q\frac{V}{k_B T}} \tag{2.25}$$

and similarly

$$p_n = p_{n_0} \mathrm{e}^{q\frac{V}{k_B T}}. \tag{2.26}$$

Here n_{p_0} is the electron density at the edge of the neutral p region in the thermal equilibrium case, which equals the electron density in the nonequilibrium inside the neutral p region far away from the edge.
Since minority carriers diffusion current will be proportional to the deviation of their concentration from the equilibrium values, an exponential behaviour for the total diode current is expected:

$$J = \left(J_{s_n} + J_{s_p}\right)\left(\mathrm{e}^{\frac{qV}{k_B T}} - 1\right) = J_s\left(\mathrm{e}^{\frac{qV}{k_B T}} - 1\right),\ V < 0 \tag{2.27}$$

where J_s is the *reverse bias saturation current*: infact, according to Equation 2.27, if a reverse bias ($V < 0$) is applied to the junction, minority carrier current will exponentially reach the limit value of J_s. The entity of this saturation current can be obtained solving the time-indipendent continuity equation for the minority carriers with the edge condition of zero minority carriers concentration ot the edge towards the depleted region:

$$D_n \frac{\partial^2 n_p}{\partial x^2} + G_n - R_n = 0, \tag{2.28}$$

where D_n is the Einstein diffusion coefficient, G_n and R_n respectively the carrier generation and recombination rate; however an explicit solution of the above equation is of no interest in this context.

2.3 High Reverse Biasing: over the breakdown

Among all the properties of externally biased $p-n$ junctions, it is of particular interest in this context to explore in detail the behaviour of a semiconductor diode when an external voltage is applied, intense enough to generate a electrical breakdown in the junction: infact, this process is advantageously used in SiPMs to provide a large signal corresponding to a detection event.

2.3.1 Breakdown

As showed in previous section, although qualitatively, according to Equation 2.27, for reverse bias voltages ($V < 0$), a net current of minority carriers is generated, reaching a saturation value J_s for large enough reverse bias. Further increase in current is due to the growth of space charge region and consequent increase of volume-generated current; however it is intuitively clear that this behaviour cannot proceed indefinitely: at some point, electric field will become so high that electrical breakdown will occurr and the reverse-bias current will increase drastically.
There are two principal mechanisms at work:

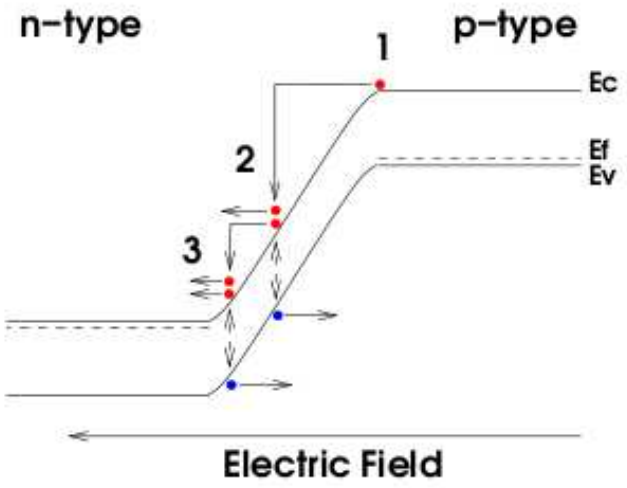

Figure 2.4: Band diagram qualitatively illustrating the process of impact ionization: electrons are in red and holes in blue; this picture had been taken from [13].

- one possibility is given by the so called *Zener breakdown*: in this case, the process is driven by a strong external electric field, whose value is such that electrons in covalent bonding are extracted by the applied electrical force; in other terms, the electrical field can move electrons from the valence to the conduction band;
- the second possibility is the *avalance breakdown*: here the process is originated by carriers (electrons and holes) that impact with the atoms of the crystal: some of them are accelerated by the electrical field until they gain enough energy to break the electron bonding and, in this way, generate another electron - hole couple.

In the following, the mechanisms of avalance breakdown will be analyzed in deeper detail.

When a elctron-hole couple is present in the diode depletion region, the electric field causes their rapid drift in opposite directions; if a sufficiently high bias had been applied, as had been mentioned before, these carriers will gain enough energy to be capable of ionizing by impact the lattice atoms: the carriers extracted in this way will then start to drift across the depleted region and if, as schematically depicted in Figure 2.4, the field is intense enough, they will be capable of impact ionization too, as well as the subsequentely extracted electron-hole

pairs: the result is a self sustaining avalanche of carriers.
Assuming a depleted region of width W, under a biasing condition that make impact ionization multiplication occur, the carrier drifts for a distance $\mathrm{d}x$ in the depleted region, which will increase the number of carriers according to

$$\mathrm{d}n = \mathrm{d}p = \alpha_n(x)n(x)\mathrm{d}x + \alpha_p(x)p(x)\mathrm{d}x, \tag{2.29}$$

where $\alpha_{n,p}(x)$ are the ionization coefficients, respectively for electron and holes; these coefficients are functions of the position x in the depleted region W, as they are strongly dependent on electric field, doping profile, temperature, etc. Assuming an asymmetric doping, with a hole concentration diffusing from the undepleted p-region *much larger* than from the undepleted n-region, it is therefore a good approximation setting $p(W) = 0$; thus, the hole concentration can be rewritten as

$$p(x) = n(W) - n(x), \tag{2.30}$$

so that, via Equation 2.29, the following equation is obtained:

$$\frac{\mathrm{d}n}{\mathrm{d}x} = \left(\alpha_n(x) - \alpha_p(x)\right) n(x) + \alpha_p(x)n(W). \tag{2.31}$$

A solution can be found in the simplified case of $\alpha_n(x) = \alpha_p(x) = \alpha(x)$, which leads to

$$n(W) = n(0) + \int_0^W \mathrm{d}x \, \frac{\mathrm{d}n}{\mathrm{d}x} = n(0) + n(W) \int_0^W \mathrm{d}x \, \alpha(x); \tag{2.32}$$

defining the multiplication factor $M = n(W)/n(0)$, one obtains

$$M = \frac{1}{1 - \int_0^W \mathrm{d}x\alpha(x)}. \tag{2.33}$$

The condition for breakdown is expressed by $M \to +\infty$, which corresponds to

$$\int_0^W \mathrm{d}x \, \alpha(x) = 1. \tag{2.34}$$

An other treatment of Equation 2.29, under different approximations, had been performed in [14] leading to

$$\int_0^W \mathrm{d}x \, \alpha_p(x) \exp\left\{ \int_0^x \mathrm{d}x' \left(\alpha_n(x') - \alpha_p(x')\right) \right\} \, = \, 1; \tag{2.35}$$

starting from Equation 2.35, several calculations of the impac tionization coefficients had been carried on, under different approximations.

In [16] expressions for impact ioniztion had been obtained under the approximation that $\alpha_p = \alpha_n$ and for two different expression of the electric field across the junction. The solution obtained in case of square field corresponds to:

$$1 - \frac{1}{M} \approx \frac{1}{2} W \, \alpha(E_M), \tag{2.36}$$

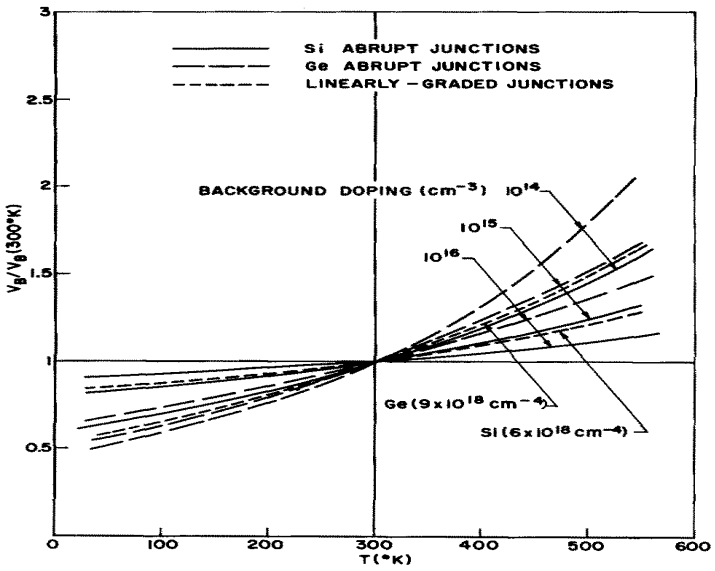

Figure 2.5: Theoretical prediction of the breakdown voltage dependence obtained in [15], for different semiconductors and different doping concentrations and profiles.

where W is the width of the depleted region and E_M is the electric field maximum which, in case of square field is given by:

$$E_M \;=\; 1.5\frac{V}{W} \;=\; (1.5/W_1)V^{2/3} \tag{2.37}$$

where V is the sum of the built-in potential and externally applied potential across the junction and W_1 is a technology dependent scale parameter.
In case of parabolic field, instead, ionization coefficent is given by

$$\alpha(E_M) = \frac{2}{\pi}\left(\frac{1.5}{W_1^3}\right)\frac{\mathrm{d}}{\mathrm{d}E_M}\int_0^{E_M}\mathrm{d}E\frac{(1-1/M)}{(E_M-E)^{1/2}} \tag{2.38}$$

and calculated numerically.
However, in [17] consistent discrepancies between the predictions given by Equations 2.37 and 2.38 and the experimental data had been brought to attention and evaluations more adherent to observations had been obtained realeasing the approximation of $\alpha_p = \alpha_n$. In particular, a phenomenological expression had been proposed

$$\alpha_{n,p}(x) \;=\; a_{n,p}\mathrm{e}^{-b_{n,p}/E(x)} \tag{2.39}$$

whose parameters $a_{n,p}$ and $b_{n,p}$ (for electrons and holes, respectively) had to be determined experimentally.

It is worth to note that no exact values exist for ionization coefficient *above* breakdown, since they are highly dependent on the the exact process of ionization and the structure of the device, as stated for exemple in [18]; nonetheless, results for Equation 2.39 obtained in [19] are often quoted and used in literature.

In parallel, attempt to analitically derive behaviour of breakdown voltage V_{BD} with temperature variations had been performed, through another analytical evaluation of ionization coefficients: in [15] first results are presented, predicting an exponential dependence of breakdown voltage from temperature, as shown in Figure 2.5, even though appears to be strongly dependent from the technological parameters of the junction (semiconductors, doping profile): thus, the consistence of these results with the linear dependence previously experimentally found by various authors (see [16] and [20] for exemple), given by

$$V_{BD}(T) = V_{BD}(T_0)\left(1 + \beta\left(T - T_0\right)\right), \tag{2.40}$$

may not be trivial, since for different construction specifications, the range of validity of the linear approximation may vary significantly.

2.3.2 Geiger-Müller Avalanche

When the applied reverse bias voltage is in excess of the breakdown voltage (V_{BD}), the process of ionization by impact from accelerated carriers becomes self-sustaining, which means that a non-negligible percentage of extracted carriers are themselves accelerated enough to be capable of ionize lattice atoms by impact and so on, in an avalanche process.
To quantify this phenomenon, in [21] the functions $P_{n,p}(x)$ had been introducted and defined as the probability for respectively an electron and a hole to generate an avalanche in the point x of the depleted region.
The probability that electron - hole pair generates such an avalanche is thus given by

$$P_{pair}(x) = P_n(x) + P_p(x) - P_n(x)P_p(x) \tag{2.41}$$

which is obtained from the complementary of the probability that neither the electron nor the hole start the avalanche.
In a similar way, the probability that a carrier in position $x + \Delta x$ generates an avalanche is obtained as the complementary probability that neither in the previous position x nor in the path from x to $x + \Delta x$ the process had started; this leads to a couple of differential equations for these probability distribution functions

$$\frac{\mathrm{d}P_n(x)}{\mathrm{d}x} = \left(1 - P_n(x)\right)\alpha_n(x)\left(P_n(x) + P_p(x) - P_n(x)P_p(x)\right) \tag{2.42}$$

$$\frac{\mathrm{d}P_p(x)}{\mathrm{d}x} = \left(1 - P_p(x)\right)\alpha_p(x)\left(P_n(x) + P_p(x) - P_n(x)P_p(x)\right), \tag{2.43}$$

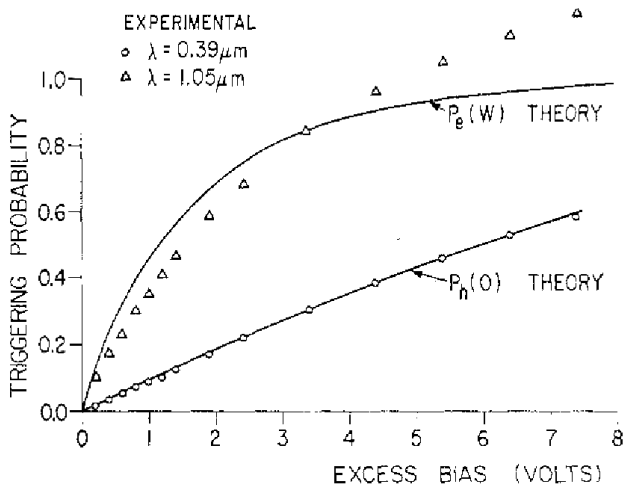

Figure 2.6: Comparison between the numerical solution of Equations 2.42 and 2.43 obtained in [21], and experimental values for the triggering probability for electron and holes.

where, again, $\alpha_{n,p}(x)$ are the ionization coefficients. It has been proven in [22] that solving Equations 2.42 and 2.43 with the boundary conditions of

$$P_n(0) \;=\; P_p(W) \;=\; 0$$

and in the limit that both $P_{n,p}(x)$ approach zero, the Equation 2.35 is obtained, meaning that triggering avalanche probability drops to zero for bias values reducing to breakdown voltage.

Equations 2.42 and 2.43 had been numerically resolved in [21] for a step function doping profile, showing a good agreement with experimental data, as illustrated in Figure 2.6.

Chapter 3

The Tool

Silicon Photo-Multipliers are an enabling technology, originally invented in Russia [2]. They essentially consist of an *array of p-n junctions* operated beyond the breakdown voltage [16], in a Geiger-Müller regime [21] described in previous chapter, with typical gain of the order of 10^6 and on-cell integrated quenching mechanisms.
The technology development is by now focused on the spectral response, the control of the dark count rate and the optical cross-talk, together with the improvement of the photon detection efficiency; however devices are by now commercially available and naturally bound to replace photo-multiplier tubes for most of the high-end applications.

Silicon photo-sensors with internal multiplication are in use since more than a decade[1]: Avalance Photo-Diodes (APDs) [23] are operated in a proportional regime, with typical gains of 10^4 and sensitivity up to 50 A/W; Single-Photon Avalanche Diodes (SPADs) [24], do feature single photon sensitivity and are tailored for high frequency counting with time resolutions down to 50 ps; however, being made out of a single cell operated in binary mode, do not carry any information about the intensity of the incoming light field.
SiPMs complement the family of existing sensors: with a cell density of $\sim 10^3/\mathrm{mm}^2$, areas up to 3×3 mm^2 and *a single output node*, they offer the possibility of measuring the intensity of the light field simply by counting the number of fired cells.
In the following, the principal figures of merit characterizing these devices will be discussed in more detail.

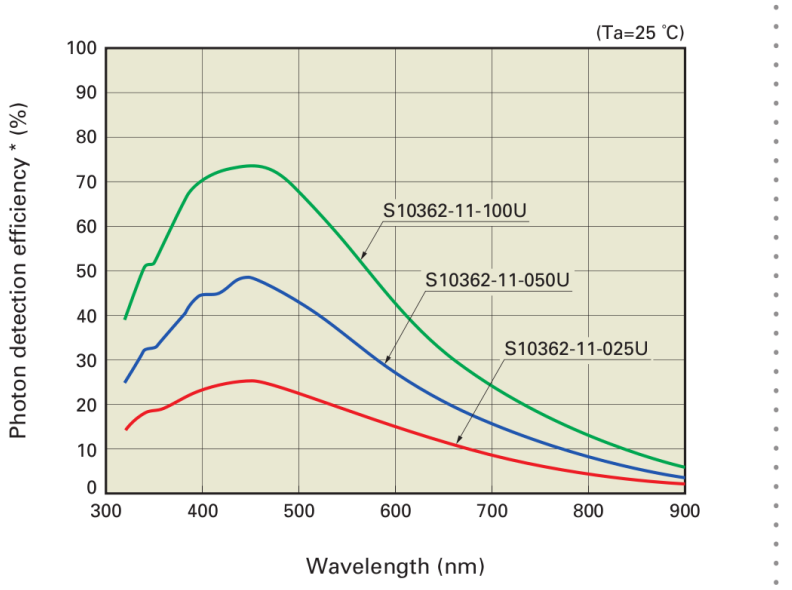

Figure 3.1: Photo-Detection Efficiency for light of different wavelengh for three different SiPM producted by Hamamatsu Photonics, taken from the data sheet available on line at http://www.hamamatsu.com/ .

3.1 Photon Detection

Regardless of the specific architecture of the sensor, a series of events are necessary in order to trigger a response:

1. a photon impinging on the detector surface must reach the depleted region;
2. a photon reaching the depleted region must extract an electron-hole pair, whose elements start drifting;
3. carriers drifting through the depleted region must ignite an avalanche;
4. the signal generated by the avalanche must be detected by the external electronics.

3.1.1 Photo-Detection Efficiency

When a photon flux of wavelenght λ and intensity I_0^λ is travelling through a medium, its intensity is attenuated according to the Beer-Lambert law

$$I(\lambda, z) = I_0^\lambda \mathrm{e}^{-\alpha(\lambda) z}, \tag{3.1}$$

where z is the distance covered by the light in the medium and $\alpha(\lambda)$ is the so called *attenuation factor* whose value depends obviously from the wavelenght

of light flux and on the medium light is travelling in; it can be assumed that attenuation of light in a semiconductor diode is essentially due to photons extracting electron-hole pairs (see for example [13]).
The probability for a photon of wavelenght λ to generate an electron-hole pair in the depleted region is commonly addressed as *quantum efficiency* and it depends on the exact stucture of the junction (thickness of the top undepleted layer, dimension of the depleted region and so on); in Figure 3.1 dependency of the global detection efficiency from the impinging photon wavelenght is depicted: its profile is due to different quantum efficiency values at different wavelenght. The presence of a maximum is due to the fact (see [25]) that in case of light impinging on a SiPM, fluxes of too short wavelenght are extinguished before reaching the depleted region and carriers extracted in the top undepleted volume of the diode have a negligible probability of reaching the active region before recombining; on the other hand, light of too long wavelenght will simply pass through the depleted region, having a very low probability of extracting any carrier.

Once electron-hole pairs had been generated, they start drifting through the depleted region and can then trigger a Geiger-Müller avalanche, with a probability previously described in Chapter 2, whose main parameter, for a given detector, is essentially the intensity of the overvoltage bias, that is the applied bias voltage exceeding the breakdown voltage.
Thus, to obtain an enhanced blue sensitivity, which is of particular interest for exemple in PET applications, efford has been spent to obtain a doping profile which could maximize the top part of the depleted layer [25] [8].

These two probabilities both contribute to one of the key parameters describing the performances of a SiPM, called *Photo-Detection Efficiency* (PDE) and is defined as

$$\mathrm{PDE}(\lambda, \Delta V_{OV}) = FF \times P_E(\lambda) \times P_A(\Delta V_{OV}), \tag{3.2}$$

where $P_E(\lambda)$ is the quantum efficiency, $P_A(\Delta V_{OV})$ is the probability for an electron-hole pair extracted in the depleted region of generating a Geiger-Müller avalanche for a give overvoltage bias ΔV_{OV}. The factor FF, called *fill factor*, is an additional parameter, whose value ranges from zero to one, representing the fraction of *active area* over the total exposed area: this reduction of the total active area is principally due to the cell bonding and quenching resistors; nonetheless, distance between cells (i.e. inactive area) can be increased also for reducing cross-talk effects, thus enhancing global sensor performances.

3.1.2 Temporal Resolution

Temporal resolution of photo-detection is a key parameter in many applications, noticeably TOF - PET applications, where time jitter of the order of one-hundred picoseconds, coupled with fast scintillators, is requested (see for exemple [8]).

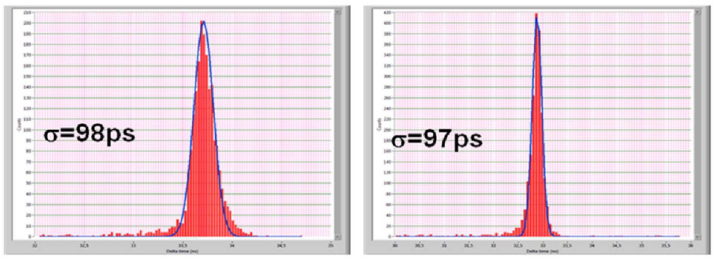

Figure 3.2: Comparative analysis of temporal resolution between an Hamamatsu SiPM (left panel) and a FBK SiPM (right panel), performed in [26].

The simpliest method to evaluate this chatacteristic is to illuminate the device under study with pulsed light and measure the temporal difference between a signal synchronous with the light source and the SiPM output: the broadening of the resulting histogram is an extimation of the device temporal resolution (an exemple is illustrated in Figure 3.2).
This parameter is obviously technology dependent, but studies conducted confirm the SiPM sub-nanosecond capability and in many cases can reach values of less than one hundred of picoseconds [26], [27].

3.2 Gain

The general beahviour of semiconductor diode working in avalanche mode can be sketched with the simple circuital model depicted in Figure 3.3. The pre-breakdown state can be represented as a capacitance C_D, corresponding to the junction capacitance, whose value can be fairly enough assumed as fixed for biasing voltages greater than the fully depletion voltage; this capacitance is in series with the quenching resistor R_Q and charged at a bias voltage $V_{BIAS} > V_{BD}$, this situation corresponding to the switch in the OFF position. Then, when a carrier traverses the depleted region has a certain probability of triggering an avalanche: if this happens, the new state can be modeled with the circuit in Figure 3.3 with the switch in the ON position, adding a new resistor R_S in parallel to the capacitance, representing both the resistance of the neutral regions of the diode and the space-charge resistance, and a voltage source V_{BD}. The capacitance discharges through the series resistance with a time constant given by the product $\tau_D = R_S C_D$.
As the voltage on C_D decreases, due to the current flowing through the quenching resistance, the current approaches to its asymptotic value of $(V_{BIAS} - V_{BD})/(R_Q + R_S)$ and, simultaneously the triggering probability drops to zero, thus quenching the avalanche.
The new situation of turned off avalanche corresponds to the switch again in the open position and the capacitor starts recharging to the bias voltage with a

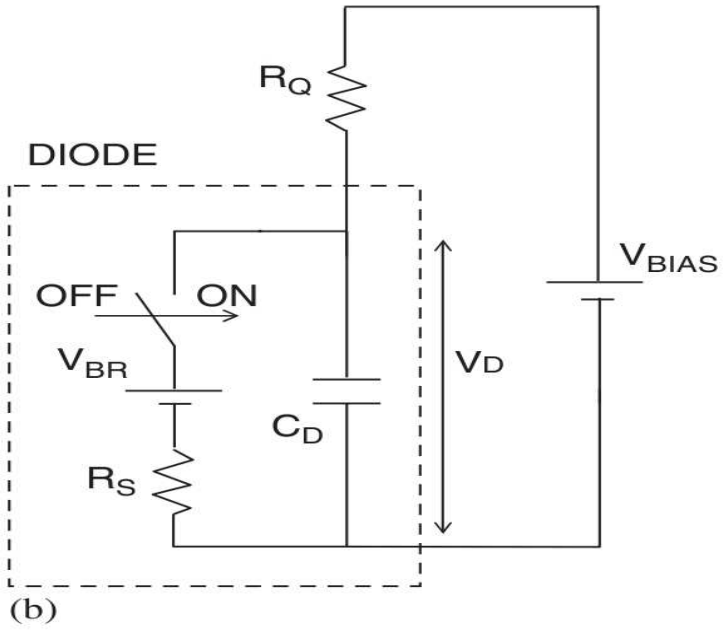

Figure 3.3: Schematic circuital model describing the behaviour of an avalanche diode of capacity C_D, with internal resistance R_S, biased at $V_{BIAS} - V_{BR}$ over breakdown voltage and and with a passive quenching resistor R_Q; the ignition of the avalance corresponds to the switch moving to the ON position; this picture had been taken from [25].

time characteristic $\tau_C = C_D R_Q$.
For a biased junction, capacitance-voltage characteristic can be determined and constitute useful parameters to describe the diode properties.
In particular, the capacitance C_D of a biased diode with a depleted region W whose depth is governed by Equation 2.24, can be calculated (see [11]) and corresponds to:

$$\frac{1}{C_D} = \frac{W}{\varepsilon\varepsilon_0} - \frac{1}{qN(W)}\frac{\partial V_{bi}}{\partial W}, \tag{3.3}$$

where ε and ε_0 are the dielectric constants, q the carriers charge and N their concentation. The second term of the previous equation is due to the variation of built-in voltage with doping and thus is usually negligible, at least in conditions of high reverse bias. Thus Equation 3.3 can be approximated as

$$C_D = \frac{\varepsilon\varepsilon_0}{W}. \tag{3.4}$$

In case of high reverse bias exceeding the breakdown voltage, the increase of the width W of the depleted region due to voltage increase becomes negligible:

therefore, for a fully depleted junction, its capacitance could be considered as fixed. Consequentely, as stated in [28] the amount of charge released by an avalanche in a over-the-breakdown reverse biased junction, can be easily calculated using:

$$Q \;=\; qG \;=\; C_D\,\Delta V, \tag{3.5}$$

where ΔV is the reverse bias in excess to the breakdown voltage. The properties of the junction are often expressed through the parameter G, called *gain*, as it indicates the number of carriers released in the process.

3.3 Dark Counts

Not all the measured G-M avalanches are originated from detection of impinging photons: a certain amount of these events is due to electron-hole pairs thermally extracted in the depleted region; because these events are triggered also in absence of external illumination of the diode, they are commonly addressed as Dark Counts and the principal figure of merit used to describe their influence on SiPMs performarces is the *Dark Count Rate* (DCR).

In Chapter 2 several Equations describing the carrier in density in conduction band had been introduced and will be now recalled, making the temperature dependence of these functions more explicit.
In particualer, Equations 2.25 and 2.26 describe the occupation density of minority carriers in case of external reverse bias across the junction; using Equations 2.19 and 2.20 the dependence from the intrinsic carrier density n_I becomes clear:

$$n_p \;=\; n_I \mathrm{e}^{\frac{E_F - E_I^n}{k_B T}}\, \mathrm{e}^{-q\frac{V_{bi}-V}{k_B T}} \tag{3.6}$$

$$p_n \;=\; n_I \mathrm{e}^{\frac{E_I^p - E_F}{k_B T}}\, \mathrm{e}^{q\frac{V_{bi}-V}{k_B T}}. \tag{3.7}$$

From Equations2.5, 2.6, and 2.7 a $T^{3/2}$ dependence of n_I can be made explicit.

A much more accurate treatment of the thermally generated avalanches includes a contribution from the Shockley-Read-Hall effect (which turns out to be dominant, see for exemple [13]): the presence of defects and impurities creates local energy traps within the depleted region, with energy level such as $E_v < E_t < E_C$; these traps allow an easyer carrier generation (and recombination, as well).
Staring from the continuity equation 2.28 and calculating the occupation probability using Equation 2.1, an extimation of the Shockley-Read-Hall carrier ther-

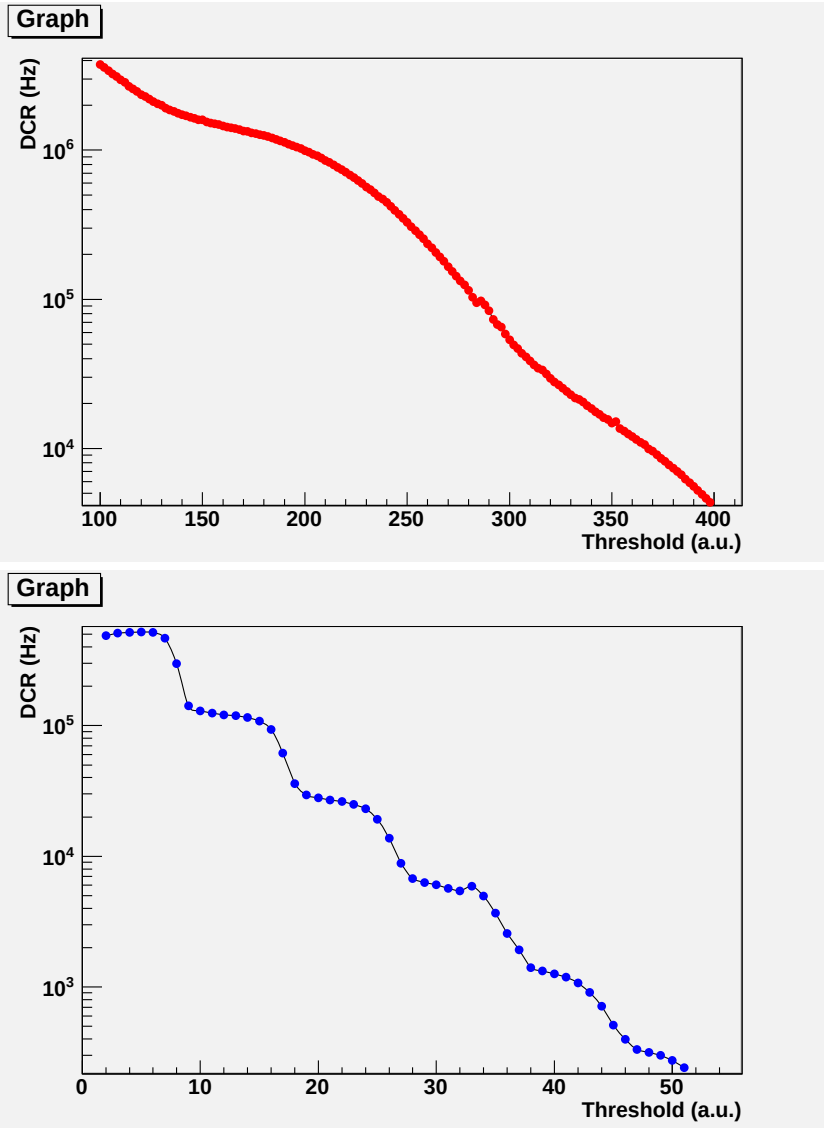

Figure 3.4: Example of *staircase curves* for two different models of SiPM: in the upper panel, a threshold scan of DCR for an STM TO8 prototype with 4900 cells separated by reflective trenches is shown, while in the lower panel a scan of a Hamamatsu S10361-100C with 100 cells; both measurements had been performed at room temperature. The higher cell number of the first one is the principal motivation underneath the higher DCR values and the less resolved shape of the "steps".

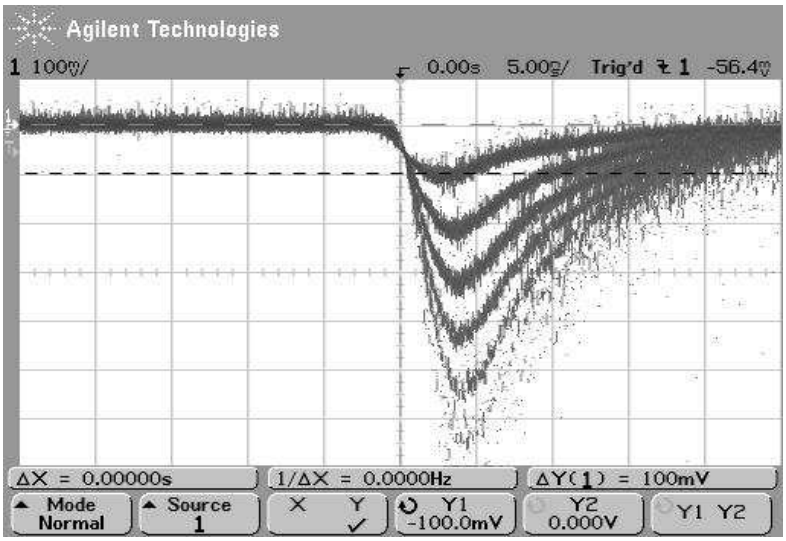

Figure 3.5: Oscilloscope screenshot a SiPM voltage output self-triggered; several curves corresponding to the cell signals are clearly visible.

mal generation rate G_{th} can be done[1] in absence of external illumination:

$$G_{th} = \frac{N_t \nu_{th,n} \sigma_n \nu_{th,p} \sigma_p n_I}{\nu_{th,n} \sigma_n \mathrm{e}^{\frac{E_t - E_I}{k_B T}} + \nu_{th,p} \sigma_p \mathrm{e}^{\frac{E_I - E_t}{k_B T}}}, \tag{3.8}$$

where N_t in the defect concentration, ν_{th} is the thermal drift velocity, σ is the capture cross-section; due to the presence of the intrinsic carrier density at the numerator of the above expression, a contribution to the temperature dependence proportional to $T^{3/2}$ is expected.

Since the subsequent avalanche triggering process is obviously identical to what previously described, the signal output due to these dark counts is indistinguishable from ordinary detection signal; for this reason, the DCR value at varying operational parameters (mostly bias voltage and temperature) is a relevant figure of merit to characterize the noise of the given detector.
One of the simpliest and although most exhaustive characterization of the DCR beahviour of a given detector, is obtained performing a threshold scan measurement of the sensor output without illumination; an example is illustrated in Fig. 3.4: for the tipical shape of the output in logarithmic scale, these curves are often referred as *staircase curve*. The first abrupt drop in the counts is associated to a treshold value such to neglect the signal of a single cell firing; the presence of subsequent "steps" has its origin in optical cross-talk effects, more

[1] for the details of the calculation, of low interest in this context, see for exemple [11]

than in simultaneous triggering of thermal extracted electron-hole pairs.
The shape itself of the step of the DCR scan illustrated in Figure 3.4 is worth a comment. It appears clear that staircase shown in the upper panel, taken from a sensor with 4900 cells, appears less resolved than the one shown in the lower panel, acquired from a 100 cells SiPM; the resolution capability r of SiPM can be described with

$$r \propto \frac{\Delta_{PP}}{\sigma_{noise}}, \tag{3.9}$$

where Δ_{PP} is the peak separation and σ_{noise} is the signal noise: for a reference see Figure 3.5. For fixed Δ_{PP} values, σ_{noise} increases with the global cell number of the device n_c: for a first qualitative analysis, the gaussian noise broadening of each peak is due to the sum of the noise contribution of each cell σ^0_{noise}:

$$\sigma_{noise} \propto \sqrt{n_c}\sigma^0_{noise}. \tag{3.10}$$

Moreover, sensor resolution decreases with increasing number of simultaneously firing cells, as will be described with deeper detail in Chapter 4.

3.4 Optical Cross-Talk

The *optical cross-talk* is the G-M avalanche triggering due to an avalanche firing in a neighbour cell. The physical phenomenon underneath this effect is the photon emission of accelarated carriers forming a G-M avalanche(see for example [29], [30]): these photons travel through the crystal, attenuating according the aforementioned Beer-Lambert law 3.1; photons reaching the depleted region of a neighbour cell can then extract an electron-hole pair which, subsequentely, can trigger an avalanche, and so on, in a cascade process.
It is thus clear that two main parameters influence the entity of this effect:

- structural parameters, mainly the distance between the SiPM cells: it has been clearly shown that (see for example [31]), according to the prediction of Eq. 3.1 cross-talk percentage decreases exponentially with increasing distance between cells;

- since G-M avalanche triggering probability is ruled principally by overvoltage bias (see for example [21]), increasing overvoltage increases the number of optical cross-talk events.

An option to reduce diffusion of photons from one firing cell to neighbour diodes is the insertion of reflective material trenches, as showed for example in [25], which reduces the optical cross-talk at the price of a lower fill factor and thus a lower PDE.

One of the simpliest method to measure the entity of this effect is based on the analysis of threshold scan measurements of DCR: it is based on the assumption that, performing such a measurement in absence of external illumination of

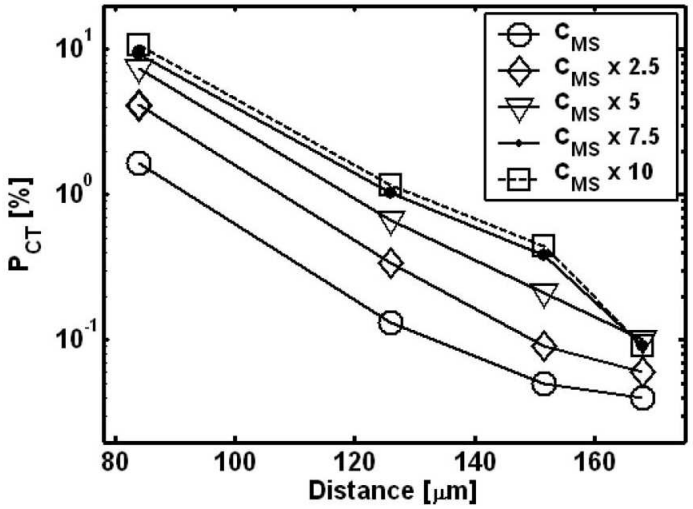

Figure 3.6: In this picture taken from [31] it is clear the exponential dependence of optical cross-talk probability from cell distance; different curves had been evaluated for different capacitance diodes, where $C_{MS} = 100$ fF: for fixed cell distance, cross-talk increases with increasing capacitance, since more charge is released in the avalanche process and more bremsstrahlung photons are emitted.

the device, only a negligible part of the counts over the *one-photon threshold* (i.e. the threshold corrsponding to the output signal of one cell firing), is due to simultaneous (i.e. within the time resolution of the SiPM, tipically at the hundreds of picoseconds level) dark count events, while they are principally originated from optical cross-talk. With this assumption, an estimation of the fraction of cross-talk events can be obtained simply by

$$X_T = \frac{DCR_{1.5}}{DCR_{0.5}}, \tag{3.11}$$

where X_T is the fraction of cross-talk events, and $DCR_{0.5,1.5}$ are the dark count rates obtained setting the threshold, respectively, between the zero and one photon level, and between the one and two photon level.

Measurements performed on different sensors show that optical cross-talk can produce a relevant number of false positive output signal, thus creating relevant deviations of the measured mean number of triggered cell from the mean number of detected impinging photons; an example of these values is shown in Table 3.1: two different sensors, from two different producers has been studied and cross-talk measured at different biasing conditions. It clearly emerges how, without reflective trenches, at high overvoltages, the fraction of cross-talk induced events can reach high values, up to 30 - 40 % of the total measured events.

STM TO8 (with trenches)		SensL CSI 0740001 (w/out trenches)	
Overvoltage (V)	Cross-Talk (%)	Overvoltage (V)	Cross-Talk (%)
0.78	1.0 ± 0.1	0.92	5.6 ± 1.3
1.13	1.1 ± 0.1	1.92	11.7 ± 1.4
1.5	1.2 ± 0.1	2.92	22.1 ± 1.6
1.71	1.3 ± 0.1	3.92	32.4 ± 1.7

Table 3.1: In this table are listed, as an example, the results of our cross-talk measurements on two different SiPMs, from two different productors.

3.5 Afterpulses

There is also a possibility that a G-M avalanche triggers a second avalanche in the same cell: these kind of induced events are called *afterpulses*. This phenomenon is tought to be caused by carriers extracted during the avalanche process that are trapped in local potential minima and subsequentely released, with a characteristic time ranging from few nanoseconds, up to microseconds , thus igniting another avalanche. The amount of charge added by this secondary events depends on the state of the diode when the afterpulse is triggered, an thus on the avalanche recovery time, according to [32]

$$\xi(t) = 1 - \mathrm{e}^{-\frac{t}{\tau_R}}, \tag{3.12}$$

where $\xi(t)$ is the fraction of charge carried by an afterpulse ignited at a time t after the previous avalanche triggering, in a diode with recovery characteristic time τ_R; it is immediately clear that afterpulses occurring in the time region of $\xi(t) \approx 1$ are indistinguishable from an ordinary pulse.
The probability for an afterpulse being triggered at the time t after a prefious pulse can be written as

$$P_{AP}(t) = \frac{1}{\tau_{short}}\mathrm{e}^{-\frac{t}{\tau_{short}}} + \frac{1}{\tau_{long}}\mathrm{e}^{-\frac{t}{\tau_{long}}} \tag{3.13}$$

as done in [32], where $\tau_{short,long}$ are the escape characteristic time; in [33] (and subsequentely by other authors, see [32] or [34]) it had been shown that a better agreement with experimental data is obtained by the sum of two afterpulse probability distributions, with two different time constants, describing a short ($\tau_{short} \sim 10$ ns) and a long ($\tau_{long} \sim 100$ ns) temporal beahviour, making the treatment of this effect utterly non-trivial.

Chapter 4

Characterization: the key to use SiPMs

SiPMs are powerful tools, with many intriguing features:

- their G-M operating mode grants them high gain, comparable to the values archieved with standard PMTs;

- their cell structure grants them an enhanched linearity, with deviation starting to become relevant when the average number of detected photons approaches the same order of magnitude of the number of cells of the device [35];

- the former, together with their pixelateded structure with a common output, provides a high dynamic range, spanning from single photon regime up to high intensities;

- the silicon-based technology of these devices grants them operability in magnetic fields, compactness and relatively low cost.

On the other hand, since G-M avalanches triggered by electron-hole pairs extracted by detection of impinging photons are obviously indistinguishable from ones originated from other processes, dealing with all possible sources of noise is far from being trivial:

- thermally extracted electron-hole pairs are the origin of high Dark Count Rates, with values ranging from several hundreds of kiloHertzs up to the MegaHertz level, depending on the total number of cells, the operating temperature and the over bias;

- spurious signals are also due to optical cross-talk: photons emitted by an avalanche can travel through silicon and reach the depleted region in a neighbour cell, thus triggering another avalanche;

- last but not least, carriers extracted during an avalanche process may be trapped in a false potential minimum in the depleted region: escaping from that trap can originate an *afterpulse* avalanche, so called beacuse the characteristic time for carriers escaping from the potential minimum is such that it tipically happens shortly after (or even during) the recovery of the previous avalanche.

The need for a characterization of the SiPM performances arose within the framework of the RAPSODI[1] project, in which the University of Insubria took active and leading role, and which had the aim of developing three different sensors using SiPMs, with three different operational requirements; the principle behind each one of these sensors which will be briefly described in the following subsections.

4.1 Characterization Protocol

Tests have been performed on existing devices with the main goal to define an exhaustive protocol and to produce a comparative study. Three kind of detectors were under test, from different manufacturers: SensL[2], Hamamatsu Photonics[3] and ST Microelectronics[4]. As shown in previous sections, the characterization of detectors is a major task for all of the applications on SiPM, with application dependent critical parameters: for example, DCR is an important parameter for low event rate application and thermal stability is essential for portable devices. For this reason the following exhaustive protocol has been developed with the intention to focus on subsets of it, depending on the applications envisaged within RAPSODI:

- Geometrical parameters (number of cells, size of detectors and occupancy factor);
- I - V measurements;
- Noise measurements:
  - Dark Counting Rate (DCR);
  - Optical cross-talk;
  - Dependence on the environmental parameters;
- Analysis of photon spectra:
  - Resolution power;
  - Gain;

[1] European founded project - COOP 32993 - RAPSODI
[2] http://sensl.com/
[3] http://www.hamamatsu.com/
[4] http://www.st.com/stonline/

  - Working point optimization (at low and large flux);
  - Electronic noise measurement taking into account cell-to-cell variations;
  - Dependence on the environmental parameters (Temperature);

- Linearity and dynamic range;
- Spectral response measurement:
  - Photon Detection Efficiency.

In particular, studies on the temperature behaviour of the main SiPM parameters (such as gain, PDE, DCR and optical cross-talk) will be described with deeper detail.

4.1.1 Experimental setup

In order to carry on this characterization protocol, a complete experimental setup has been put in place in the Silicon detector laboratory at Università degli Studi dell' Insubria in Como.
As a light source, a green-emitting LED ($\lambda = 510$ nm) has been used, coupled to a fast pulse generator *PDL800-B PicoQuant*. The SiPM output signal has been delivered using the following acquisition chain and digital electronics:

- SiPMs were directly connected to a first stage amplification board:
  - in experimental situations where the SiPM operated under a continuous light flux, a Transimpedance pre-amplifier provided by SensL has been used: this device converts the raw current from the SiPM into a voltage, with an amplification of 470 V/A;
  - when the SiPM was meant to operate in a pulsed light regime, a different pre-amplifier had been used, called Pulse Amplifier and also provided by SensL, which allowed the fast rise of the detector to be exploited, providing an amplification factor of 20;
- a leading edge discriminator *Lecroy 821* with a user-defined voltage threshold which SiPM output has to exceed in order to provide a triggering signal;
- in case of frequency measurements (e.g. DCR measurements), discriminator output has been directly delivered to a scaler;
- output of SiPM has been processed by a *CAEN QDC V792N* board:
  - the board provides a charge measurement performing integration of the input voltage signal, with a conversion time of 2.8 μs and a reset time of 4 μs;

  - the temporal window of integration is obtained providing a gate NIM signal,which must precede the analog input signal of at least 15 ns;

- digital information has been trasferred to the equippement computer through a *USB-VME Bridge CAEN* .

The system composed by the investigated SiPM and a first-stage amplification board, has been set in metal box sealed with grease, in which air has been replaced with helium. Eventually, cooling fluid has been pumped into the box through a copper pipe, allowing controlled temperature variations. Temperaure of the system has been measured by a thermistor placed in contact with the external packaging of the sensor.

4.2 Different applications, different needs

The RAPSODI collaboration was an international collaboration, founded by the European Commission, whose partners were: the *University of Como*, the *Institute for Theoretical and Experimental Physics*[5] (ITEP), *Akademia Górniczo-Hutnicza*[6] (AGH), PTW[7], *SensL*[8], *FORIMTECH S.A.* and *Jiri Plch-specialni merici metody*. The aim of the project was the developement of three detectors, using the SiPM technology:

- a real time dosimeter for mammography, called MAMMODOS;

- an ambient Radon concentration meter, called RADIM 7;

- a portable detector for illicit radioactive material transportation, called *The Snooper*.

The main issues related to these three prototypes and the SiPMs will be briefly presented in the following subsections.

4.2.1 MAMMODOS: real time dosimetry for mammography

The device under study was meant to be a novelty in the field of mammography, consisting in a cost-effective and compact instrument, composed by a very thin detection plate (or a scintillation fiber), SiPMs as light sensors and a small local display, to perform a real-time measurement of the dose delivered to a patient during a mammography examination. The part introduced into the imaging beam had to be engineered to be either fully tissue equivalent and homogeneous or semi-opaque and clearly identifiable, with no possibility to be considered an

[5] http://www.itep.ru/eng/in_eng.shtml
[6] http://www.agh.edu.pl/en
[7] http://www.ptw.de/
[8] http://sensl.com/

artefact. The instrument had been designed to be used in contact with the patient, mounted to the paddle of the mammography X-ray machine in such a way that the display on the side can be visible during and especially after the mammography examination: consequentely, the sensor must b capable of measurements under a continuous flux regime.. The prototype consists of a blue light emitting plastic tile[9] ($1 \times 4 \times 0.1$ cm^3) optically coupled to a 1 mm diameter Wave Length Shifting (WLS) fiber, delivering light to SiPMs.
The whole instrument had to be characterized relying on four principal figures of merit:

- precision: defined as the spread of the measurements for constant irradiation conditions.
- sensitivity: defined as the minimum detectable variation in the dose rate.
- minimum detectable signal: differing from the sensitivity because of the pedestal spread
- linearity measured against the dose rate in the region of interest.

All of them obviously have an influence on the choice of a proper model of SiPM:

- the main issue is related to linearity: infact, as the system has to be compliant with dose rates ranging from 2 mGy/s up to 150 mGy/s (as required by the council directive 97/43 EURATOM, article 8, sub-clause 6), the SiPM coupled with the WLS fiber should be able to provide a robust linear response, spanning two order of magnitude of impinging fluxes of light;
- at the same time, the same directive requires a 5 % sensitivity on dose rates measurements, which implied a control an all possible sources of noise, in particular DCR, which had to be as low as possible.

These two requirements are in a sort of contrast: in fact, the best way to enhance the linear dynamic range of the instrument is obviously to chose a SiPM with high cell number but this implies an increment in DCR values and a worsening of the detector sensitivity and minimum detectable signal; thus, to find the optimal sensor for the MAMMODOS detector, all the available SiPMs had to be characterized.
Different models of SiPMs had been tested under various aspects, in particular concerning their linearity and dynamic range and part of the carried out tests will be described in Section 4.2.1; in the end, the choice for the final prototype led to the detector CSI 0747 015 A20 HD, producted by SensL[10] (SensL 9k henceover), whose main parameters had been measured and reported in Table 4.1.

[9] Produced at ITEP, Moscow
[10] http://sensl.com/

Sensor ID:	CSI 0747 015 A20 HD
Number of Diodess:	8640
Area:	3 mm × 3 mm
Single Diode dimension:	20 μm × 20 μm
Breakdown Voltage:	28.04 V
Leakage current:	0.95 μA
DCR:	8 MHz
Optical Cross-Talk:	22.5 %
Gain:	10^6
PDE:	4 %

Table 4.1: SensL SiPM main characteristics. Measurements refer to room temperature and a working point of +2 V with respect to the breakdown voltage.

I-V direct and indirect measurements

Studies on the output current of the SiPMs were of particular interest for the MAMMODOS application, where the SiPMs were meant to operate under a *continuous flux* (and not pulsed) of incoming light. Tests had been performed in order to estimate the current range and the corresponding frequency of the Geiger-Mueller avalanches: both figures are relevant in the design of a dedicated front-end electronics. Moreover, the latter provides a significant figure for the specific sensor, in term of linearity range against the mean time of arrival between photons.
The I-V curve directly measured for the sensor of interest using the Keithley 4200 Semiconductor Analyzer System is shown in Fig. 4.1. The current was also measured indirectly by normalizing the charge integrated by the CAEN V792 QDC System over a well defined gate window. Values of the current for a set of biasing voltages voltages were obtained as:

$$I = QDC_{cal}\frac{\Delta QDC}{t_{gate}}\frac{1}{K_{amp}}, \tag{4.1}$$

where $QDC_{cal} = 0.11\ pC$/channel is the QDC calibration constant; ΔQDC is the most probable value of the integrated charge spectrum; t_{gate} is the integration time and $K_{amp} = 470/100$ is the effective amplification factor of the transimpedence amplifier.

An indirect estimate of the current beyond the breakdown voltage was also obtained by measuring the Dark Count Rate (DCR), the cross talk and the sensor gain. Assuming the current in the breakdown regime is actually dominated by Geiger-Mueller avalanches, the values of the currents were obtained as:

$$I = G_{SiPM}\, e^{-}\, \nu_A(1 + X_T), \tag{4.2}$$

where e^- is the electron charge, G_{SiPM} is the gain of the SiPM, X_T is the cross-talk, defined as the ratio of the DCR at *"half photoelectron"* threshold

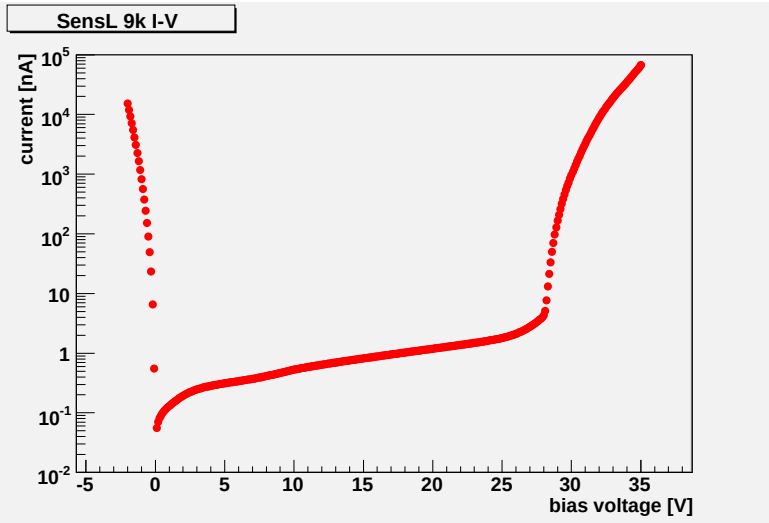

Figure 4.1: I-V profile of the SensL CSI 0747 015 SiPM (SensL9k henceover); mesurements were performed at 25.6 °C.

Bias [V]	$DCR_{0.5}$ [MHz]	$DCR_{1.5}$ [MHz]	X_T (%)	Current [μA]
29.5	7.1 ± 0.8	0.9 ± 0.1	12.7 ± 2	0.82 ± 0.10
30.0	8.0 ± 0.9	1.8 ± 0.2	22.5 ± 3.5	1.53 ± 0.18
30.5	10.2 ± 1.1	3.2 ± 0.4	31.4 ± 4.8	2.80 ± 0.34
31.0	12.0 ± 1.3	5.3 ± 0.6	44.2 ± 6.8	4.53 ± 0.56
31.5	14.0 ± 1.5	8.0 ± 0.9	57.1 ± 8.8	6.94 ± 0.87

Table 4.2: DCR and X_T values for the SensL 9k. Measurements performed at room temperature.

and *"one-and-half photoelectrons"* threshold and ν_A is the avalanche frequency which, in this peculiar situation of no light exposure, has been set equal to the $DCR_{0.5}$, the dark count rate at *"half photoelctron"* threshold; its contribution to the total number of fired cells had been taken into account using Eq. 4.15.

DCR values are summarized in Table 4.2. Data point from the indirect measurements are overlaid to the direct measurements in Figure 4.2 (upper panel), showing a remarkable agreement. The deviation between the direct and indirect measurements is shown in Figure 4.2 (lower panel).

In order to finalize these measurements for the MAMMODOS application, the SiPM dynamic range had to be tested. The minimum current value was estimated for the configuration where the radiation field was probed with a blue emitting fiber, conveying the scintillation light to the sensor via a clear fiber. Data are reported in Table 4.3; there, for each exposure value, the corresponding

values of signal and baseline in QDC counts are presented: errors have been estimated using the standard deviation of each QDC count distribution divided by the squared root of the number of counts; the corresponding values of dose rate are presented as well: these values have been evaluated multiplying the charge measured by a conversion factor calculated using a calibrated equipment. According to Equation 4.1, the minimal detectable current is 0.786 ± 0.005 μA. The Geiger-Mueller avalanche frequency is derived from Equation 4.2 and corresponds to 4.1 ± 0.2 MHz; the error on the frequency has been calculated propagating as well the error on our G_{SiPM} and X_T values. Taking into account a PDE for the SensL 9k at room temperature, with 510 nm green light of about 3.3%, *assuming no more than one visible photon/converted X-ray* is actually detected by the sensor, the mean time of arrival of the photons results to be 8.07 ± 0.39 ns.
The maximum current value has been estimated for the configuration where the radiation field was probed with a tile, at the maximum mAs level and no filter and correspond to a current of 147.4 ± 0.09 μA and an avalanche frequency of 770 ± 35 MHz, namely a photon frequency of 23.3 ± 1.1 GHz. Data are reported in Table 4.4, in a way similar to Table 4.3.
The number of cells triggered by impinging photons can thus be estimated by solving simultaneously Eq. 4.1 and Eq. 4.2 with the following ansatz:

$$N_{cells} = \nu_A \times t_{gate}, \tag{4.3}$$

where ν_A is the avalanche frequency; as an example, values referring to Table 4.3 data have been plotted in Figure 4.3.

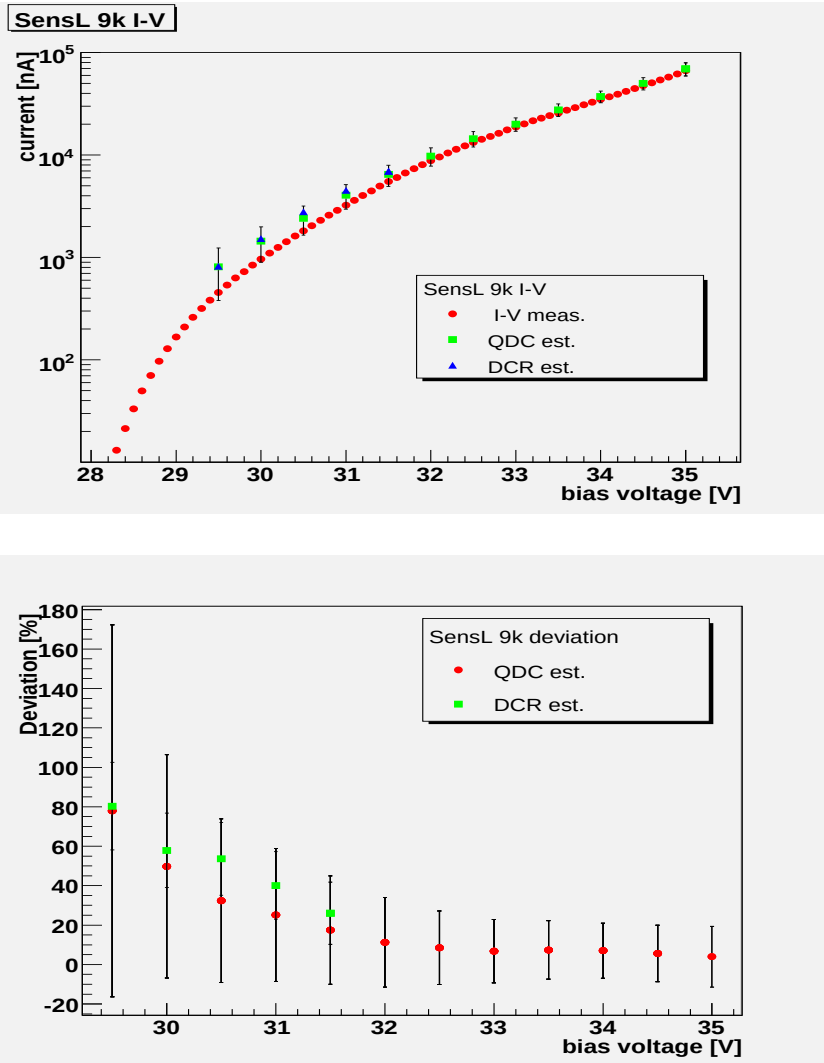

Figure 4.2: Upper panel: I-V data for the Sensl 9k sensor; indirect measurement from the QDC data are shown together with an estimate from the Dark Count Rate. The reference points refer to the direct measurement. Lower panel: percentage deviation of the estimates from the reference values.

Set Exposure [mAs]	Dose Rate [mGy/s]	Signal	Baseline	Current [μA]
10	5.93 ± 0.02	1798 ± 1.0	1630 ± 0.1	0.786 ± 0.005
12	7.84 ± 0.03	1840 ± 0.9	1624 ± 0.1	1.001 ± 0.004
16	8.96 ± 0.03	1859 ± 0.9	1623 ± 0.1	1.105 ± 0.004
20	11.21 ± 0.04	1938 ± 1.0	1622 ± 0.1	1.479 ± 0.005
25	14.14 ± 0.05	2004 ± 1.0	1630 ± 0.1	1.752 ± 0.005
32	16.37 ± 0.06	2071 ± 1.2	1622 ± 0.1	2.102 ± 0.006
40	21.20 ± 0.08	2192 ± 1.2	1622 ± 0.1	2.668 ± 0.006
50	25.62 ± 0.09	2287 ± 1.3	1620 ± 0.1	3.122 ± 0.006
64	31.65 ± 0.12	2421 ± 1.4	1610 ± 0.1	3.796 ± 0.007
80	37.62 ± 0.14	2592 ± 1.5	1623 ± 0.1	4.536 ± 0.007
100	42.90 ± 0.16	2707 ± 1.6	1615 ± 0.1	5.111 ± 0.008

Table 4.3: Data regarding the minimal detected current using the SensL 9k detector. Signal and baseline mean values and their errors are in QDC counts. Integration time t_{gate} is 5000 ns.

Exposure [mAs]	Dose Rate [mGy/s]	Signal	Baseline	Current [μA]
100	194.9 ± 1.5	3415 ± 1.9	266 ± 0.05	147.40 ± 0.09
80	163.7 ± 1.3	2987 ± 1.9	267 ± 0.05	127.32 ± 0.09
64	137.0 ± 1.1	2586 ± 1.7	269 ± 0.05	108.46 ± 0.08
50	109.6 ± 0.9	2186 ± 1.6	270 ± 0.05	89.69 ± 0.07
40	89.8 ± 0.7	1858 ± 1.5	272 ± 0.05	74.24 ± 0.07
32	73.0 ± 0.6	1592 ± 1.2	273 ± 0.05	61.74 ± 0.06
25	59.7 ± 0.5	1369 ± 1.2	273 ± 0.05	51.30 ± 0.06
20	48.7 ± 0.4	1183 ± 1.0	273 ± 0.05	42.60 ± 0.05
16	40.0 ± 0.3	1032 ± 1.0	275 ± 0.05	35.43 ± 0.05
12	33.7 ± 0.3	913 ± 0.8	276 ± 0.05	29.82 ± 0.04
10	24.2 ± 0.2	748 ± 0.8	276 ± 0.05	22.09 ± 0.04
08	17.8 ± 0.1	641 ± 0.7	278 ± 0.05	16.99 ± 0.03
05	9.8 ± 0.1	483 ± 0.5	279 ± 0.05	9.55 ± 0.03
04	6.6 ± 0.1	431 ± 0.5	281 ± 0.06	7.02 ± 0.02

Table 4.4: Data regarding the maximal detected current using the SensL 9k detector. Signal and baseline mean values and their errors are in QDC counts. Integration time t_{gate} is 500 ns.

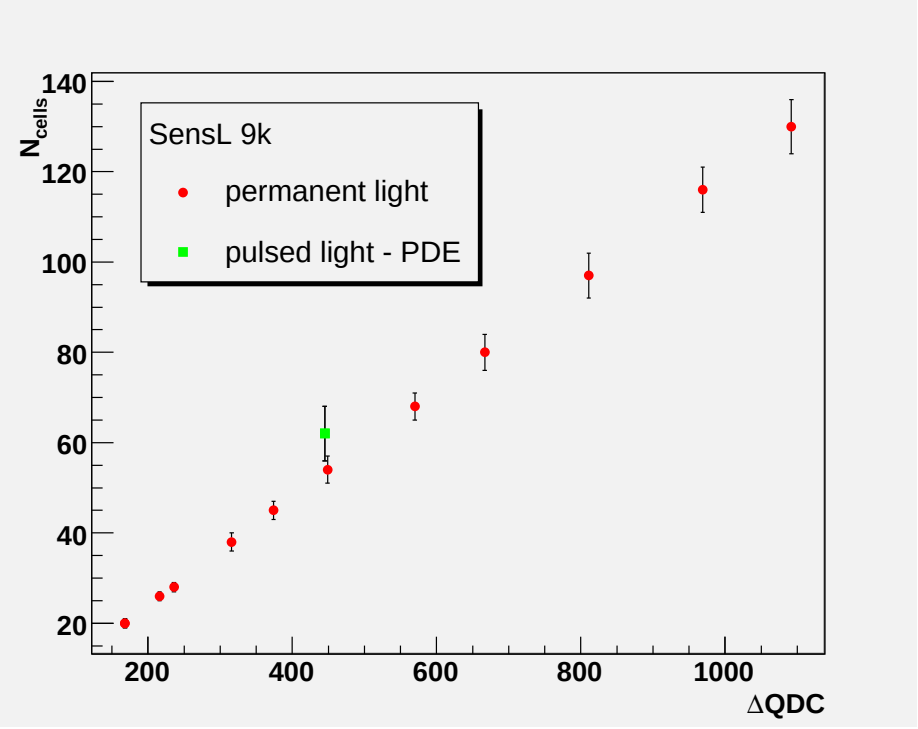

Figure 4.3: Number of triggered cells evaluated for the data presented in Table 4.3 (red dots) and for the cross-check experiment with pulsed light (green square). Flux of pulsed light has been measured with the HAMAMATSU H5783 Photo Multiplier and counts $\sim$ 1900 photons per pulse.

A cross-check has been performed by illuminating the sensor with a single pulse of light of known flux and measuring the QDC output: the number of fired cells has then been evaluated multiplying the flux by the SensL 9k PDE; the result has also been showed in Figure 4.3, proving the consistency of the procedure. Therfore, from the outlined procedure, it emerged clearly that the sensor informally called SensL 9k fulfilled the MAMMODOS specifications in terms of electrical current for the dose rate of interest. Concerning the sensor performance, the SensL 9k scores a significant result, being its linearity proven till a Geiger-Mueller avalanche frequency up to 800 MHz.

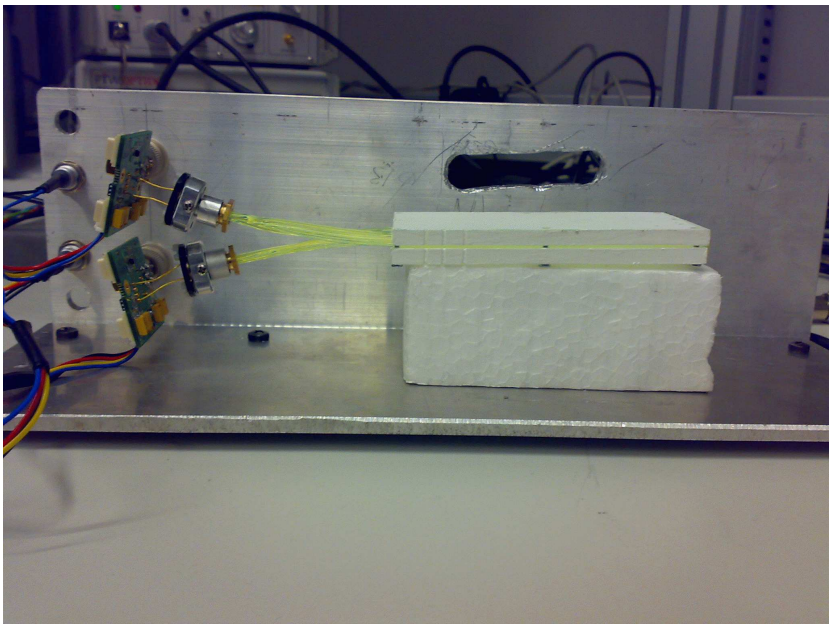

Figure 4.4: The Radon meter detection apparate prototype: a ZnS foil is enclosed between two plastic holders and put in contact with WLS fibers which deliver light to two SiPMs.

4.2.2 RADIM 7: measurement of ambiental Radon concentration

Measurements of ambiental Radon concentration are main issues for what concerns occupational safety and health; these kind of detectors are meant to be placed in close ambients for several days, in order to acquire enough statistics to provide a reliable measurement.
Concentration measurements are performed via detection of alpha particles emitted by Radon decay; thus, the prototype of the detection part of the RADIM 7 consisted in ZnS foil, sensible to alpha particles, coupled with WLS fibers, delivering light to two SiPMs, whose characteristics have to be compliant with a pulsed light regime (in contrast to the requirement for the MAMMODOS, which was meant to be operated under a constant light flux).
The main issue related with this detector is the fact that Radon concentration is tipically quite low, so global Radon alpha emission in a close ambient is a low rate process (*Agenzia Regionale per la Protezione Ambientale* - ARPA[11], fixed to 150 Bq/m^3 the ward level of Rn concentration): thus dealing with *false positives* was the main problem to solve, in order to archieve the desired low flux sensitivity.

[11] documents can be found online on http://ita.arpalombardia.it/

Threshold (p.e.)	with source (kHz)	w/out source (kHz)
1.5	195.12	229.27
2	181.71	130.49
2.5	102.44	74.27
3	49.76	13.17
3.5	32.93	5.73
4	17.93	1.24
4.5	12.78	0.36
5	10.88	0.09
5.5	10.29	0.02

Table 4.5: In this table coincidence measurements are presented. Coincidence frequency had been measured, both with and without alpha source (^{241}Am), varying the comparator threshold for both sensors: threshold values are expressed in *photoelectrons* (p.e.), meaning that comparator had been set to a voltage level adequate to neglect the output of a number of simultaneous avalanches corrsponding to the threshold level. Increasing the treshold level, the coincidence counts measured without source decrease, while the counts with alpha source reach a plateau value.

An exhasutive discussion on the technique used in order to obtain a close-to-zero false positive condition is not possible, since it is partially covered by a non-disclosure agreement; however, an important part of this mechanism can be described and consisted in using the two SiPMs in coincidence mode, coupling each one with a threshold discriminator: optimizing the threshold level could then allow to neglet enough stocastic events (i.e. thermally generated avalanches), to reach an adequate signal-to-noise ratio. This can be easily explained: the coincidence frequency ν_C of stocastic events is given by

$$\nu_C \;=\; \nu_A\,(1-\mathrm{P}_B(0)\,)\;+\nu_B\,(1-\mathrm{P}_A(0)\,), \tag{4.4}$$

where $\nu_{A,B}$ is the DCR of the sensor A and B respectively and $\mathrm{P}_{A,B}(0)$ is the probability of no dark count events from the sensor A and B respectively, occuring during the coincidence gate time t_C. Assuming a poissonian probability distribution for the dark count events, the previous expression becomes

$$\nu_C \;=\; \nu_A\,(1-\mathrm{e}^{-\nu_B t_C})\;+\nu_B\,(1-\mathrm{e}^{-\nu_A t_C})\;\simeq\;2\,\nu_A\nu_B t_C. \tag{4.5}$$

So, lowering the the DCR of each sensor (for example increasing the triggering threshold), the stocastic coincidence dark count rate falls quadratically.
These requirements guide the choice of the optimal SiPM:

- sensors with low values of DCR are preferable;
- to optimize the efficiency of the alpha detection, high PDE levels are also highly desirable;

- since Radon detectors are left on the site of measurement for several days of continuos data acquisition, they are exposed to temperature variations which influence Photo-Detection Efficiency and gain: since comparator thresholds do not change, uncontrolled gain variations can dramatically worsen the signal-to-noise ratio; thus a clear knowledge of the temperature behaviour of SiPMs is of utmost importance;

A first proof-of-principle test had been performed using un alpha emitting source ^{241}Am, changing comparator threshold in order to measure the same over threshold dark counts for both SiPMs: results, performed at room temperature are shown in Table 4.5: it is clear how, increasing the threshold, the rate of stochastic coincidence events decrease, while the rate of alpha detection events reaches a plateau.
These first tests seemed to confirm that the SensL 9k characteristics matched with the operational requests for the Radon-meter.
Still, behaviour of gain and PDE at varying temperature remained an open issue that could invalidate the SiPM choice: a too steep temperature dependence of chosen SiPM parameters could make the realization of the prototype unfeasible.

Threshold (p.e.)	Counts (Hz)				
	^{57}Co	^{241}Am	^{137}Cs	^{60}Co	no source
3.5	46.15	634.1	2927	-	35.6
4.5	15.38	451.9	2683	103.4	5.76
5.5	12.5	426.9	2634	101	5.00
	Activity (kBq)				
	37	40	185	37	-

Table 4.6: Coincidence frequencyes measured for four different radionuclides for different thresholds; threshold values are expressed in *photoelectrons*, meaning the comparator had been set to a level adequate to neglet the output corresponding to number of simultaneous avalanches lower than the threshold value. It is clear that increasing threshold values, the coincidence frequencies reach a plateu (different for each isotope due to different activity values and different decay energies), meaning that stocastic events are almost entirely neglected. The presence of a plateau value for dark count coincidence suggested the possibility of a slight radioactive contamination of the scintillating crystal.

4.2.3 The Snooper: illicit radiocative material detection

The detector for illicit radioactive material called *Snooper*, was intended to be a portable detector for homeland security application, capable of signaling the presence of alpha, beta and gamma emitting radiocative materials, just after a quick probing.
As in previous projects, operationals requirements for the detectors have an impact on the SiPM parameters:

- ISO standard require a minimal dose rate which should trigger an alarm, corresponding to 0.4 μSv/h after 3 s of investigating time; thus, to match with this requirement, an high PDE value is of grat importance;

- due to the expected brief sampling time, the presence of false positive could generate problems and should be kept as low as possible;

- as the detector is meant to be portable, indoor-outdoor temperature variations do not have to affect the efficiency of the instrument: performances should not change within a temperature range varying from -15 °C up to + 45 °C.

To match these requirements, expecially the low flux sensitivity, a coincidence setup analogue to the one used for the Radon-meter had been used, using a scintillating crystal to convert alpha, beta and gamma radiation into visible light to be detected by the SiPMs.
Since the minimal detectable dose was a main issue, SiPMs had been chosen with large area, in order to maximize cristal emitted light collection; on the other hand, as previously explained, these sensors posses higher DCR values,

worsening the noise of the detector. Thus, to test the coincidence setup, a threshold scan had been performed, using four different radionuclides of known activity and the results are shown in Table 4.6, proving in this case as well how increasing the sensor signal threshold allows to easily get rid of the dark count coincidence events. From this proof-of-principle, the feasibility of the device clearly emerges, since over a certain threshold the entire dark count contribution to the triggered events is neglected; still, temperature behaviour remains an open problem.

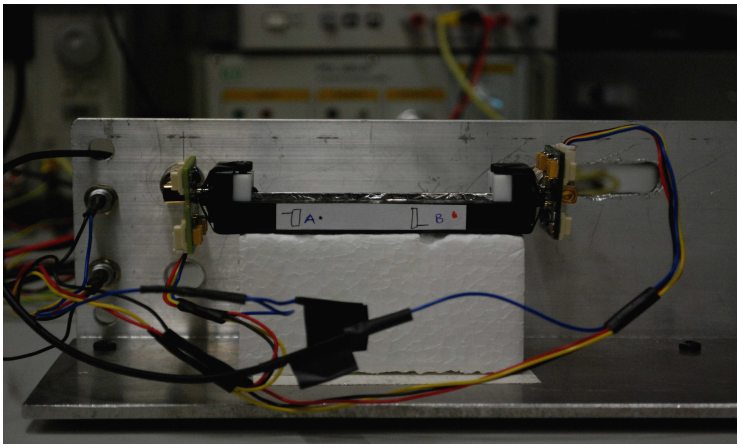

Figure 4.5: The Snooper detection part prototype: a polished YAP crystal with square cross section, enveloped in a mylar foil is put direct contact with two SiPMs.

4.3 Studying temperature behaviour

In order to understand quantitatively the effects of temperature changes on SiPM main figures of merit, a dedicated set of measurements had to be accomplished. Procedure had been tested with SensL CSI 0747 015 A20 HD (whose characteristics at room temperature listed previously in Tab. 4.1) and results regarding this sensor will be presented in more detail in the following subsections. Once the procedure had been tested, it had been repeated with different SiPM models: a SensL CSI 0740 001 A20 HD, an Hamamatsu S10362-11-100C and an ST Microelectronics TO-8 prototype.
Sensors had been placed in the cooling box described in section 4.1.1, and different spectra had been acquired at different bias voltages and different temperatures for gain and PDE measurements, along with DCR measurements at different tresholds, useful for DCR and cross-talk evaluation.

In order to describe with deeper detail the procedure, a typical low-flux spectrum is shown in Fig. 4.7. The histogram is composed by the charge measure-

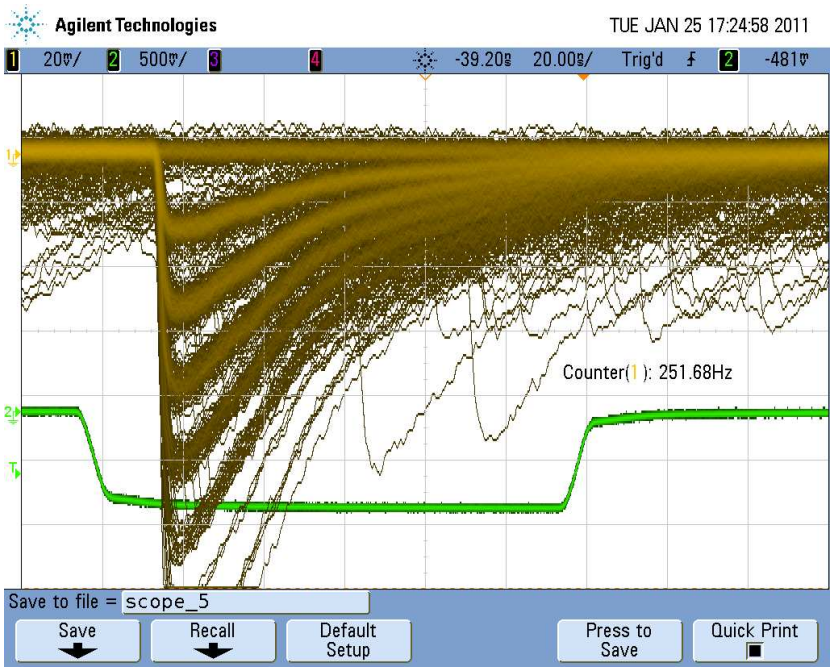

Figure 4.6: Oscilloscope screenshot of the negative voltage output of a SiPM (yellow), illuminated by a pulsed light source triggered by a NIM signal (green), which is also used as integration gate. Several equally spaced curves can be clearly recognized in the SiPM signal, progessively corresponding to the simultaneous firing of one, two, three (and so on) cells; the area subtended by the first curve is proportional to the SiPM gain, while the width of each curve is proportional to the stochastic noise of the device.

ments performed by the CAEN QDC of the output signal of the SiPM under study: a waveform generator triggered both the light source and the *gate* needed to perform the charge measurement (see Fig. 4.6). Thus the structure of the histogram reflects the characteriscs of the SiPM, since the n-th peak position represents the most probable output value (in released charge) of n cells firing simultaneuosly and its gaussians broadening is due to stochasitc noise sources; in this experimental situation, the very first peak represents the *zero-photon* peak, i.e. the output of the QDC board with no SiPM signal. Thus, the broadening of the n-th peak σ_n can be with good approximation described with the following relation:

$$\sigma_n^2 = \sigma_0^2 + n\sigma_1^2, \tag{4.6}$$

where σ_0 is the variance of the zero-photon peak, estimating the noise contibution due to the electronic chain, and σ_1 is the variance of the first photon peak, providing an estimation of the noise relative originated by the SiPM itself.

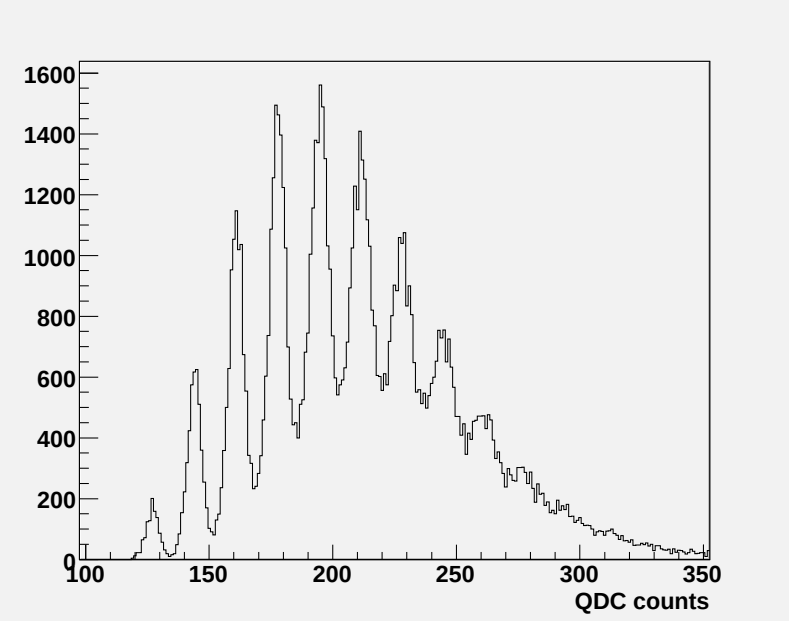

Figure 4.7: Example of low flux spectrum of a SiPM; each histogram bin represent a single QDC channel, thus representing a charge measurement, precisely 0.11 pC per channel.

4.3.1 Gain

Gain had been evaluated by illuminating the SiPM with low photon flux, thus obtaining a spectrum whose peaks are clearly recognizable: an example is shown in Fig. 4.7. As the n-th peak corresponds to the mean charge released by n Geiger-Müller avalanches, gain calculation has been straightforward, using the following relation:

$$G = \frac{QDC_{cal}}{e^- K_{amp}} \Delta_{PP}, \tag{4.7}$$

where G is the gain, $QDC_{cal} = 0.11$ pC/channel is the charge corresponding to one QDC unit, e^- is the elementary charge, K_{amp} is the global amplification factor of the electronic setup, and Δ_{PP} is distance in QDC units between two adjacent peaks of the collected spectra.
In Fig. 4.8 the behavior of gain with bias voltage, at fixed temperatures, is shown: a linear dependence in the range of interest is clearly observable and varying temperature does not affect the slope of the extrapolated curves, within the experimental errors. In Fig. 4.9 the same gain values are presented as function of the temperature, for fixed bias voltage: a linear behavior is still clearly recognizable; in this case as well slope is not affected by the change of applied bias.
This analysis suggests that gain can be expressed as a linear function of a

SiPM Model	m_{BD} (mV/degree)
SensL CSI 0747 015 A20 HD	23.2 ± 1.4
SensL CSI 0740 001 A20 HD	23.6 ± 0.9
Hamamatsu S10362-11-100C	61.9 ± 0.7
STM T0-8 prototype	31.5 ± 0.1

Table 4.7: In this table are presented, for different SiPM models, obtained values of the breakdown voltage rate of change with temperature; it obviously emerges how these values are technology dependent: infact, the ones built by the same producers with the same method present an almost identical value.

variable which can be re-scaled with temperature; since it is well known that breakdown voltage has, in our range of interest, a linear dependence from temperature [20], the over voltage, defined as the difference between the applied bias voltage and the breakdown, is thus a suitable candidate.
The mentioned condition can be summarized in the equations

$$G(V,T) = m_V(V - V_{BD}(T)), \tag{4.8}$$
$$G(V,T) = m_T T + G(T_0,V), \tag{4.9}$$
$$\tag{4.10}$$

where m_V and m_T are the slopes of curves representing the gain as function, respectively, of the bias voltage and of the temperature, while $V_{BD}(T)$ is the breakdown voltage and T_0 is a reference temperature. Solving simultaneously these equations for $V_{BD}(T)$, the rate of change of the breakown voltage with temperature has been found as given by

$$m_{BD} = -\frac{m_T}{m_V}. \tag{4.11}$$

This same procedure had been applied to every SiPM that needed a characterization of the temperature behaviour. As clearly appears from the results listed in Tab. 4.7, the values of m_{BD} are technology dependent.

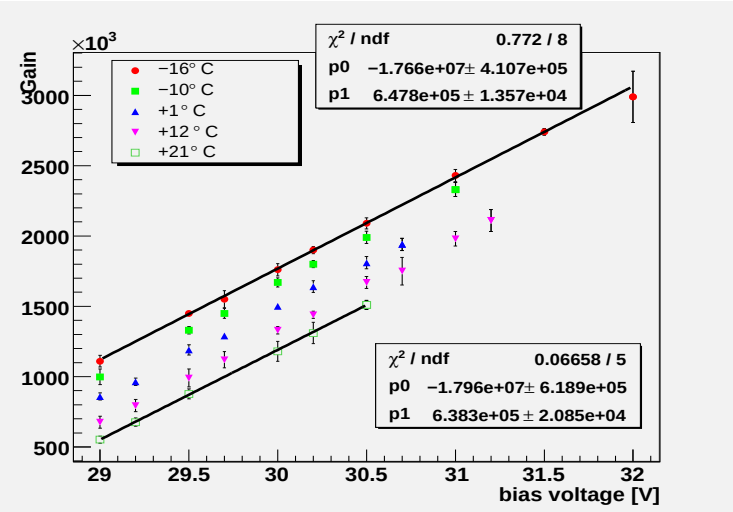

Figure 4.8: Gain values plotted as function of bias voltage, for different temperatures; a linear fit had been performed for each temperature set: obtained fit slopes show compatible values.

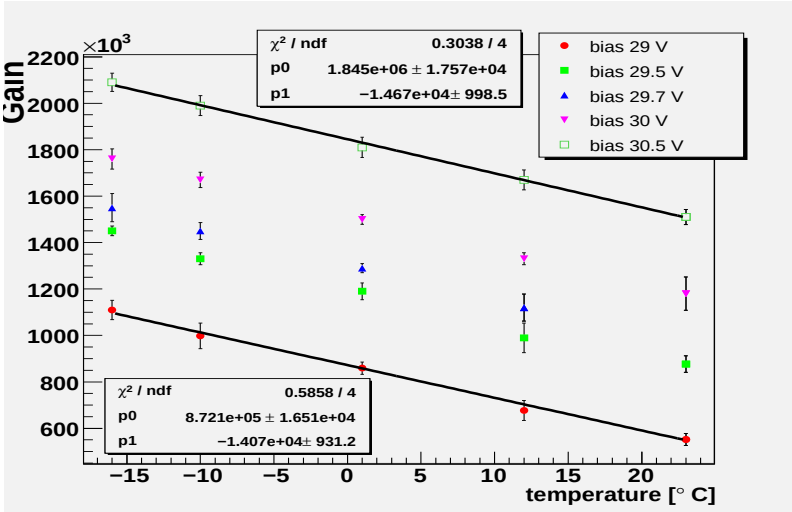

Figure 4.9: Gain had been plotted as function of temperature (expressed in Celsius degrees), for fixed bias voltages; each set had been fitted using a linear law: obtained slopes show compatible values.

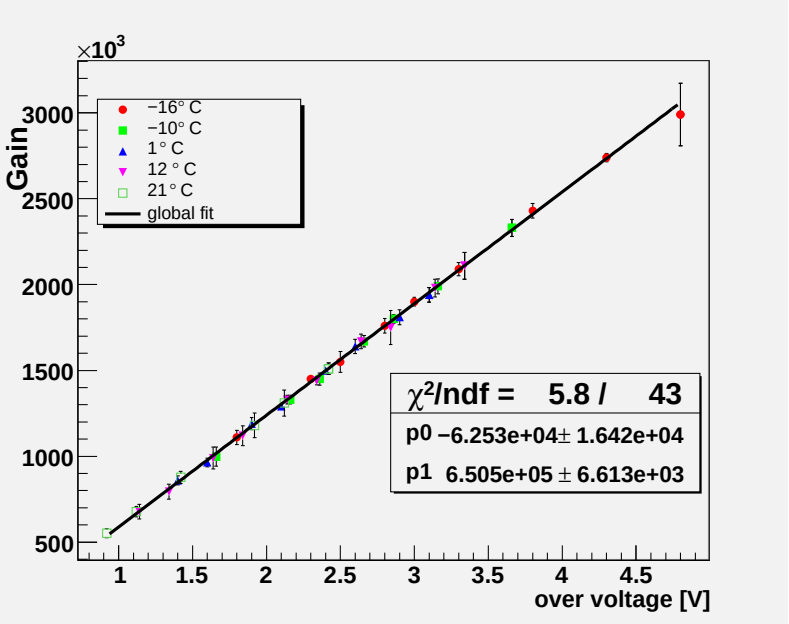

Figure 4.10: Gain plotted as a function of the over voltage values obtained calculating breakdown voltage for each temperature; all the data set acquired at different temperatures had been fitted with the same linear law.

Thus, using breakdown voltage value measured at room temperature (RT) as a reference value, breakdown values for each temperature can be calculated by rewriting Equation 2.40 as:

$$V_{BD}(T) = \mathrm{m}_{BD}(T - T_{RT}) + V_{BD}(T_{RT}); \tag{4.12}$$

using the above equation it is possible to express the gain and all the other measured parameters as a function of the over voltage: in Fig. 4.10 gain has been plotted versus over voltage, showing a global linear behavior indipendent from the temperature.
Equation 4.12 can be profitebly adoperated to stabilize the operational parameters of a SiPM againist varying environmental conditions: if m_{BD} is known with enough precision and frequent measurements of the SiPM temperature are preformed, the overvoltage across each cell can be maintained fixed simply continuously adjusting the applyed bias according to the temperature variations; this idea led to a collaboration between Università dell'Insubria and CAEN, for the realization of CAEN SP5600 General Purpose Power Supply and Amplification Unit module with an integrated threshold discriminator.

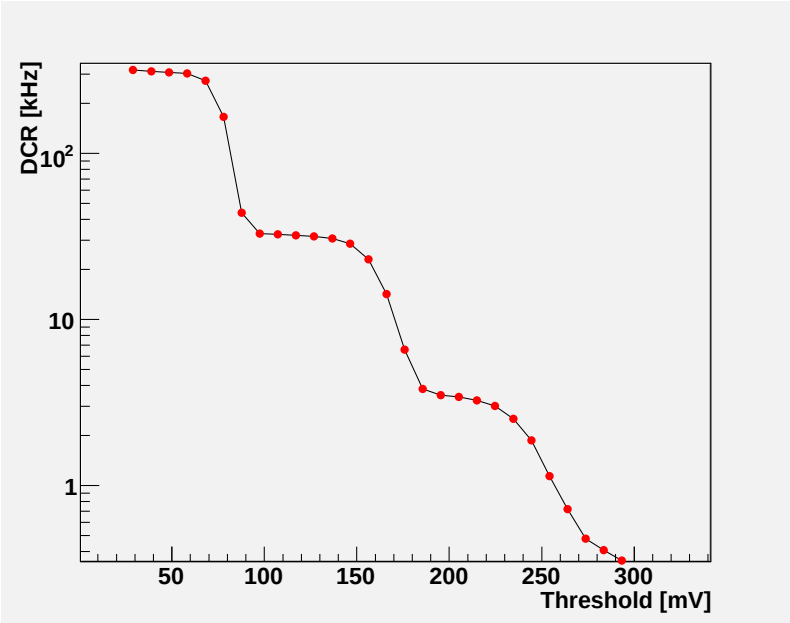

Figure 4.11: Example of *staircase curve*, obtained after three-stage amplification.

4.3.2 Dark Count Rate

As explained in section 3.3, Dark Count Rate (DCR hereon) is the frequency of the Geiger-Müller avalanches triggered by thermally extracted carriers. A scan of the DCR at different threshold can be done, and the resulting plot (an example is shown in Fig. 4.11) is characterized by a serie of plateaus whose value decreases sharply (tipically one order of magnitude in frequency) for precise thresholds: this corresponds to settings of the discriminator higher than the output signal respectively of the first photon, the second and so on: this kind of plots are usually referred to as *staircase functions*.
DCR has been measured at different voltages and different temperatures, also setting different discrimination thresholds; in Fig 4.12, for example, results for *"half photon threshold"*[12] are shown. A clear and expected dependance from temperature is recognizable, as recalled in section 3.3.
An exhaustive knowledge of the DCR behaviour is of utmost importance, for a complete characterization of all the sources of noise of the detector; in particulare, as shown in previous sections, it can be a fundamental figure of merit for low flux applications.

[12]The discriminator has been regulated with a threshold corresponding to half the output signal of the first photon.

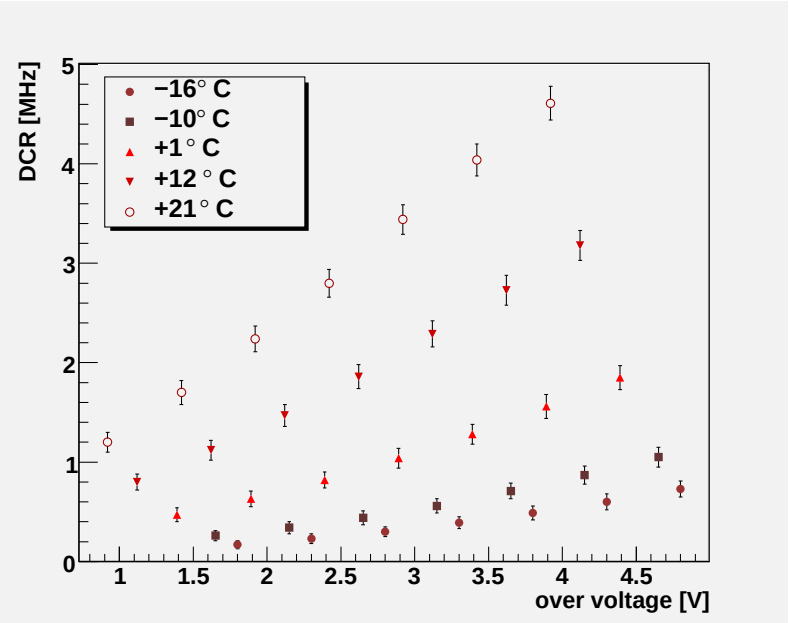

Figure 4.12: DCR at different temperatures rescaled as function of the over voltage, for a SensL SiPM.

4.3.3 Optical cross-talk

An electron avalanche is modelized as a microplasma; photons emitted by plasma during this event have a certain probability to reach the neighbour cell diodes and trigger a second avalanche: thus, the quantity named optical cross-talk (for brevity simply cross-talk or X_T hereon) is simply the percentage of avalanches triggered by such a mechanism.
Cross-talk has been calculated starting from DCR measurements, using Equation 3.11, that is taking the ratio between the DCR frequencies measured setting the discriminator threshold respectively at *"one-and-half photon"* and at *"half photon"*. This method is based on the assumption that the probability that two uncorrelated avalanches are triggered within the same rise time is negligible, so that all the second photon events are due to cross-talk.
In Fig. 4.13 results of cross-talk evaluation are displayed: it is worth noticing that, within experimental errors, cross-talk does not seem to possess a strong temperature dependance.

4.3.4 Photo-Detection Efficency

Photo-Detection Efficiency (PDE) is a key parameter for every light detector and, according to Equation 3.2, it is defined as the product of three terms:

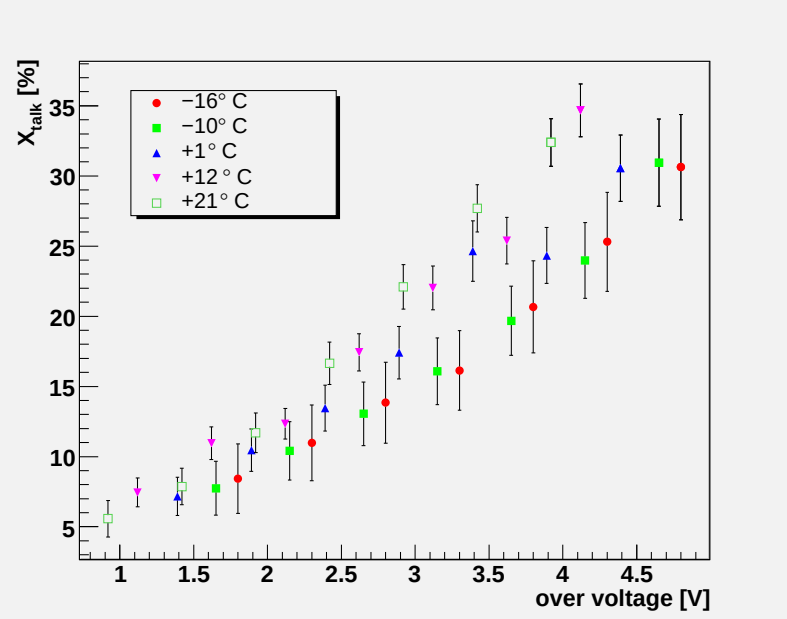

Figure 4.13: Cross-talk values plotted as function of the over voltage, at different temperatures, for a SensL SiPM.

- Quantum Efficiency, the probability that the impinging photon produces a charge carrier and it is a function of the incoming light wavelenght;

- the Geiger-Müller probability that the extracted carrier generates an avalanche, and depends on the over voltage;

- the so called Fill Factor (FF), a geometrical factor which express the fraction of the active area of the sensor, respect to the total area;

PDE value thus represents the fraction of impinging photons that are detected. To measure this quantity, SiPMs have been illuminated with light whose intensity Φ had been previously measured with a calibrated PMT HAMAMATSU H5783 and then resulting spectra have been acquired; PDE has thus been evaluated estimating the mean number of measured photons $< n >_{meas}$ divided it by the incoming light intensity:

$$PDE = \frac{< n >_{meas}}{\Phi}. \tag{4.13}$$

In case of spectra where each photon peak could be resolved, $< n >_{meas}$ has been evaluated by fitting the peak positions with a Poissonian curve and then evaluating the mean value of the fit result distribution. In case peaks could not

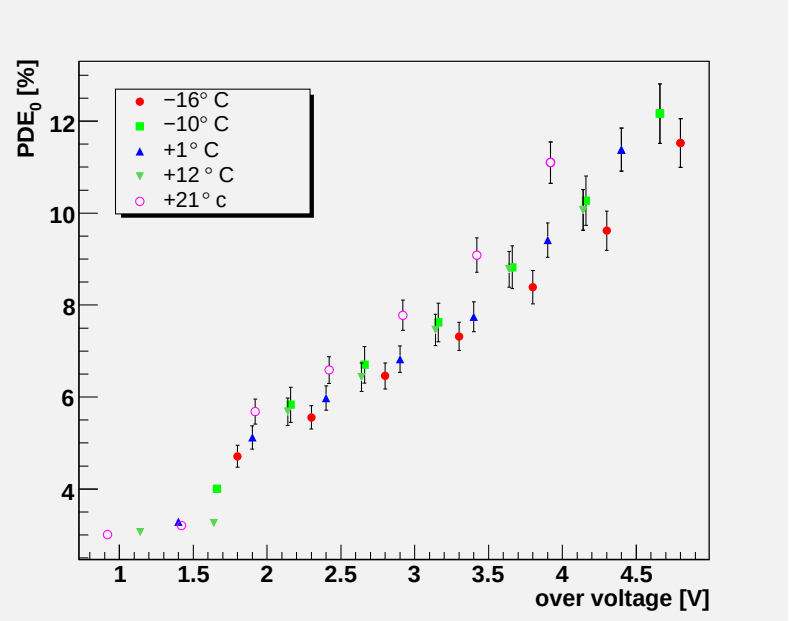

Figure 4.14: PDE values corrected taking into account cross-talk effects, for a SensL SiPM. Wavelenght of impinging light is 510 nm.

have been resolved, $< n >_{meas}$ has been extimated using

$$< n >_{meas} = \frac{QDC_{cal}}{e^- \, G \, K_{amp}} \Delta QDC, \tag{4.14}$$

where G is the proper gain value, e^- is the elementary charge, $QDC_{cal} = 0.11$ pC is the charge per QDC unit, K_{amp} is the amplification factor of the electronic chain, and ΔQDC is the difference between the mean value of the obtained spectrum and the pedestal position.
This method, howevever, provides a zero-order approximation of the PDE because it does not take into account cross-talk effects that can be as large as 40% (see again Fig. 4.13 as a reference). To properly estimate the *"real"* number $< n >_0$ of impinging photons triggering an avalanche,the following relation has been used:

$$< n >_{meas} = \frac{< n >_o}{1 \, - \, X_T} \simeq < n >_o (1 \, + \, X_T), \tag{4.15}$$

the approximation valid for small values of cross-talk; PDE values previously obtained have thus been corrected using $< n >_0$ as the mean number of detected photons as shown in Fig. 4.14. Again, PDE_0 does not seem to have any remarkable temperature dependance, thus confirming the consistency of our results with the definition of PDE.

Chapter 5

The output of SiPMs: a statistical description

Charcterization is an important step in knowledge of SiPM technology, but nonetheless it is just the first one. A further advancement in our studies on SiPMs had been originated when the applicability of SiPMs as detectors in Quantum Optics experiments had been tested: in particular, SiPMs had been used in experiments aiming at the reconstruction of probability distribution of light fields.
Adopting these devices in such measurements proved to be an intriguing challenge: their high photon number resolution capability is an advantageous feature, but the detectors themselves posses a behaviour significantly disclose from the ideal bernoullian detection process, principally due to the presence of relevant DCR and optical cross-talk; therefore, in order to properly reconstruct the light field probability distribution, the contibution of these two effects to the detector response had to be modelized.

Since the actual measurement concerns the output of the SiPM, providing a description of the probability distribution functions of the geiger-Müller avalanches had been necessary in order to trace back to the statistic of the impinging light:

1. incoming light on the detector generates a certain number of G-M avalanches by *"ordinary detection"*, the whole process governed by detector PDE;

2. DCR also contributes, because during integration time additional avalanches are thermally generated and thus measured;

3. last, all the avalanches generated by detection and thermal extraction can trigger additional events in neighbour cells by optical cross-talk: moreover, these latter can themselves ignite neighbour cells in a cascade behaviour which could not be trivial to describe.

Once obtained a phenomenological mathematical expression of the probability distribution of the G-M avalanches, two parallel and somehow complementary pahts had been followed in order to analyze experimental data:

- a first procedure, called *Method I*, elaborated principally by the authors of [36], which represents the generalization of the technique illustrated in the same paper: this method is based on the explicit calculation of a mathematical expression of the first three momenta of the probablity distribution function;
- the other procedure, *Method II*, is based on the analysis of the peak-resolving spectra and the fit of the obtained data about the statistics of the G-M avalanches with the mathematical expression of the probability distribution functions.

5.1 Detector response modelling

The response of an ideal detector to a light field can be described in a simple way as a bernoullian process:

$$B_{m,n}(\eta) = \left(\begin{array}{c} n \\ m \end{array} \right) \eta^m (1-\eta)^{n-m} \ . \tag{5.1}$$

being n the number of impinging photons over the integration time, m the number of detected photons and $\eta < 1$ the photon-detection efficiency. Actually, η is a single parameter quantifying detector effects and losses (intentional or accidental) which can be tracked to the optical system. As far as SiPM are concerned, detector effects are due to the quantum efficiency, the fill factor and the avalanche triggering probability, namely the probability for a charge carrier to develop a Geiger-Mueller quenched discharge [16, 21]. As a consequence, the distribution $P_{m,\mathrm{det}}$ of the number of detected photons, that is the GM avalanches actually corresponding to a detected photon, triggered by a photo-electron has to be linked to the distribution $P_{n,\mathrm{ph}}$ of the number of photons in the light under measurement by [37, 38, 39]:

$$P_{m,\mathrm{det}} = \sum_{n=m}^{\infty} B_{m,n}(\eta) P_{n,\mathrm{ph}} \ . \tag{5.2}$$

It can be demonstrated [40] that for a combination of classical light states the statistics is preserved by the primary detection process.

This simple description has to be further developed to link $P_{m,\mathrm{det}}$ to the probability density distribution of the GM avalanches of any origin. First we must take into account spurious hits and cross-talk effects, not negligible in the detectors being studied. The dark count rate results in a poissonian process which can be described as:

$$P_{m,\mathrm{dc}} = \overline{m}_{\mathrm{dc}}^m / m! \exp(-\overline{m}_{\mathrm{dc}}) \ , \tag{5.3}$$

where $\overline{m}_{\rm dc}$ is the mean number of dark counts during the gate window (or integration time) and $\sigma^{(2)}_{m,\rm dc} = \sigma^{(3)}_{m,\rm dc} = \overline{m}_{\rm dc}$.

As a consequence, the statistics of the recorded pulses may be described as:

$$P_{m,\rm det+dc} = \sum_{i=0}^{m} P_{i,\rm dc} P_{m-i,\rm det} \ , \tag{5.4}$$

obviously shifting the mean value and increasing variance and third-order central moment according to

$$\begin{aligned}
\overline{m}_{\rm det+dc} &= \overline{m}_{\rm det} + \overline{m}_{\rm dc}, & (5.5)\\
\sigma^{(2)}_{m,\rm det+dc} &= \sigma^{(2)}_{m,\rm det} + \sigma^{(2)}_{m,\rm dc} = \sigma^{(2)}_{m,\rm det} + \overline{m}_{\rm dc}, & (5.6)\\
\sigma^{(3)}_{m,\rm det+dc} &= \sigma^{(3)}_{m,\rm det} + \sigma^{(3)}_{m,\rm dc} = \sigma^{(3)}_{m,\rm det} + \overline{m}_{\rm dc}. & (5.7)
\end{aligned}$$

As a further step, cross-talk effects shall be taken into account. Cross-talk is a genuine cascade phenomenon that can be described at first order as [41]

$$C_{k,l}(x_t) = \left(\begin{array}{c} l \\ k-l \end{array} \right) x_t^{k-l} (1-x_t)^{2l-k} \ . \tag{5.8}$$

being x_t the (constant) probability that the GM avalanche of a cell triggers a second cell (which becomes equivalent to the cross-talk probability X_T in the limit of $X_T \to 0$), l the number of dark counts and photo-triggered avalanches and k the actual light signal amplitude.

Within this first-order approximation, the actual sensor response is described by

$$P_{k,\rm cross} = \sum_{m=0}^{k} C_{k,m}(x_t) P_{m,\rm det+dc} \ , \tag{5.9}$$

characterized by

$$\begin{aligned}
\overline{k}_{\rm cross} &= (1+x_t)\overline{m}_{\rm det+dc}, & (5.10)\\
\sigma^{(2)}_{k,\rm cross} &= (1+x_t)^2 \sigma^{(2)}_{m,\rm det+dc} + x_t(1-x_t)\overline{m}_{m,\rm det+dc}, & (5.11)\\
\sigma^{(3)}_{k,\rm cross} &= (1+x_t)^3 \sigma^{(3)}_{m,\rm det+dc} + 3x_t(1-x_t^2)\sigma^{(2)}_{m,\rm det+dc} + \\
&+ x_t(1-3x_t+2x_t^2)\overline{m}_{m,\rm det+dc}. & (5.12)
\end{aligned}$$

In the following we refer to this analytical model as *Method I*. We also consider a better refined model (*vide infra*, *Method II*) offering, in principle, an extended range of application but paying the price of being limited to a numerical rather than analytical solution.

Irrespective of the model, the amplification and digitization processes that produces the output x can simply be described as a multiplicative parameter G:

$$P_{x,\rm out} = G P_{Gk,\rm cross} \ , \tag{5.13}$$

conveniently scaling the momenta as $\overline{x}_{\rm out} = G\overline{k}_{\rm cross}$, $\sigma^{(2)}_{x,\rm out} = G^2 \sigma^{(2)}_{k,\rm cross}$ and $\sigma^{(3)}_{x,\rm out} = G^3 \sigma^{(3)}_{k,\rm cross}$.

5.1.1 Method I: an analytical evaluation of the second and third order momenta

This approach extends the method presented in [36] to detectors with a significant dark count rate and first order cross-talk effects. Experimentally, it is based on the detection of a light field performed by varying, in a controlled way, the optical losses , i.e. η, with detector parameters presumed to be constant throughout the η scan.

The second-order momentum of the recorded pulse distribution $P_{x,\mathrm{out}}$ can be used to evaluate the Fano factor:

$$\begin{aligned} F_{x,\mathrm{out}} &= \frac{\sigma^{(2)}_{x,\mathrm{out}}}{\overline{x}_{\mathrm{out}}} = G\frac{\sigma^{(2)}_{k,\mathrm{cross}}}{\overline{k}_{\mathrm{cross}}} \\ &= G(1+x_t)\frac{\sigma^{(2)}_{m,\mathrm{det+dc}}}{\overline{m}_{\mathrm{det+dc}}} + G\frac{x_t(1-x_t)}{1+x_t} \\ &= \frac{Q_{\mathrm{det+dc}}}{\overline{m}_{\mathrm{det+dc}}}\overline{x}_{\mathrm{out}} + G\frac{1+3x_t}{1+x_t}\ , \end{aligned} \tag{5.14}$$

where $Q_{\mathrm{det+dc}} = \sigma^{(2)}_{m,\mathrm{det+dc}}/\overline{m}_{\mathrm{det+dc}} - 1$ is the Mandel factor of the primary charges. Note that, due to dark-counts, the coefficient of $\overline{x}_{\mathrm{out}}$ in Eq. (5.14) cannot be written as $Q_{\mathrm{ph}}/\overline{n}$ [36, 42], that is, the coefficient $Q_{\mathrm{det+dc}}/\overline{m}_{\mathrm{det+dc}}$ does not only depend on the light field to be measured.

Similarly we can calculate a sort of symmetry parameter

$$\begin{aligned} S_{x,\mathrm{out}} &= \frac{\sigma^{(3)}_{x,\mathrm{out}}}{\overline{x}_{\mathrm{out}}} = G^2\frac{\sigma^{(3)}_{k,\mathrm{cross}}}{\overline{k}_{\mathrm{cross}}} \\ &= G^2(1+x_t)^2\frac{\sigma^{(3)}_{m,\mathrm{det+dc}}}{\overline{m}_{\mathrm{det+dc}}} + 3G^2x_t(1-x_t)\frac{\sigma^{(2)}_{m,\mathrm{det+dc}}}{\overline{m}_{\mathrm{det+dc}}} + G^2\frac{x_t(1-3x_t+2x_t^2)}{1+x_t} \\ &= \frac{Q_{s,\mathrm{det+dc}} - 3Q_{\mathrm{det+dc}}}{\overline{m}^2_{\mathrm{det+dc}}}\overline{x}^2_{\mathrm{out}} + G\frac{1+3x_t}{1+x_t}\frac{Q_{\mathrm{det+dc}}}{\overline{m}_{\mathrm{det+dc}}}\overline{x}_{\mathrm{out}} + G^2\frac{1+7x_t}{1+x_t}\ , \end{aligned} \tag{5.15}$$

where $Q_{s,\mathrm{det+dc}} = \sigma^{(3)}_{m,\mathrm{det+dc}}/\overline{m}_{\mathrm{det+dc}} - 1$.

Note that in the presence of dark-counts both coefficients $(Q_{s,\mathrm{det+dc}} - 3Q_{\mathrm{det+dc}})/\overline{m}^2_{\mathrm{det+dc}}$ and $Q_{\mathrm{det+dc}}/\overline{m}_{\mathrm{det+dc}}$ are no-more independent of the light under measurement [40]. We will see how this modifies the results in the following examples involving classical light states for which the statistics of detected photons is the same as that of photons.

A validation and a comparison of the proposed model was performed by sampling coherent and multi-thermal light fields, where the proposed model can be specified as follows.

5.1.2 Method II: a numerical evaluation based on the photon-number resolving properties of SiPM

The above mentioned self-consistent method is very powerful, but requires the acquisition of several histograms at varying η, which could not always be easy to perform, or possible at all, in many practical applications: from this point of view, the possibility to analyze each spectrum independently looks complementary to the self-consistent approach. This analysis had been performed with a two-step procedure:

- the areas of the spectrum peaks had been measured, thus obtaining an estimation of the number of counts per peak;
- the obtained data points had been fitted with a theoretical function, which takes into account the statistics of light, detection and all deviations of the detectors from ideality, such as DCR and cross-talk effects.

To evaluate the area of each peak, a multi-peak fit of the spectrum histogram had been performed, modelling each peak with a Gauss-Hermite function [43]:

$$\mathrm{GH} \;=\; N e^{-w^2/2} \left[1 + {}^3h H_3(w) \;+\; {}^4h H_4(w)\right], \tag{5.16}$$

where

$$w \;=\; \frac{x - \bar{x}}{\sigma}; \tag{5.17}$$

and N is a normalization factor, $\bar{x}$ is the peak position and σ is the variance of the gaussian function; $H_3(w)$ and $H_4(w)$ are the third and the fourth normalized hermite polynomials and their contribution gives the asymmetry of the peak shape, whose entity is regulated by the pre-factors ${}^3h$ and ${}^4h$, with values in the range $[-1, 1]$. The global fit function of the spectrum is a sum of as many Gauss-Hermite function as the number of resolved peaks.
The choice of the GH-function in Eq. (5.16) allowed to calculate the area A_n of the n-th peak in a very straightfoward way, simply by the relation

$$A_n \;=\; N_n \, \sigma_n \, (\sqrt{2\pi} \;+\; {}^4h_n). \tag{5.18}$$

The error σ_{A_n} on the obtained value had been calculated by propagating the errors on the fit parameters.
This analysis is also useful in order to calculate the system gain G: in fact, from the fitted values of the peak positions $\bar{x}_n$ it is immediate cakculating the peak-to-peak distance Δ for all the resolved peaks:

$$\Delta_{n,n+1} \;=\; \bar{x}_{n+1} \;-\; \bar{x}_n. \tag{5.19}$$

The error $\sigma_{\Delta_{n,n+1}}$ associated to this value can be once again obtained by propagating the fit errors of the peak position values; furthermore, to estimate G a weighted average on all the peak-to-peak values obtained from the analyzed histogram had been performed.

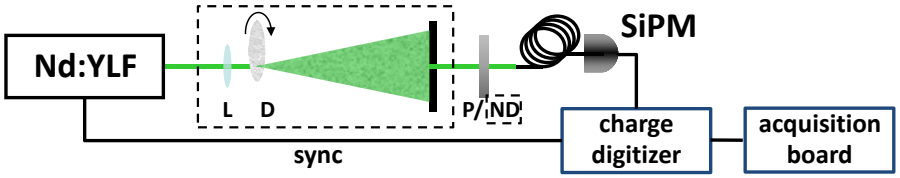

Figure 5.1: Experimental setup. Nd:YLF: laser source, P: polaroid, ND: variable neutral density filter, SiPM: detector. The components in the dashed boxes are inserted to produce the pseudo-thermal field.

As for the theoretical function, the effect of detection, DCR and amplification had been modelled as described in previous sections (see Eq.s (5.1)-(5.4) and Eq. (5.13)).
The effect of cross-talk had been described by using a bernoullian process, in a way analogue to what has been done with function $C_{k,m}(x_t)$ of Eq. (5.8). However, as cross-talk process is intrinsically a cascade phenomenon, its contribution has been calculated by adding higher order effects:

$$P_{k,cross} = \sum_{m=0}^{k} \sum_{n=0}^{m} \sum_{j=0}^{n} P_{k-m-n-j,det+dc}\, B_{m,k-m-n-j}(x_t)\, B_{n,m}(x_t)\, B_{j,n}(x_t); \tag{5.20}$$

where terms like $B_{j,n}(x_t)$ stand for the bernoullian distribution

$$B_{j,n}(x_t) = \left(\begin{array}{c} n \\ j \end{array} \right) x_t^j (1-x_t)^{n-j} \ . \tag{5.21}$$

Such a higher order expansion is not trivial to be achieved by the self-consistent approach of *Method I*, in which an explicit analytic expression of $P_{x,\mathrm{out}}$ is needed in order to calculate its momenta. Here, as all the elements of interest ($\overline{m}_{el}$, $\overline{m}_{dc}$, x_t, the number of modes μ) will be obtained as fit parameters, this is not necessary and therefore $P_{x,\mathrm{out}}$ can be just numerically calculated as the fitting function.
The major limit of this approach is obvious: as all the information on the statistics of the system is obtained from the peak areas, this method can only be applied to peak-resolving histograms with a number of peaks greater than the number of free parameters of the fitting function, which, in the present analysis, can rise up to five.

5.2 Experimental Setup

To test the aformentioned model, a stable light source emitting photons with rigorous poissonian statistics was needed, in order to avoid other sources of

deviation from the statistics; similarly, an overall control on the sources of noise of the SiPM under test were due.

- The sensor chosen for the experimental test was the Hamamatsu MPPC S10362-11-100C, whose main parameters are listed in Table 5.1, for many reasons:
  - first, its intrinsic high gain values would allow to acquire spectra without loss of information due to an excessively compressed scale and without and avoiding to add too many amplificators in the electronic chain;
  - its relatively low DCR values at room temperature contributed to an enhanced control on the sources of the deviation from the light statistics;
  - its low number of cells gave us much more control on the statistics of the Geiger-Müller avalanches;
- the sensor had been thus illuminated with a frequency-doubled Nd:YLF mode-locked laser amplified at 500 Hz (High Q Laser Production) that provides linearly polarized pulses of ∼5.4 ps duration at 523 nm wavelength;
- two series of measurements were performed, the first one directly on the coherent laser output with a poissonian statistics and the second one on the pseudo-thermal light obtained by passing the laser through a rotating ground-glass diffuser (D in Fig. 5.1) [44]; the light to be measured was delivered to the sensor by a multimode optical fiber (1 mm core diameter);
- the signal digitization was synchronized to the laser pulse and integration gate generated with an *AGILENT 33250A Waveform Generator*, externally triggered by the laser;
- signal was integrated by a *V171816ch QDC CAEN V792N*, with a 12-bit resolution over 400 pC range; the signal was typically integrated over a 200 ns long time window.

	Hamamatsu MPPC S10362-11-100C
Number of Diodes:	100
Area:	1 mm × 1 mm
Diode dimension:	100 μm × 100 μm
Breakdown Voltage:	**69.23** V
dark-count Rate:	**540** kHz at 70 V
Optical Cross-Talk:	**25** % at 70 V
Gain:	$3.3 \cdot 10^6$ at 70 V
PDE (green):	15 % at 70 V

Table 5.1: Main characteristics of the SiPM (Hamamatsu, model MPPC S10362-11-100C). The data refer to room temperature.

5.3 Experimental results

5.3.1 Coherent light

First of all, coherent light emerging from the laser had been measured. Values of the output, x, had been measured with 20000 subsequent laser shots for 15 series, each one with a different mean value $\overline{x}_{\rm out}$, set by rotating a polarizer (P in Fig. 5.1) in front of the collection fiber. Then a series in the absence of light had been acquired, whose mean value was used to set the zero.
Following *Method I* the experimental values of $F_{x,\rm out}$ and $S_{x,\rm out}$ could then be evaluated and results are plotted in Fig. 5.2 as a function of $\overline{x}_{\rm out}$. Fitting the data to straight lines the values obtained were (81.1 ± 0.2) ch, for $F_{x,\rm out}$, and (6971 ± 57) ch^2, for $S_{x,\rm out}$.
Using Equations 5.4 and 5.9 explicit expression for $P_{k,\rm cross}$ in case of impinging coherent light had been calculated:

$$P_{k,\rm cross} = e^{-\overline{m}_{\rm det+dc}}(1-x_t)^{-k}x_t^k \; {}_pF_q\left(1,-k;\frac{1}{2}-\frac{k}{2},1-\frac{m}{2};-\frac{(1-x_t)^2\overline{m}_{\rm det+dc}}{4x_t}\right)\frac{\sin(k\pi)}{k\pi}\,, \tag{5.22}$$

where $\overline{m}_{\rm det+dc} = \overline{k}_{\rm cross}/(1+x_t) = \overline{x}_{\rm out}/(G(1+x_t))$. Thus, the explicit expression of the first three momenta of the probability distribution had been calculated and inserted in Equations 5.14 and 5.15, obtaining:

$$F_{x,\rm out} = G\frac{1+3x_t}{1+x_t} \tag{5.23}$$

$$S_{x,\rm out} = G^2\frac{1+7x_t}{1+x_t} \tag{5.24}$$

at any mean value $\overline{x}_{\rm out}$. It is worth to note that in Equations 5.23 and 5.24 does not appear an explicit term representing the contribution of DCR.
These expressions had been used to evaluate G and x_t with a fit of the experimental values, obtaining $G = (75.4 \pm 1.3)$ ch and $x_t = (0.039 \pm 0.009)$. Then, x-values had been divided by G and re-binned in unitary bins [36, 42] to obtain

the $P_{k,\mathrm{cross}}$ distribution of the actual light signal amplitude measured in the presence of dark-counts and cross-talk. Note that due to the linearity of the detector the mean value of the output can be directly obtained as $\overline{k}_{\mathrm{cross}} = \overline{x}_{\mathrm{out}}/G$, independent of the shape of the distribution. In Fig. 5.3 had been plotted as

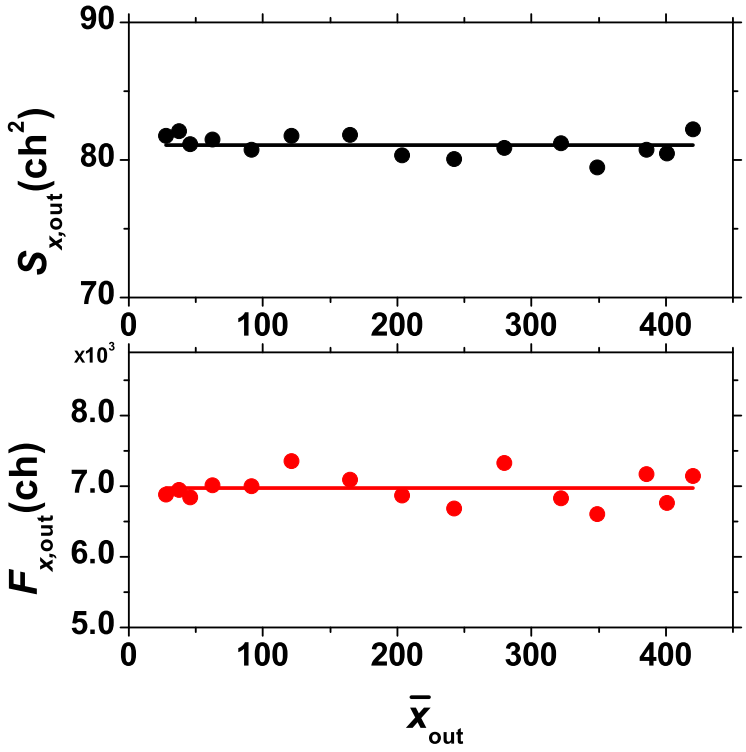

Figure 5.2: Plot of $F_{x,\mathrm{out}}$ and $S_{x,\mathrm{out}}$ as a function of $\overline{x}_{\mathrm{out}}$ for coherent light.

bars six different $P_{k,\mathrm{cross}}$ distributions at different mean values. Superimposed to the experimental values are shown two theoretical curves: one is a poissonian having mean value $\overline{k}_{\mathrm{cross}}$ (white circles), while the other (full circles) had been evaluated by including the cross-talk effect. The theoretical distributions (full circles in Fig. 5.3) had been evaluated by using the measured values of $\overline{x}_{\mathrm{out}}$, G and x_t. Note that measuring a coherent light with this method enables the simultaneous characterization of the detector gain and of the contribution of cross-talk. The comparison between the data and the theoretical functions can be estimated through the evaluation of the fidelity

$$f = \sum_{k=0}^{m} \sqrt{P_{k,\mathrm{exp}} P_{k,\mathrm{theo}}} \ . \tag{5.25}$$

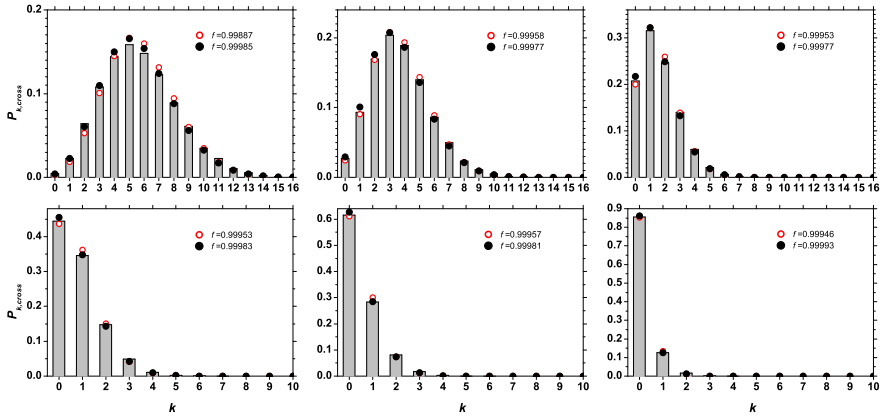

Figure 5.3: Experimental $P_{k,\mathrm{cross}}$ distributions at different mean values (bars) and theoretical curves evaluated according to *Method I*: poissonian (white circles), poissonian modified by cross-talk effect (full circles). The corresponding fidelity values of the reconstruction are also shown.

On the other hand, using the method of analysis of *Method II*, each one of the acquired histograms could be studied separately. As mentioned above, in the case of coherent light, the theoretical fitting function is described by a total of three free parameters: expectation value of light and DCR contribution $\overline{m}_{\mathrm{det+dc}}$, the probability x_t for an avalanche to trigger a second one and a global normalization factor (up to three "iterations"), so that analysis had been limited to spectra with at least 4 resolved peaks.
In Fig. 5.4 are shown the results of this analysis for the multi-peak fit and for the fit of the statistics of the avalanches using χ^2 as an indicator of the goodness of the fit result. The obtained x_t values are compatible with what we obtained with *Method I*. Also the gain values, evaluated as the peak-to-peak distance, show a good agreement with the G values given by *Method I*: $G = (78.28 \pm 0.26)$ ch for spectrum in left panel and $G = (72.61 \pm 0.19)$ ch for spectrum in right panel.

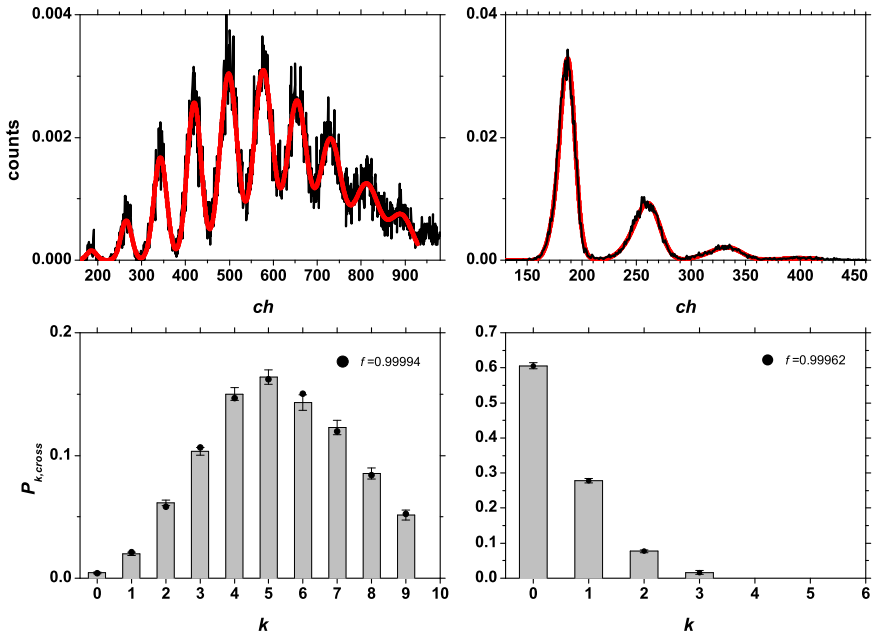

Figure 5.4: Experimental results for *Method II* applied on two of the histograms acquired with coherent light. Upper row: result of the multi-peak fit procedure; lower row: fitted theoretical distributions. The corresponding fidelity values of the reconstruction are also shown.

5.3.2 Multi-mode pseudo-thermal light

The photon-number distribution of a field made of μ independent thermal modes each containing N_{th}/μ mean photons [37] is given by

$$P_{n,\mathrm{ph}} = \frac{(n+\mu-1)!}{n!\,(\mu-1)!\,(N_{th}/\mu+1)^{\mu}\,(\mu/N_{th}+1)^{n}}\ , \tag{5.26}$$

for which $\overline{n} = N_{th}$, $\sigma_n^{(2)} = N_{th}\,(N_{th}/\mu+1)$ and $\sigma_n^{(3)} = N_{th}\,(N_{th}/\mu+1)\,(2N_{th}/\mu+1)$. In order to obtain information on the contribution of dark-counts was necessary to measure a different light statistics, whose shape is modified by the convolution with the poissonian distribution for dark-counts. A pseudo-thermal light field had been thus produced by selecting with a small aperture (~ 150 μm diameter) a region much smaller than the coherence area of the speckle patterns produced by the rotating diffuser.

The same procedure described for coherent light had been followed by measuring the values of the output, x, at 50000 subsequent laser shots and at 10

different mean values, obtained by means of a variable neutral-density filter (ND in Fig. 5.1). In Fig. 5.5 the plot of the experimental values of $F_{x,\mathrm{out}}$ and $S_{x,\mathrm{out}}$ is shown as a function of $\overline{x}_{\mathrm{out}}$, along with the fitting curves evaluated from Equations 5.14 and 5.15:

$$\begin{aligned} F_{x,\mathrm{out}} &= \left(1-\frac{\overline{x}_{\mathrm{dc}}}{\overline{x}_{\mathrm{out}}}\right)^2 \overline{x}_{\mathrm{out}} + B \\ S_{x,\mathrm{out}} &= A\left(1-\frac{\overline{x}_{\mathrm{dc}}}{\overline{x}_{\mathrm{out}}}\right)^3 \overline{x}_{\mathrm{out}}^2 + 3B\left(1-\frac{\overline{x}_{\mathrm{dc}}}{\overline{x}_{\mathrm{out}}}\right)^2 \overline{x}_{\mathrm{out}} + C \ , \end{aligned} \quad (5.27)$$

where μ, the number of indipendent thermal modes, had been setted equal to one and, for semplicity of notation the parameters $A = 2$, $B = G(1+3x_t)/(1+x_t)$ and $C = G^2(1+7x_t)/(1+x_t)$ had been introduced. Again, first of all the data had been fitted with $F_{x,\mathrm{out}}$ in this way obtaining the values of $\overline{x}_{\mathrm{dc}} = (5.82028 \pm 1.34015)$ and $B = (87.805 \pm 2.09009)$ ch.
Subsequentely the data for $S_{x,\mathrm{out}}$ had been fitted by substituting the obtained values of $\overline{x}_{\mathrm{dc}}$ ch and B to obtain $A = (2.34754 \pm 0.091576)$ and $C = (8531.48 \pm 419.571)$ ch^2. These values are then used to evaluate G and x_t, obtaining $G = (74.2785 \pm 1.76982)$ ch and $x_t = (0.100174 \pm 0.050529)$.

The x-values were then divided by G and re-binned in unitary bins [36] to obtain the $P_{k,\mathrm{cross}}$ distribution of the actual light signal amplitude measured in the presence of dark-counts and cross-talk. In Fig. 5.6 six different $P_{k,\mathrm{cross}}$ distributions are plotted at different mean values, depicted as bars. Superimposed to the experimental values two theoretical distributions are shown: the first one (white circles) is evaluated by including the contribution of dark-count that modifies the statistics of a single-mode thermal distribution (see Eq. (5.26)) into $P_{m,\mathrm{det+dc}}$ according to Eq. (5.28), which, in the present case, yields:

$$\begin{aligned} P_{m,\mathrm{det+dc}} &= \sum_{k=0}^{m} P_{k,\mathrm{dc}} P_{m-k,\mathrm{det}} \\ &= \frac{e^{-\overline{m}_{\mathrm{dc}}}}{(\mu-1)!}\left(1+\frac{\mu}{\overline{m}_{\mathrm{det}}}\right)^{-m}\left(1+\frac{\overline{m}_{\mathrm{det}}}{\mu}\right)^{-\mu} \\ &\quad U\left[-m, 1-m-\mu, \overline{m}_{\mathrm{dc}}\left(1+\frac{\mu}{\overline{m}_{\mathrm{det}}}\right)\right] \ , \end{aligned} \quad (5.28)$$

where $U(a,b,z)$ is the confluent hypergeometric function. The parameters are evaluated as $\overline{m}_{\mathrm{dc}} = \overline{x}_{\mathrm{dc}}/(G(1+x_t))$ and $\overline{m}_{\mathrm{det}} = (\overline{x}_{\mathrm{out}} - \overline{x}_{\mathrm{dc}})/(G(1+x_t))$. The second curve (full circles) is evaluated from Eq. (5.9) to take into account the cross-talk. Unfortunately, the calculation does not yield an easy analytical result, and hence it has been evaluated numerically.
The values of the fidelity for the data in Fig. 5.6 improve when both dark-counts and cross-talk are taken into account.

Turning now to the other approach, it is worth to notice how the number of fit parameters in this case is enhanced: the probability distribution is in this case

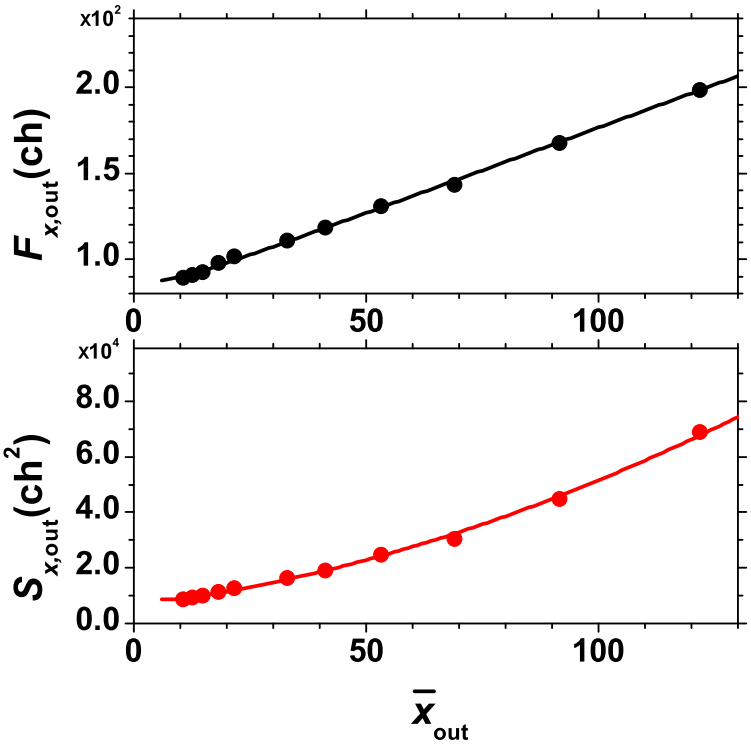

Figure 5.5: Plot of $F_{x,\mathrm{out}}$ and $S_{x,\mathrm{out}}$ as a function of $\overline{x}_{\mathrm{out}}$ for pseudo-thermal light.

described by the expectation value $\overline{m}_{\mathrm{det}}$ of avalanches generated by detection, the expectation value $\overline{m}_{\mathrm{dc}}$ of DCR contribution, the number of modes μ, the probability x_t of triggering a cross-talk event (up to three "iterations") and again a global normalization factor, for a total of 5 fit parameters: obviously, this puts a severe limit on the applicability of this method, needing at least 6 resolved peaks.

As it can be noted from the fit results in Fig. 5.7, once again the results obtained by using *Method II* are compatible within errors with what we found by applying *Method I*. However, whether the global fits present a very low χ^2 value for degree of freedom, the obtained fit parameters present high uncertainties, probably indicating the presence of very high off-diagonal elements in the minimization matrix and suggesting a strong correlation between the various parameters. This problem can be avoided by fixing some of the fit parameters (such as DCR or cross-talk), by retrieving their value from an accurate direct measurement.

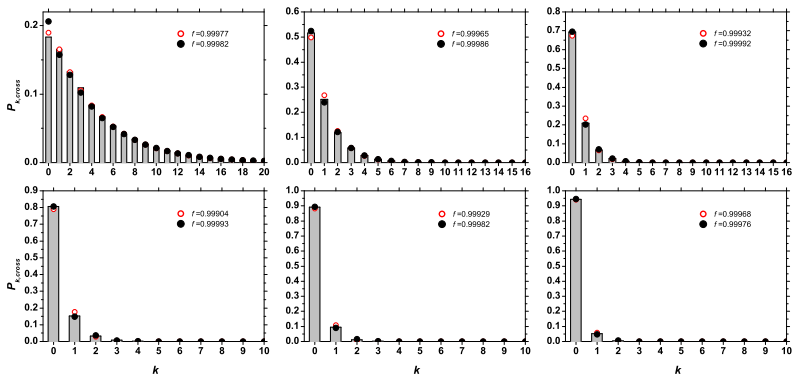

Figure 5.6: Experimental $P_{k,\mathrm{cross}}$ distributions at different mean values (bars) and theoretical distributions evaluated according to *Method I*: thermal modified by dark count distribution (white circles), thermal modified by dark counts and cross-talk effect (full circles). The corresponding fidelity values of the reconstruction are also shown.

5.4 Discussion

It is woth to compare the results of the two analysis methods on the same data sets. In Fig. 5.8 (a) as full circles are plotted the values of x_t obtained by applying *Method II* to coherent light along with their weighted average (full line). As a comparison, the value of x_t obtained by applying *Method I* is plotted as dashed line.
Similarly, in Fig. 5.8 (b) as full circles the values of mean photon numbers are shown, evaluated for the same data as in panel (a) by applying *Method II*. White circles represent the values of mean photon numbers obtained by applying *Method I*: the values are compatible within errors. The same comparison for the measurements on thermal light is shown in Fig. 5.9. Here it is possible to notice that the agreement is better for the mean values of detected photons (panel (a)) and for the DCR (panel (b)), while the estimated values of x_t from the two *Methods* definitely disagree. This can be due to the different approximations adopted by the two *Methods* (first order *vs* third order) that become relevant when measuring thermal light instead of coherent light.
In Table 5.2 we summarize the results of the two *Methods*. In conclusion, both *Methods* work in a self-consistent way, even if they have two definitely different approaches. *Method I* does not need peak resolving capability, but requires the acquisition of several histograms at varying η. Once determined the parameters x_t and DCR, all the datasets in a series can be analyzed, independent of the number of distinguishable peaks in the pulse-height spectrum. *Method II* works analyzing each histogram independently, but, as GM-avalanches distribution is obtained with a fit of the data, it requires at least a number of resolved peaks

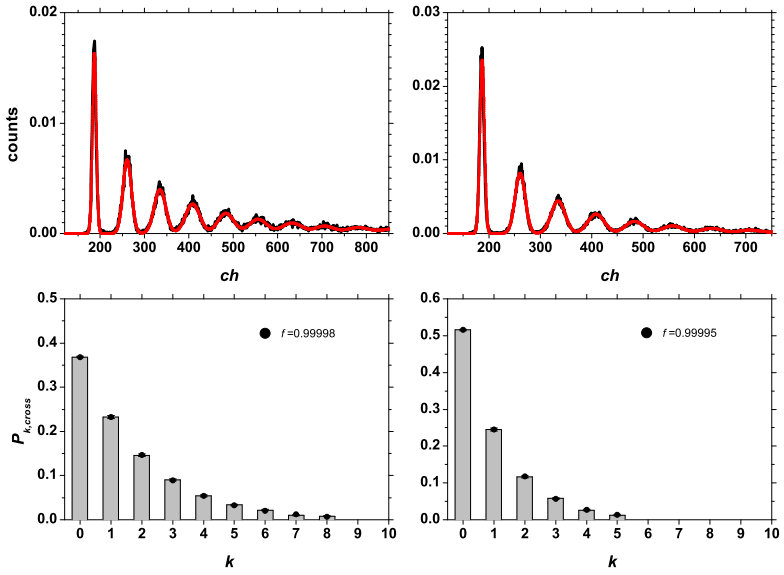

Figure 5.7: Experimental results for *Method II* applied on two of the histograms acquired with thermal light. Upper row: result of the multi-peak fit procedure; lower row: fitted theoretical function. The corresponding fidelity values of the reconstruction are also shown.

greater than the number of free parameters.
The fact that the two *Methods* give very similar results for mean photon numbers is particularly important as in most applications this is the only important parameter. Merging the two *Methods* we can devise an optimal strategy based on a self-consistent calibration performed by measuring a known light and analyzing the data with *Method I*: once known x_t and DCR, the determination of the mean photon number is independent of the specific statistics of light. Hence the information on the mean photon number can be obtained from each single measurement, even when the fitting procedure of *Method II* cannot be applied.

	Poissonian		Pseudo-thermal	
	Method I	*Method II*	*Method I*	*Method II*
DCR	-	-	0.071 ± 0.017	0.094 ± 0.035
Cross-talk	0.038 ± 0.008	0.027 ± 0.005	0.091 ± 0.042	0.035 ± 0.004

Table 5.2: Comparison between the global DCR and cross-talk values obtained with *Method I* and weighted average of the values obtained with *Method II*.

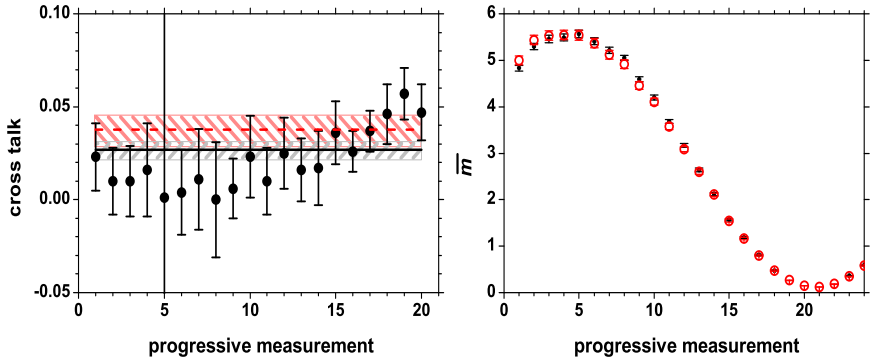

Figure 5.8: (a) Values of x_t obtained by applying *Method II* to coherent light (full circles) and their weighted average (full line). Dashed line: value of x_t obtained by *Method I*. (b) Values of mean photon numbers evaluated by applying *Method II* (full circles) and by applying *Method I* (white circles).

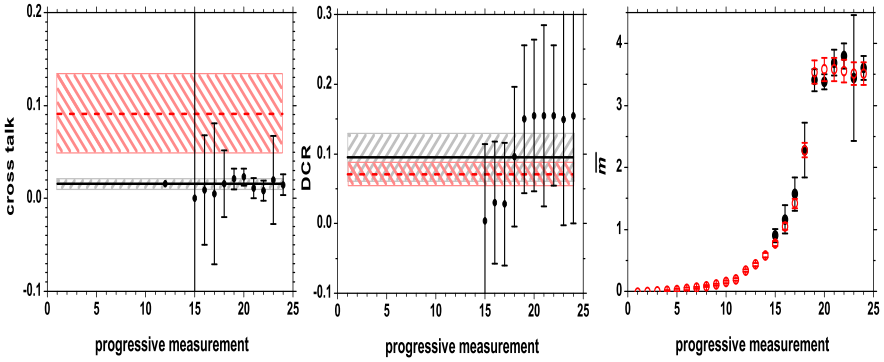

Figure 5.9: (a) Values of x_t obtained by applying *Method II* to thermal light (full circles) and their weighted average (full line). Dashed line: value of x_t obtained by *Method I*. (b) Values of DCR evaluated for the same data as in panel (a) by applying *Method II* (full circles) and their weighted average (full line). Dashed line: value of DCR obtained by *Method I*. (c) Values of mean photon numbers evaluated by applying *Method II* (full circles) and by applying *Method I* (white circles).

Chapter 6

Fluorescence Fluctuation Spectroscopy

Under the generic name of Fluorescence Fluctuation Spectroscopy (FFS) are grouped different tecniques principally applied to biophysics, with the objective of measuring parameters of interest (such as mean number of particle in the volume and/or their diffusion coefficient) of a system of particles (i.e. molecules) diffusing for brownian motion. These particles are ligated with fluorophore dyes, the sample is illuminated and consequent fluorescence emission is recorded and analyzed: brownian motion causes particles moving in and out of the *excitation volume* (i.e. the volume of the system illuminated in order to excite the fluorophores), thus causing variations in the intensity of the fluorescence light emission; from the measurement of fluctuations of fluorescence intensity, FFS techniques can determine the value of the parameters of the system under study.

If $\bar{N}$ is the average number of particles in the excitation volume, its variations can be, for a first qualitative analysis, estimated as of the order of $\sqrt{\bar{N}}$, while the mean intensity of the fluorescence can be with good approximation assumed as linearly proportional to $\bar{N}$: from this follows that the ratio between the fluctuations and the mean value of the fluorescence is $\sim 1/\sqrt{\bar{N}}$, decreasing with increasing average number of fluorescing particles. Thus, in order to optimize the experimental conditions, for a given concentration the excitation volume should be as small as possible; in order to archieve such an operational condition two principal methods of excitation of the fluorophores had been developed:

- a first method consists basically in focalizing the light meant to excite the fluorophore using a microscope; part of the fluorescence is collected again by the same microscope and is delivered in another microscope, which focalizes it on the sensor, after spatially filtering it with a pinhole on the focal plane: this *confocal setup*, with some more improvements, prevents from delivering out-of-focus fluorescence light;

- another method consists in the so called *two-photon excitation* (TPE): two photons of an energy lower than the energy gap between the gound state and the excited state can interact with electrons "simultaneously", thus bringing them to the excited level; being this a higher-order process, its cross section is very low and excitation can take place with a non-negligible probability only in the focus.

In the following sections the basics of these two methods will be illustrated in deeper detail. Subsequentely, the two main FFS techniques will be approached:

- *Fluorescence Correlation Spectroscopy* (FCS), based on the temporal autocorrelation of the fluorescence signal, allows to measure the mean number of particles in the excitation volume and the Einstein diffusion coefficient, thus characterizing the dynamical properties of the molecules under study;

- *Photon Counting Histogram* (PCH), performing fluorescence photon counting in a given sampling time, does not allow to measure the dynamical properties of the particles, but is meant to distinguish different particle species in the same sample, which is much more difficult with the FCS technique when they have the same dimension.

6.1 One and Two Photon Excitation

Stable light sources as lasers are natural candidates for FFS experiments [45, 46, 47], since any fluctuation in the intensity of the light source would obviously induce fluctuations in the fluorescence emission. Moreover, to restrict the system under study to a very small average number of molecules, mainly two setup schemes to minimize the excitation volume had been proposed and used since the early 1990s and will be described in the following.
The shape of the excitation volume is of paramount importance in analyzing FFS data, since it enters directely in the calculation of the physical expressions describing FCS and PCH output; thus different mathematical models of the laser beam intensity profile in the focus had been elaborated, in order to describe different experimental conditions [48]. A first model uses a three dimensional gaussian (3DG) profile:

$$I_{3DG}(x,y,z) \;=\; I_0 \exp\left(-\frac{2\left(x^2+y^2\right)}{\omega_0^2}-\frac{2z^2}{z_0^2}\right), \tag{6.1}$$

where z_0 and ω_0 are the beam waist respectively in the axial direction and in the other two directions.
A second model uses a Lorentzian function profile in the axial beam direction and a gaussian in the other two directions (2DGL):

$$I_{2DGL}(x,y,z) \;=\; I_0 \frac{2\omega_0^2}{\pi\omega^2(z)} \exp\left(-\frac{2(x^2+y^2)}{\omega^2(z)}\right), \tag{6.2}$$

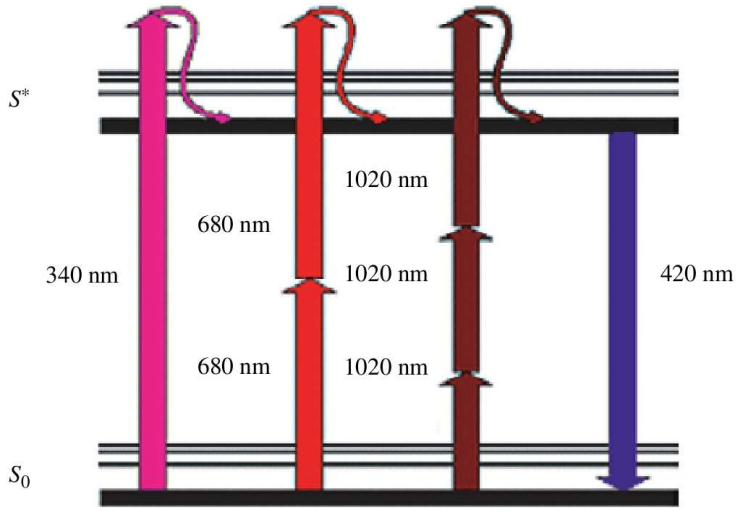

Figure 6.1: Pictografic representation (taken from [49] of the one, two and three photon fluorophore excitation process from the ground state S_0 to the excited level S^*.

where the Lorentzian shape along the z direction is given by

$$\omega^2(z) = \omega_0^2 \left(1 + \left(\frac{z}{z_R}\right)^2\right), \quad \text{with} \quad z_R = \frac{\pi\omega_0^2}{\lambda}, \tag{6.3}$$

for a beam of wavelenght λ.

It is often practical defining a scaled point spread function, as

$$\overline{PSF}\,(\vec{r},t) = \frac{I^n\,(\vec{r},t)}{I_0^n} \tag{6.4}$$

where the multiphoton index has values n =1 for one-photon excitation, $n = 2$ for two-photon excitation [48] and $\vec{r}$ indicates a three-dimensional vector. With this definition, the excitation volume becomes

$$V_{PSF} = \int \mathrm{d}\vec{r}\,\overline{PSF}\,(\vec{r},t)\,; \tag{6.5}$$

thus the mean number of particles respectively in the reference volume and in the excitation volume are merely linked together via the average concentration

$$\langle C\rangle = \frac{\bar{N}_0}{V_0} = \frac{\bar{N}_{PSF}}{V_{PSF}}. \tag{6.6}$$

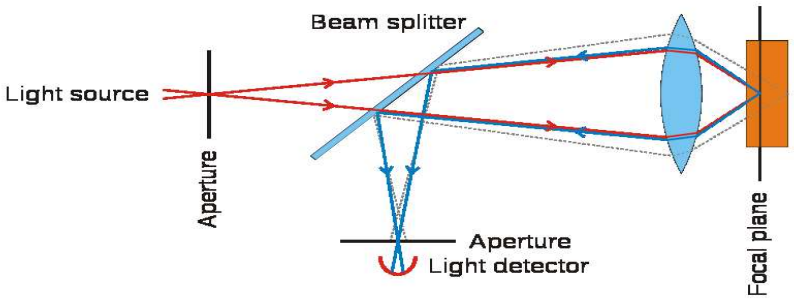

Figure 6.2: Schematic depiction of a confocal microscopy setup: source light is focalized in the biological sample, then fluorescence light is collected by the same microscope, deviated by a dicroic mirror and focalized on the detector, with a pinhole at the focal lenght.

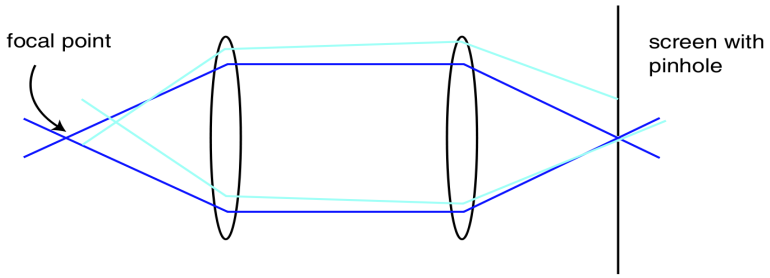

Figure 6.3: Functioning principle of the confocal microscope: out-of-focus light emission is prevented to reach the sensor by a pinhole placed on the focal plane.

6.1.1 Confocal Setup

The confocal setup was first realized in 1990 in an FCS experiment consists in the setup schematically depicted in Figure 6.2: it is used in FFS experiments in cas of one-photon excitation, to prevent fluorescence light emitted outside the point spred function to reach the detector.
A laser beam of the fluorophore excitation wavelenght is focalized onto the sample by a microscope of high numerical aperture [45]; fluorescence emission is collected again by the same microscope, deflected by a dichroic mirror and directed into another microscope, and light is finally delivered to the sensor; a micrometric pinhole is placed on the conjugate focal plane, or on the focal plane of the second microscope, to spatially filter fluorescence light: each component

needs to be fixed to three directional micropositioners, in order adjust the component position with a precision level of the micrometer.
As schematically depicted in Figure 6.3, this setup prevents most of the light emitted outside the focus from being delivered to the sensor, granting observation on a volume tipically of the order of 10 μm^3 [50]. However, as much of the light from sample fluorescence is blocked at the pinhole, this increased resolution is at the cost of decreased signal intensity so long exposures are often required.

6.1.2 Two-Photon Excitation

It had been theoretically predicted in the early 1930s [51] that electron transition to excited state can occur also with photons of half the necessary energy (thus with double wavelenght), but the use of this mechanism in biological application had been first proposed by Denk et al. in only 1990 [52]. As schematically depicted in Figure 6.1, if a photon of half the energy needed to excite the fluorophore is absorbed by an electron, this can reach a "virtual level": if then a second photon of the same wavelenght is absorbed (within a time $\sim 10^{-15}$ s), the electron reaches the ordinary excited state [45]. This kind of process requires photon flux of the order of 10^{31} photons/cm^{2}s, which can be tipically obtained only by focalizing light provided by mode-locked lasers with pulses of the order $\sim$ 0.1 - 1 ps, with a repetition rate of several tens of Megahertz.
A first advantage of TPE in FFS is thus clearly evident: since fluorophore excitation occurs only in the focus, a small excitation volume ($\sim$ 1 μm^3,see for exemple [48]) is automatically selected, without the need of an additional confocal setup to reject out of focus fluorescence.
A second advantage lies in the fact that the two-photon induced transitions due to the fact that is simmetry suppressed, is characterized by different selection rules and vibronic coupling[1]. Thus, two-photon excitation spectra can be considerably different from the one-photon excitation counterpart, which makes possible to accomplish simultaneous excitation of spectrally distinct dyes.

6.2 Fluorescence Correlation Spectroscopy

The basic principle of FCS is to measure the autocorrelation function $G(\tau)$ of the fluorescence intensity. If fluctuations of fluorescence intensity around its equilibrium value result principally from variation of particle number in the excitation volume due to brownian diffusion, the autocorrelation function will depend on the diffusion coefficient and on the size of the excited volume.
By definition, the non-normalized autocorrelation function is given by

$$G(\tau) \;=\; \langle F(t)F(t+\tau)\rangle\,, \tag{6.7}$$

[1]term describing transitions both vibrational and electronic, which in a molecule may be interrelated and can influence each other

where $F(t)$ is the fluorescence intensity at time t, and the angular brachets stand for time average. This expression can be rewritten as

$$G(\tau) \;=\; \langle \delta F(t) \delta F(t+\tau) \rangle + \langle F \rangle^2 \,, \tag{6.8}$$

where the fluctuations of fluorescence intensity can be expressed as

$$\delta F(t) \;=\; F(t) - \langle F \rangle \;=\; \beta \int \mathrm{d}V \, I^n \left(\vec{r}, t \right) \delta C \left(\vec{r}, t \right) , \tag{6.9}$$

where β is a factor including the absorption cross-section, fluorescence quantum yield and light collection efficiency. The previous equation is based on the *assumption that excitation light intensity is constant* and thus fluorescence fluctuations are almost entirely due to particle concentration fluctuations in the excitation volume

$$\delta C \left(\vec{r}, t \right) \;=\; C \left(\vec{r}, t \right) - \langle C \rangle \,. \tag{6.10}$$

Using Equations 6.4 and 6.5 in Equation 6.9 leads to

$$\langle F \rangle \;=\; \beta I_0^n V_{PSF} \langle C \rangle \,, \tag{6.11}$$

representing the flat backgound in the autocorrelation function in Equation 6.8: evaluation of the $\langle \delta F(t) \delta F(t+\tau) \rangle$ term is much more complicated.
Assuming that the concentration variation $\delta C((\vec{r}, t)$ follows the diffusion equation

$$\frac{\partial \delta C \left(\vec{r}, t \right)}{\partial t} \;=\; D \nabla^2 \delta C \left(\vec{r}, t \right) , \tag{6.12}$$

it has been demonstrated (see [53]), that

$$\left\langle \delta C \left(\vec{r}, t \right) \delta C \left(\vec{r'}, t+\tau \right) \right\rangle = \frac{\langle C \rangle}{\left(4\pi D \tau \right)^{3/2}} \exp \left(- \frac{\left| \vec{r} - \vec{r'} \right|^2}{4 D \tau} \right) , \tag{6.13}$$

where D is the Einstein diffusion coefficient, which, for particles of radius R, in a solution of viscosity η at temperature T has the following expression:

$$D \;=\; \frac{k_B T}{6 \pi \eta R} . \tag{6.14}$$

In case of one photon excitation and 3DG beam profile, insertion of Equation 6.13 into Equation 6.8 normalized respect to $\langle F \rangle^2$, leads to:

$$G(\tau) \;=\; 1 + \frac{1}{V_{PSF} \langle C \rangle} \left(1 + \frac{\tau}{\tau_D} \right)^{-1} \left(1 + \frac{(x_0^2 + y_0^2)\tau}{z_0^2 \tau_D} \right)^{-1/2} ; \tag{6.15}$$

where $\tau_D = (x_0^2 + y_0^2)/4D$ (see [45]) and for $\tau \to 0$, the mean number of particles in excitation volume $\bar{N}_{PSF} = V_{PSF} \langle C \rangle$ can be obtained.
This model can be further improved, adding for exemple active particle transport [54] .
It has been demonstrated that for TPE the double integral expressing the autocorrelation function has no explicit analytic solution; however, different parametrizations, similar to Equation 6.15 can be used in order to analyze data ([53]and [49]).

6.3 Photon Counting Histogram

6.3.1 Basic principles: the Mandel Equation

The bases of the PCH technique lies in the description of the photodetection. It had been shown that for many purposes, a semiclassical treatment where the electromagnetic field is described classically and the atomic system of the detector is treated quantum mechanically, is a proper description of the photodetection process [55]. Thus, the photon counting statistics is well described by the Mandel formula

$$p\left(k,t,T\right) \;=\; \int_0^\infty \frac{\left(\eta W(t)\right)^k \mathrm{e}^{-\eta W(t)}}{k!} p\left(W(t)\right) \mathrm{d}W(t), \tag{6.16}$$

describing the probability of detecting k photons at time t, with a detector integration time T and a detection efficiency η. The probability distribution of the energy of the electromagnetic field on the detector is given by

$$W(t) \;=\; \int_t^{t+T} \mathrm{d}t \int_A \mathrm{d}A\, I(\vec{r},t), \tag{6.17}$$

that is the integration of light intensity $I(\vec{r},t)$ over the integration time T and the detector area A and thus $p(W(t))$ is the energy distibution.
From Equation 6.16, it emerges that the detection is characterized by two fundamental forms of randomness; the first one, known as *shot noise*, reflects the quantum mechanical nature of the photodetection process, in its discreteness and statistical indipendence. As a matter of fact, even in the ideal case of detection of a source with constant intensity, such that $p(W(t)) = \delta(W - \bar{W})$, the photon counting distribution is given by a Poisson distribution.
The second source of noise is given by the variations in the intensity of the detected electromagnetic field, expressed by the energy distribution $p(W)$. Any fluctuation of the light intensity will cause a deviation of the distribution of the detected photons from a Poisson distribution to a super-Poissonian distribution: while for a Poisson distribution the variance σ^2 is equal to the mean value $\langle k \rangle$, for a super-Poissonian we have that $\sigma^2 > \langle k \rangle$. The reason of this characteristic "additional broadening" of the distribution is immediately clear by interpreting Equation 6.16 as a superposition of Poisson distributions for different energy values W, each one weighted by a factor $p(W)$.
A key role is played by the integration time: for $T \to \infty$, the intensity fluctuations will be completely averaged, thus the energy distribution function will approach a Dirac δ-function and consequentely the photon count distribution will become a Poissonian distribution. So in order to track the intensity fluctuations, the integration time has to approach zero, or at least to be chosen shorter than the particle fluctuations time scale: in these operational conditions, a proportionality between the energy distribution and the intensity distribution can be assumed, so that $p(W) = p(I)T$ and Equation 6.16 can be rewritten as

$$p(k) \;=\; \int_0^\infty \mathrm{d}I_D\, Poi\left(k, \eta_I I_D\right) p(I_D), \tag{6.18}$$

where $Poi\,(k, \eta_I I_D)$ is a Poisson probability distribution of counting k photons, with an expectation value of $\eta_I I_D$, being I_D the light intensity at the detector and $\eta_I = T\eta$. Using Equation 6.4, the intensity of light reaching the detector at position $\vec{r}_0$ is given by

$$I_D \;=\; I_0^n \beta \overline{PSF}(\vec{r}_0), \tag{6.19}$$

where the parameter β again contains excitation probability, fluorescence quantum yield and all the setup and instrument dependent factors.

6.3.2 Photon Counting for one particle in a closed system

Moving from these basic principles, it is possible to model the photon counting histogram for fluorescence fluctuations. Using Equation 6.19 a relation between the intensity at the detector and the position of a fluorescent particle can be expressed as

$$p(I_D) \;=\; \int \mathrm{d}\vec{r}\, \delta\left(I_D - I_0^n \beta \overline{PSF}(\vec{r})\right) p(\vec{r}). \tag{6.20}$$

Starting from the ideal case of a single particle moving freely in an enclosed reference volume V_0, the particle position probability distribution will be described by the following:

$$p(\vec{r}) \;=\; \begin{cases} 1/V_0 & \text{for } \vec{r} \in V_0, \\ 0 & \text{for } \vec{r} \notin V_0. \end{cases} \tag{6.21}$$

Combining Equation 6.21 with Equation 6.18, the probability of measuring k photons, from one particle in a reference volume V_0 with *molecular brightness* $\epsilon = I_0^n \beta \eta_I$, is obtained as:

$$\begin{aligned} p^{(1)}(k; V_0, \epsilon) \;&=\; \int \mathrm{d}\vec{r}\, Poi\left(k, \epsilon \overline{PSF}(\vec{r})\right) p(\vec{r}) \\ &=\; \frac{1}{V_0} \int \mathrm{d}\vec{r}\, Poi\left(k, \epsilon \overline{PSF}(\vec{r})\right), \end{aligned} \tag{6.22}$$

which describes a super position of Poissonian distribution each with expectation value $\epsilon \overline{PSF}(\vec{r})$. Thus, from Equation 6.22, the average number $\langle k \rangle$ of photon counts for one molecule freely diffusing in the volume V_0 is given by

$$\langle k \rangle = \frac{\epsilon}{V_0} \int \mathrm{d}\vec{r}\, \overline{PSF}(\vec{r}) \;=\; \epsilon \frac{V_{PSF}}{V_0}. \tag{6.23}$$

The molecular brightness ϵ indicates the number of counts per molecule per sampling time. A second time indipendent parameter can be introduced, as $\epsilon_{sec} = \epsilon / T = I_0^n \beta \eta$, expressing the photon counts per molecule per second.

Under the assumption that no fluorescence photons can be generated outside the point spread function volume, explicit expressions for $p^{(1)}(k; V_0, \epsilon)$ had been calculated in [48], for 2DGL and 3DG point spread functions. As the integral

of Equation 6.22 diverges for k=0, the expressions are valid for $k > 0$ and $p^{(1)}(0; V_0, \epsilon)$ are calculated from the normalization condition of the probability distribution functions. Thus, for exemple, in case of two-photon excitation with a 2DGL beam profile with $V_{PSF} = \pi\omega_0^4/\lambda$, one obtains

$$p^{(1)}(k; V_0, \epsilon) \;=\; \frac{1}{V_0}\frac{\pi^2\omega_0^4}{2\lambda k!}\int_0^\infty \mathrm{d}x\,(1+x^2)\gamma\left(k, \frac{4\epsilon}{\pi^2(1+x^2)^2}\right), \tag{6.24}$$

or, in case of one-photon excitation with a 3DG profile with $V_{PSF} = (\pi/2)^{3/2}\omega_0^2 z_0$, the probability distribution becomes

$$p^{(1)}(k; V_0, \epsilon) \;=\; \frac{1}{V_0}\frac{\pi\omega_0^2 z_0}{k!}\int_0^\infty \mathrm{d}x\,\gamma\left(k, \epsilon\mathrm{e}^{-2x^2}\right). \tag{6.25}$$

6.3.3 PCH in an open system

The generalization to an expression for N non-interacting particles is straightforward: if these particles can be treated as statistically indipendent variables, the probability of measuring k photons, from N particles with molecular brillance ϵ, freely diffusing in a volume $V_0 > V_{PSF}$ is given by N-times the convolution of the probability distribution for a single particle, or, in formula

$$p^{(N)}(k; V_0, \epsilon) \;=\; \underbrace{p^{(1)} \otimes \cdots \otimes p^{(1)}}_{N \text{ times}}(k; V_0, \epsilon) \tag{6.26}$$

In real experimental conditions the reference volume V_0 is not closed, so that the number of particles inside it is not fixed; if V_0 is chosen so that it is much smaller than the resevoir, the particle number fluctuations are well described by Poisson statistics

$$p(N) \;=\; Poi(N, \bar{N}_0), \tag{6.27}$$

where $P(N, \bar{N}_0)$ is a Poisson distribution with expectation value $\bar{N}_0$, the average number of particle in the reference volume, which is linked to the average number of particles in the excitation volume $\bar{N}_{PSF}$ according to Equation 6.6.
If the system under analysis is open, the probability of having no particles in the reference volume must be taken into account: with no particles inside V_0 and therefore inside V_{PSF} there must be no photon counts by definition, so this probability can be expressed as

$$p^{(0)}(k; V_0, \epsilon) \;=\; \delta(k), \quad \text{where} \quad \delta(k) \;=\; \begin{cases} 1 & \text{for } k = 0 \\ 0 & \text{for } k > 0 \end{cases} \tag{6.28}$$

Under these conditions, the PCH for an open system is obtained by averaging the single probabilities of counting k photons with N particles, each one weighted by the corresponding poissonian probability of having N particles in the reference volume:

$$\Pi(k; \bar{N}_{PSF}, \epsilon) \;=\; \sum_{N=0}^{\infty} p^{(N)}(k; V_0, \epsilon)\, Poi(N, \frac{V_0}{V_{PSF}}\bar{N}_{PSF}). \tag{6.29}$$

From this expression, the average number of photon counts can be directely extimated and corresponds to

$$\langle k \rangle \; = \; \epsilon \bar{N}_{PSF}. \tag{6.30}$$

On the other side, it has been proven (see [48]) that the deviation from the poissonian behaviour is also proportional to the molecular brilliance

$$\mathcal{Q} \; = \; \frac{\sigma^2 - \langle k \rangle}{\langle k \rangle} \; = \; \gamma_2 \epsilon, \tag{6.31}$$

where $\mathcal{Q}$ is the Mandel deviation factor [56], that is the Fano factor of the measured photon-counts distribution minus one (as the Fano factor of a Poissonian distribution has a value of exactely of one, so that $\mathcal{Q} = 0$), while γ_2 is the so called *geometrical factor*, defined as

$$\gamma_m \; = \; \frac{\int \mathrm{d}\vec{r} \, \overline{PSF}^m(\vec{r})}{\int \mathrm{d}\vec{r} \, \overline{PSF}(\vec{r})}, \tag{6.32}$$

which in Equation 6.31 is calculated for $m = 2$.
These results lead to two principal methods of analyzing data from a PCH measurement:

- by direct analysis of the photon counting histogram, providing an expression for Equation 6.29, and using it to fit the normalized histogram of the photon counts, obtaining $\bar{N}_{PSF}$ and ϵ as fitting parameters;

- by analysis of the momenta since, as shown in Equations 6.30 and 6.31, $\bar{N}_{PSF}$ and ϵ are related to the first and the second momenta of the normalized counts distribution.

Further improvements of the previously depicted model have been elaborated, during the past few years.
Most noticeably, deviations from ideality of the detectors, in particular the effect of dead time τ_d of the instrumentation, had been taken into account in [57]. Introducing a parameter $\delta = \tau_d / T$, where T is the integration time, Equation 6.30 becomes (parameters labelled with a prime indicate modifications due to dead time contribution):

$$\langle k \rangle' \; = \; \epsilon \bar{N}_{PSF} \left[1 - \delta \epsilon (\gamma_2 + \bar{N}_{PSF}) \right], \tag{6.33}$$

while the Mandel deviation factor is affected by dead time according to the following

$$\frac{\mathcal{Q}' - \mathcal{Q}}{\mathcal{Q}} \approx \delta \left[-\frac{2\bar{N}_{PSF}}{\gamma_2} - 2 - 3\epsilon \bar{N}_{PSF} + \epsilon \left(\gamma_2 - \frac{2\gamma_3}{\gamma_2} \right) \right], \tag{6.34}$$

for small values of δ. In an analogue way, the authors calculated deviations due to the afterpulsing probability p_a (starred quantities):

$$\langle k \rangle^* = \langle k \rangle + p_a \langle k \rangle \tag{6.35}$$

$$\frac{\mathcal{Q}^* - \mathcal{Q}}{\mathcal{Q}} \approx p_a \left(1 + \frac{2}{\gamma_2 \epsilon}\right). \tag{6.36}$$

Another improvement worth to be mentioned is the introduction of the *out-of-focus correction* in one-photon excitation PCH, by Huang et al. [58]: the same authors had previously demonstrated in [59] that in one-photon excitation the use of a simple 3DG profile could lead to significant errors in data analysis.
The hypotesis was that in one-photon excitation, out of focus fluorescence emission could be collected and detected, in case the observation volume is larger than the point spread function volume. Defining for compactness

$$\omega_m = \int \mathrm{d}\vec{r} \overline{PSF}^m(\vec{r}), \tag{6.37}$$

a parameter representing the deviation of the actual observation volume profile from the 3DG profile had been defined as

$$\mathrm{F}_m = \frac{\omega_m - \omega_{3DG\,m}}{\omega_{3DG\,m}}. \tag{6.38}$$

Then, noting that $\omega_1 = V_{PSF}$, an *observational volume* V had been defined as

$$V = \frac{\omega_1^2}{\omega_2} = \frac{(1 + \mathrm{F}_1)^2}{1 + F_2} \frac{\omega_{3DG\,1}^2}{\omega_{3DG\,2}}. \tag{6.39}$$

Corrections for out-of-focus emission are obtained by introducing the parameter $Q = V_0/V$ and expanding in Tayolr series Equations 6.22: the order of corretion m_c is chosen by setting $\mathrm{F}_m \approx 0$ for $m > m_c$.

6.3.4 Multiple Species

If two different species non interacting with each other are present in the same sample with a number of molecules N_1 and N_2, respectively, and had been ligated with different fluorophores displaying different molecular brightness ϵ_1 and ϵ_2, the PCH for this system is straightforwardly given by the convolution of the PCH for the single specie:

$$\Pi(k; \bar{N}_1, \bar{N}_2, \epsilon_1, \epsilon_2) = \Pi(k; \bar{N}_1, \epsilon_1) \otimes \Pi(k; \bar{N}_2, \epsilon_2). \tag{6.40}$$

This makes PCH more suitable than FCS for the identification of multiple species in the same sample: indeed in case of FCS analysis, different particles need to possess significantly different kinetic properties in order to be distinguished; using PCH technique, instead, if the species mantain the hypothesis of no mutual interaction, it is enough to use appreciably different fluorophores in order to distinguish them and measure the average number of particles.

Chapter 7

Photon Counting Histogram with SiPMs

In the following chapter, several issues related to a series faseability studies regarding the use of SiPMs as detecting technology in PCH experiments are presented.
In particular, it is by this point self evident that the standard PCH model presented in Chapter 6 is not suitable for properly analyze SiPM output; thus the phenomenological model for SiPM response presented in Chapter 5 had been used to modify the PCH equations, taking into account deviations from ideal detection caused by the presence of optical cross-talk and DCR.
In parallel, setup commissioning had been carried on using SPADs as refrence detectors and main problems and goals are presented; finally, tests with SiPMs had been performed and analyzed.

7.1 Why SiPMs in PCH?

So far, PCH measurements have been performed using APDs or other fast single-photon counting detectors; these detectors are suited for use in the single-photon regime, that is keeping the intensity of the impinging light very low in order to reduce the probability of photon arrival during the sensor dead time (tipically of the order of 80 ns for SPADs): consequently, since the resulting count rate is low too, the sampling time must be chosen not too small, tipically ranging from few tens of microseconds up to milliseconds. This obviously sets an lower limit on the timescale of the process under study.

On the other hand, it has been extensively demonstrated in previous chapters that SiPMs are fast enough sensors ($\tau_{fall} \sim 30$ ns), with high photon number resolving capability and strict linearity; moreover, if the impinging light flux does not cause the detector saturation and can be assumed as homogeneously distributed on the sensor area, SiPMs have virtually no dead time, since under

these conditions there are always cells available which are ready for detection. These features suggested two principal improvements for PCH experiments.

First, as with the use of SiPMs single-photon regime could in principle be avoided, there could be a reduction of sampling time T to the order of 100 ns, which could allow the use of PCH technique for investigation of processes which were previously below the system resolution capabilities.
Second, shortening integration time could allow performing both PCH and FCS measurement with the same data acquisition. In fact, in practical FCS experimental conditions, fluorescence intensity is acquired for sampling times T short enough to grant temporal resolution, and a dedicated autocorrelator records the measured intensity for each time interval, so that Equation 6.7 becomes

$$G(\tau) \; = \; \sum_{j} F(j \times T) F(j \times T + \tau). \tag{7.1}$$

If T is also adequately long as to provide a measurement of the number of detected photons, the same data output can be used to construct a PCH.

7.2 PCH modification: Cross-Talk and DCR

The expression for PCH distribution 6.29 obtained in Chapter 6 had been calculated assuming an ideal detection process. However, as extensively demonstrated in previous Chapters, SiPM detection process presents relevant deviations from ideality which have to be taken into account in order to properly analyze their output.

The procedure described in Chapter 5 can be applied to PCH probability distribution $\Pi(k; \bar{N}, \epsilon)$ described in Equation 6.29. Using Equation 5.4, PCH can be first convoluted with a poissonian distribution $P_n(\langle n \rangle_{dcr})$ with expectation value $\langle n \rangle_{dcr} = \nu_{dcr} T$, the average DCR value ν_{dcr} multiplied by the integration time T; Equation 5.9 can be applied to the resulting distribution, thus obtaining

$$\begin{aligned} &\Pi^{\star}\left(k; \bar{N}, \epsilon, x_t, \langle n \rangle_{dcr}\right) = \\ &= \sum_{N=0}^{\infty} p_{\#}(N; \bar{N}) \sum_{m=0}^{k} C_{k,m}(x_t) \sum_{n=0}^{\infty} P_n(\langle n \rangle_{dcr}) p^{(N)}(m-n; \epsilon), \end{aligned} \tag{7.2}$$

where x_t is the parameter representing the probability for a cell of triggering a neighbour cell by cross-talk and $C_{k,m}(x_t)$ is the bernoullian-like distribution defined in section 5.1 describing the probability of measuring k G-M avalanches out of n previously triggered, with $k > m$.
As shown in paragraph 5.1, this procedure leads to probability distribution functions with an explicit analytic expression and whose first three momenta can be explicitly calculated; using Equation 5.10 and 5.11, the modified (signed

by a star $\star$) expressions for the average photon count number and the Mandel deviation factor are obtained:

$$\langle k \rangle^{\star} = (1 + x_t) \left(\epsilon \bar{N} + \langle n \rangle_{dcr} \right) \tag{7.3}$$

$$\mathcal{Q}^{\star} = \frac{(1 + x_t)^2 \gamma \epsilon^2 \bar{N} + 2x_t \left(\epsilon \bar{N} + \langle n \rangle_{dcr} \right)}{(1 + x_t) \left(\epsilon \bar{N} + \langle n \rangle_{dcr} \right)}, \tag{7.4}$$

where γ stands for the geometrical factor of Equation 6.32 calculated for $m = 2$, and the superscript "2" had been dropped for the sake of simplicty.

Thus, in principle, Equation 7.2 can be used to to fit the experimental PCH results and consequentely obtain the values for $\bar{N}$ and ϵ as fit parameters.
On the other hand, explicit calculation of the momenta of the photon count distribution function corrected for cross-talk and DCR contribution, could allow to calculate the parameters of interest by simultaneously solving Equations 7.3 and 7.4, provided that three of the five parameters present are previously measured and then set as fixed.

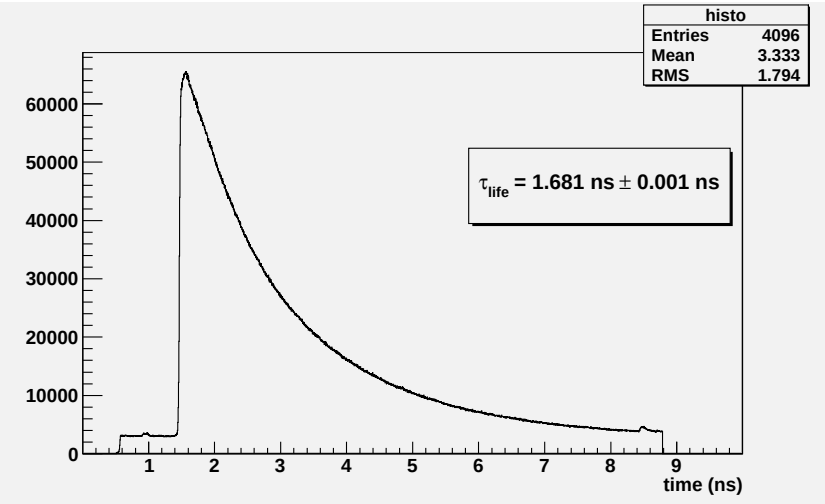

Figure 7.1: Lifetime measurement of rhodamine B in water: the characteristic time has been obtained by a fit with an exponential function.

7.3 Experimental Setup

In order to experimentally verify the capabilities of SiPMs in PCH experiments a simple Two-Photon setup had been assembled:

- light has been provided using a Ti:Sapphire mode-locked laser[1], with 48 MHz of repetition rate and 3.9 ps of pulse width; 840 nm fundamental harmonic had been extracted from the cavity with a prism and delivered to the focusing objective;

- infrared light has been focused in the sample using a Nikon Plan objective with 1.25 numerical aperture, infinity corrected and to be operated at a working distance of 0.17 mm; to avoid excessive refractive index mismatch, the space between the objective lens and the cuvette containig the fluorescent solution had been filled with optical grease;

- a solution of rhodamine B in water, with excitation wavelegth around 610 nm has been used as fluorescence source: in Figure 7.1 a lifetime measurement of the fluorophore is shown, with a lifetime $\tau_{life} = 1.68$ ns;

- fluorescence has been collected by the same objective, deviated using a dichroic mirror and delivered to the SiPM via multimode 1 mm diameter fiber;

[1] Tiger-ps SHG, Time Bandwidth Products, Zurich, CH

- a SiPM by Hamamtsu (MPPC S10362-11-100C) has been used, controlled by a CAEN SP5600 General Purpose Power Supply and Amplification Unit module with an integrated threshold discriminator[2]: digital NIM output of the discriminator has been set in coincidence with the laser synchronized signal using a EG&G CO4010 module;
- coincidence frequency has been measured with a CAEN VME V1718 module.

7.4 Data Acquisition

Given the 48 MHz repetition rate of the laser light source, the SiPM is espected to detect a pulse of fluorescence light every 20 ns and with a recovery time of $\sim$ 60 ns, output signal will pileup.
In these experimental conditions, the usual charge measurement seemed unfeasible:

- the CAEN V792N QDC requires an integration gate starting at least 15 ns before the rise of the signal, meaning that the board would not be able to process every pulse; moreover, due to the pileup, the output of a charge measurement performed by signal integration would lead to a result difficult to interpret in order to reconstruct the photn statistics;
- the DT5720A Desktop Digitizer[3] samples the output signal every 4 ns, which means that the signal integration would be performed using only 5 points.

Thus a completely different approach in data acquisition had been carried on, in order to measure the modified PCH distribution of Equation 7.2; the coincidence frequency $\nu(x)$ between a threshold scan of the SiPM output and a trigger signal ν_T synchronous with the laser pulses (but with a reduced frequency) has been acquired; the measured frequency can be described by the following relation:

$$\nu(x) \;=\; \nu_T \left(1 - \mathrm{e}^{-t_C \nu_S \int_x^{+\infty} \mathrm{d}yP(y)}\right) \;+\; \nu_T t_C \nu_S \int_x^{+\infty} \mathrm{d}yP(y); \tag{7.5}$$

where x is the threshold value, ν_S is the laser repetition rate and t_C is the coincidence time window. The above Equation is based on the fact that coincidence happens both if after a trigger signal at least a SiPM signal over threshold x is triggered within the concidence time window *or* if trigger signal rises within the coincidence time after SiPM signal passes the threshold. For small Poissonian expectation values, Equation 7.5 can be approximated as:

$$\nu(x) \;\approx\; 2\nu_T \nu_S t_C \int_x^{+\infty} \mathrm{d}y\, P(y); \tag{7.6}$$

[2]a description of the module can be found on the datasheet available on the website: http://www.caen.it/
[3]technical informations about all the above mentioned CAEN devices are availabe at http://www.caen.it/

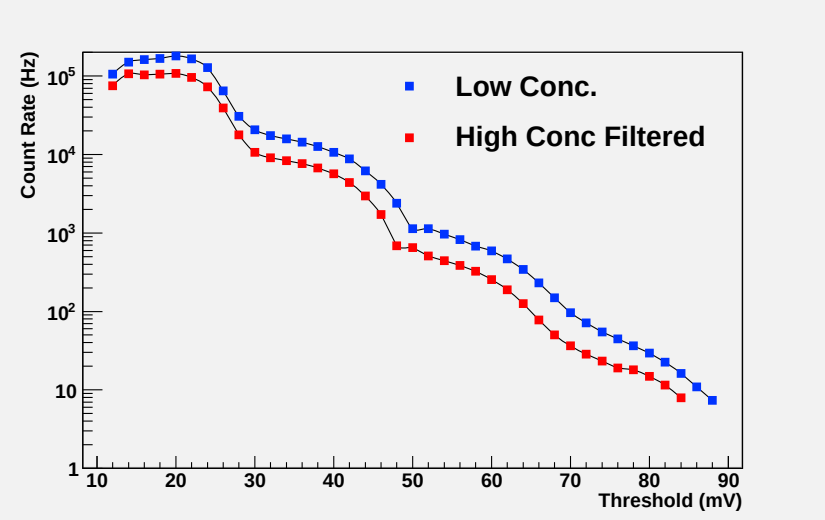

Figure 7.2: Threshold scan of the fluorescence signal for the 200 nM concentrated solution (blue squares) and for the 2 μM concentrated solution (red squares). A slight deviation in the lenght of the last "steps" can be noticed, meaning that probably there had been some relevant variation of the over bias.

thus, by Fundamental Theorem of Integration the distribution can be obtained as

$$P(x) \;=\; \frac{-1}{2\nu_T \nu_S t_C}\,\frac{\mathrm{d}\nu}{\mathrm{d}x}(x); \tag{7.7}$$

subsequentely, performing multipeak integration of the obtained $P^\star$ with a similar procedure described in Chapter 5, the counting histogram is obtained.
It is worth to stress that the correct identification of the normalizing constant is of utmost importance in this procedure, also beacuse the $\Pi^\star(0)$ entry of the counting histogram is obtained from the request of normalization of the PCH:

$$\Pi^\star(0) \;=\; 1 - \sum_{k=1}^{L} \Pi^\star(k) \tag{7.8}$$

where L is the last detected peak.

7.5 Experimental Results

Before starting with the fluorescence measurements, two preliminary data acquisition have been performed:

- an ordinary DCR staircase had been acquired, necessary to obtain a cross-talk probability measurement;

- a coincidence measurement of the dark counts, in order to extimate the $\langle n \rangle_{dcr}$ parameter.

Then, a solution of rhodamine B in water with a concentarion of 2 μM has been prepared: part of this solution has been diluted 10 times, to reach a 200 nM concentration of fluorophores. This second sample has been placed in a cuvette with micrometric thick bottom and placed on the microscope: fluorescence emission has been analyzed with the threshold scan method described in the previous section.
The 2 μM concetrated solution had been subject to the same procedure, but a neutral filter of 1 optical density[4] had been placed in front of the fiber, to reduce the fluorescence intensity to have approximately the same mean value of photon counts of the less concentrated solution, to make the comparison between the two distribution easier: for equal mean value, the 200 nM concentrated solution PCH should possess greater deviations from poissonian behaviour compared with the more concentrated one, therefore showing an higher tail of the distribution and an higher Fano factor.
In Figure 7.2 the resulting staircases are shown; the acquisition of each curve lasted for several hours, due to the low coincidence frequencies at higher threshold values: despite the PSAU module controlling the SiPM under test is endowed with overvoltage control for temperature variations, it is possible that during such long acquisition times environmental condition varied beyond the PSAU adjustment capabilities; a variation of the overvoltage during the acquisition time could explain infact the difference in the lenght of the staircases steps, suggesting that the more concentrated solution data set had been acquired with a slightly lower overbias.
Using Equation 7.7 multipeak spectra had been obtained, as illustrated in Figure 7.3; these objects had been treated with the same multipeak fit procedure explained in Chapter 5 to obtain the PCH distribution (where the zero-photon element has been obtained from the normalization condition 7.8) and results are shown in Figure 7.4. From the PCH, mean value and Fano factor of each distribution had been calculated and results are listed in Table 7.1.

In order to calculate the average number of molecules $\bar{N}$ in the excitation volume and the molecular brightness ϵ for the two concentations, both the momenta analysis and the PCH fit procedure had been considered.

[4]the optical density is a logarithmic unit measuring the attenuation of light through a medium: thus 1 optical density reduces the light intensity of an order of magnitude

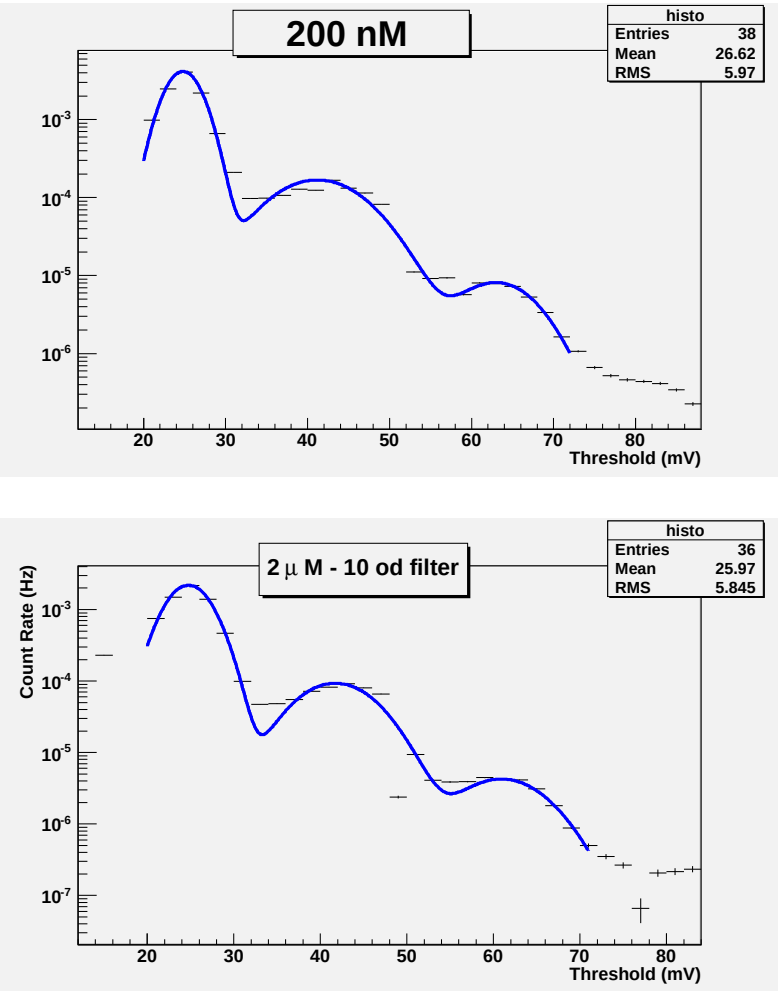

Figure 7.3: Multipeak spectra of the fluorescence obtained from the threshold scans using Equation 7.7; in upper panel spectrum from 200 nM concentated solution is shown, while in lower panel the one obtained from the 2 μM solution. Since staircase had been acquired with a 2 mV step, histograms have 2 mV large bins. Spectra had been fitted with a multi-gaussian function and areas of each peak have been used as PCH entries.

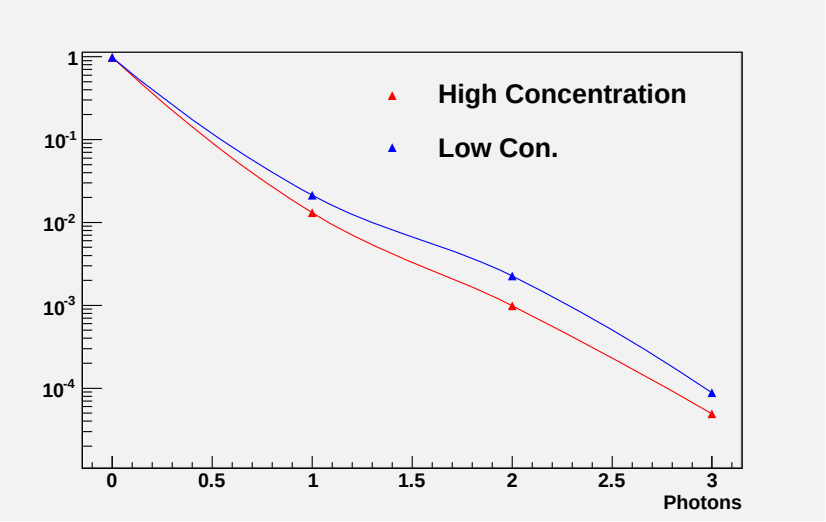

Figure 7.4: PCH obtained experimentally using Equation 7.7 and 7.8 on the threshold scan of the fluorescence emission of the 200 nM (in blue) and 2 μM (in red) rhodamine B concentrations; histogram values are given by the triangles, lines are just to guide the eye.

Concentration (nM)	$\langle k \rangle^{\star}$	Fano Factor
200	0.02625 $\pm$ 0.00012	1.16745 $\pm$ 0.00046
2000	0.01519 $\pm$ 0.00011	1.13458 $\pm$ 0.0007

Table 7.1: In this table the the mean value and the Fano Factor for the two distributions are listed. The mean value of the two solution are not exactely equal as expected: this is probably due to a worse positioning of the microscope, with a consequent worsening of the light focus.

7.5.1 Momenta analysis

The momenta analysis turned out to be of difficult applicability, given the aforementioned experimental conditions. Infact, solving simultaneously Equations 7.3 and 7.4 to find $\bar{N}$ and ϵ, an hyperbolic depenedence from the cross-talk parameter is made explicit, with a singularity in $x_t = (F-1)/(3-F)$, where F is the measured Fano factor.

This dependence appears to be strong, so that an extemely precise and accurate measurement of the cross-talk turns out to be necessary, in order to obtain a proper evaluation of the parameters of interest. As an exemple, in Figure 7.5 the mean number of molecules as function of the x_t parameter is shown, using

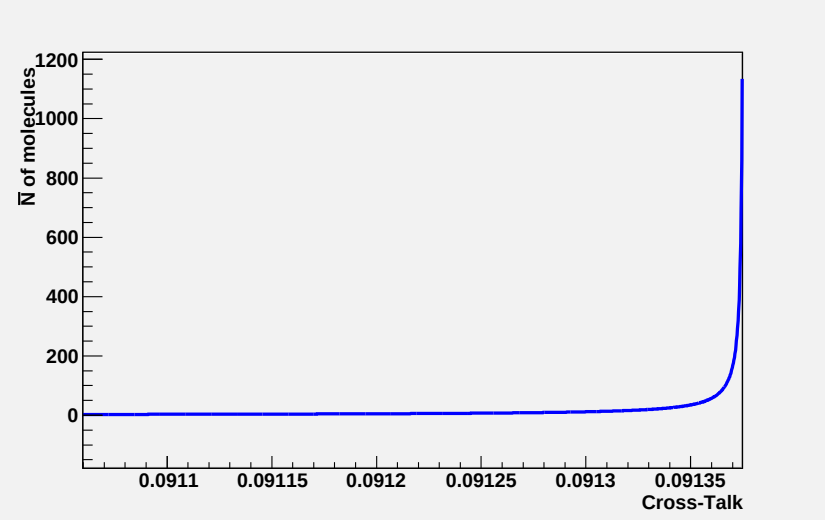

Figure 7.5: Mean number of molecules at varying cross-talk parameter, calculated solving simultaneously Equations 7.3 and 7.4 show an hyperbolic behaviour; extimation of $\bar{N}$ reach values consistent with experimental conditions ($\bar{N} > 1$) only in proximity of the singularity.

the $\langle k \rangle^{\star}$ and F values obtained with the 200 nM data set:

- as for the accuracy, cross-talk measurement must be a correct estimate of the cross-talk value during the acquisition process, which is hard to obtain in this experimental situation, due to the long time required for the data acquisition;
- even an accurate estimate must be extremely precise: it is clear that an indetermination regarding the fourth decimal place of the cross-talk value can cause a two order of magnitude indetermination on the evaluation of $\bar{N}$;

thus, even though a more accurate measurement of cross-talk can in principle be performed, such a precision is beyond our technical capabilities, making the momenta analysis a method of difficult applicability.

7.5.2 Histogram Fit

With the fit of the PCH, more consistent results had been obtained. Histograms obtained from the multipeak fit procedure had been fitted with a function $\Pi^{\star}(k;\epsilon,\bar{N},\langle n\rangle_{dcr},x_t)$, obtained adding to Equation 6.29 cross-talk and DCR contribution according to the procedure described in Chapter 5.
Due to the relatively small number of fitting points, to increase the number of degrees of freedom, the parameter repesenting the average number of dark counts has been fixed during the fitting procedure, for both data sets; results are presented in Table 7.2 and fit curves are shown in Figure 7.6.
Parameters obtained with the fit procedure show a general consistence with the experimental conditions. The difference of an order of magnitude in the mean number of particle in the excitation volume reflects the difference in concentration between the two samples; direct comparison with results obtained by other authors at similar concentrations (in [48], for exemple) is difficult because a measurement of the excitation volume (which obviously depends from the experimental conditions) could not have been performed[5].
The difference of about a factor ten in the moluclare brightness is consistent with the insertion of the neutral filter of one optical density. In particular, the fact that the molecular brightness of the 2 μM concentration set is found to be *more* than ten times lower, could be explained by a worsening of the light focusing with a consequent decrease in the absorption probability; a broader focus could also explain the slightly higher mean number of molecules in the excitation volume; this worsening could have been caused by some instability of the micropositioners used to assemble the setup.
Moreover, the difference between the cross-talk values is consistent with lower over biasing condition for the 2 μM set, suggesting that a worsening of the PDE could also have contributed to a lower molecular brightness.

Parameters	Concentrations (nM)	
	200	2000
$\bar{N}$	5.24 ± 0.03	71.70 ± 0.03
ϵ	$3.99 \times 10^{-3} \pm 2.4 \times 10^{-5}$	$1.536 \times 10^{-4} \pm 7 \times 10^{-7}$
x_t	$0.08085 \pm 5 \times 10^{-5}$	$0.0637 \pm 1 \times 10^{-4}$
$\langle n\rangle_{dcr}$	3.24×10^{-3}	3.24×10^{-3}

Table 7.2: Results for the fit of the PCH distributions. Errors listed are obtained from fit procedure. Results for mean number of particles and molecular brillance are consistent with what expected, even though there is not exactely a factor 10 between the parameters of the two data sets.

[5]Excitation volume is often obatined via FCS measurements with fluorophores of known diffusion coefficient.

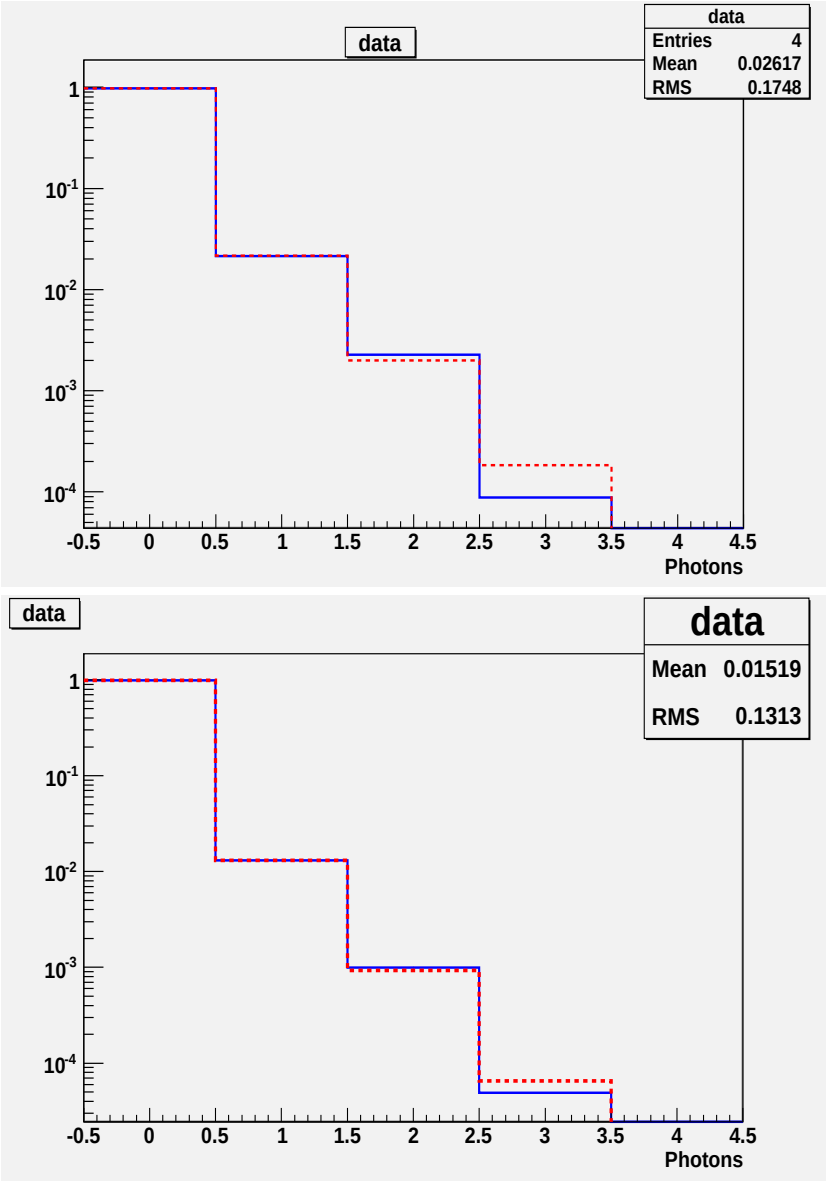

Figure 7.6: Fit of the experimental PCH for 200 nM concentation (upper panel) and 2 μM concentration (lower panel): experimental data are in blue continuous line, while fit results are in red dashed line.

7.6 Discussion

With this first feasibility study, it has been proven that SiPMs possess the capability of operate in a PCH experiment: through the necessary modelization of their response, elaborated in Chapter 5, it has been shown that the fit procedure of the experimentally obtained PCH brings consistent results, being capable of measure the mean number of molecules in the excitation volume; nonetheless further tests are needed in order to verify the real advantage SiPMs can bring in a practical experimental situation.
As previously stated in section 7.1, the main experimental improvement would be given by the possibility to perfrom reliable PCH and FCS measurement with a single data acquisition, measuring fluorescence emission *"pulse by pulse"* in a regime exceeding the single-photon; however, as explained in section 7.4, the performed studies could not test this possibility mainly due to the 48 MHz repetition rate of the laser light source.
Thus, next step in the feasibility studies would be given by performing PCH measurements with a reduced pulse frequency to the MegaHertz level (for exemple using a pulse-peaker device): under these conditions, it should be possible to perform the ordinary charge measurement on a pulse-by-pulse level. Moreover, this would allow fast and direct acquisition of the photon spectra; with fast acquisition time, a more accurate estimation of the cross-talk and DCR parameters can be performed.
Finally, last step of this study should be to test the possibility of also temporally autocorrelate charge measurements as in ordinary FCS experiments, for exemple adding a correlator as in [53] or [54].

Chapter 8

Conclusions

Starting from a description of the basic physical principles beyond the Silicon Photomultipliers functioning, this work presented an overlook on this technology and on some some of its possible applications.

Great part of this work took place within the framework of an international scientific and industrial collaboration with the aim of developing three radiation detectors using the SiPM technology; in order to find the optimal sensor for each application, an exhaustive protocol to provide a characterization of the performances of the main SiPM parameters has been provided, in particular concerning measurements of photo-detection efficiency, gain, dark count rate, optical cross-talk and their dependence from temperature variations.
The dependence of breakdown voltage from temperature has been confirmed to be very well described by a linear law and a robust method to measure its slope has been elaborated and applied to different models of SiPMs from different producers. This knowledge has been subsequentely employed in a partnership with CAEN, in the realization of the SP5600 General Purpose Power Supply and Amplification Unit module, providing it with a bias voltage adjustment feature, which allows to fix the SiPM over bias with varying environmental temperature.

In order to furtherly improve the knowledge on Silicon Photomultipliers, a deep study, both experimental and phenomenological, on their output signal has been carried on. A phenomenological model describing the statistics of Geiger-Müller avalanches for impinging photons with known probability distribution has been elaborated: this model takes into account the contribution given by the thermally generated avalanches and by the cross-talk, thus providing a model for the SiPM deviations from ideal bernoullian detection.
However, a complete treatment of the cell afterpulsing is still not included in this model, probably causing an overestimation of the dark count contribution: to provide a more consistent description of SiPM response, such an improvement of the model is necessary.

These models for SiPM response were necessary for the subsequent feasibility studies on the applicability of this sensors as detecting technology in Fluorescence Fluctuation Spectroscopy biophysical experiments, where parameters describing the system under study (proteins ligated with fluorophores in a solution) are measured from the deviations of the fluorescence intensity around its mean value. In these experiments, the use of fast (with a sub-nanosecond temporal resolution) detectors with an high photon number resolution can costitute an improvement of the experimental conditions, but a model for any sort of deviation from ideality is necessary.
Thus a Two-Photon Excitation setup has been commissioned and SiPM performances have been tested: the used sensor showed to possess the capabilities of performing an effective Photon Counting Histogram measurement, providing extimations of mean number of proteins in the excitation volume and the system molecular brightness.
Despite these well promising results, more studies still have to be performed: due to the experimental setup, data acquisition is long and data analysis is far from being trivial; moreover, present experimental conditions do not allow a pulse-by-pulse acquisition, which is essential in order to realize the idea of a combined FCS and PCH measurement. Thus, more effort is necessary in order to bring to FFS techniques a real experimental advantage with the use of SiPMs.

Bibliography

[1] G. Lutz. Silicon radiation detectors. *Nuclear Instruments and Methods in Physics Research Section A: Accelerators, Spectrometers, Detectors and Associated Equipment*, 367(1-3):21 – 33, 1995. Proceedings of the 7th International Wire Chamber Conference.

[2] A.V. Akindinov, A.N. Martemianov, P.A. Polozov, V.M. Golovin, and E.A. Grigoriev. New results on MRS APDs. *Nuclear Instruments and Methods in Physics Research Section A: Accelerators, Spectrometers, Detectors and Associated Equipment*, 387(1-2):231 – 234, 1997. New Developments in Photodetection.

[3] N. Wattimena. The CALICE tile hadron calorimeter prototype with SiPM readout: design, construction and first test beam results. In *ISSP 07*, 2007.

[4] Riccardo Fabbri. CALICE second generation AHCAL developements. In *The 2010 Linear Collider Workshop and the International Linear Collider meeting*, 2010.

[5] A. Heering, J. Rohlf, J. Freeman, S. Los, S. Kuleshov, and Y. Musienko. Performance of silicon photomultiplers with the CMS HCAL front-end electronics. *Nuclear Instruments and Methods in Physics Research Section A: Accelerators, Spectrometers, Detectors and Associated Equipment*, 576(2-3):341 – 349, 2007.

[6] Jim Freeman. Silicon photomultipliers for the CMS hadron calorimeter. *Nuclear Instruments and Methods in Physics Research Section A: Accelerators, Spectrometers, Detectors and Associated Equipment*, 617(1-3):393 – 395, 2010. 11th Pisa Meeting on Advanced Detectors - Proceedings of the 11th Pisa Meeting on Advanced Detectors.

[7] N. Otte, B. Dolgoshein, J. Hose, S. Klemin, E. Lorenz, R. Mirzoyan, E. Popova, and M. Teshima. The SiPM – A new photon detector for PET. *Nuclear Physics B - Proceedings Supplements*, 150:417 – 420, 2006. Proceedings of the 9th Topical Seminar on Innovative Particle and Radiation Detectors.

[8] Alberto Del Guerra, Nicola Belcari, Maria Giuseppina Bisogni, Gabriela LLosa, Sara Marcatili, Giovanni Ambrosi, Franco Corsi, Cristoforo Marzocca, Gianfranco Dalla Betta, and Claudio Piemonte. Advantages and pitfalls of the silicon photomultiplier (SiPM) as photodetector for the next generation of PET scanners. *Nuclear Instruments and Methods in Physics Research Section A: Accelerators, Spectrometers, Detectors and Associated Equipment*, 617(1-3):223 – 226, 2010. 11th Pisa Meeting on Advanced Detectors - Proceedings of the 11th Pisa Meeting on Advanced Detectors.

[9] C. Casella. The AX-PET Demonstrator: performance and first results, 7-10 June 2010. Siena, Italy.

[10] The CTA Consortium. *Design Concepts for the Cherenkov Telescope Array CTA*, chapter 8: CTA Telescope Technology. arXiv:1008.3703v2, May 2010.

[11] Gerhard Lutz. *Semiconductor Radiation Detector*. Springer, 1999.

[12] S.M. Sze. *Physics of Semiconductor Devices*. Wiley, 2007.

[13] J. Carlton Jackson. *Geiger-Mode Avalanche Photodiodes*. PhD thesis, National University of Ireland, 2003.

[14] A. G. Chynoweth and G. L. Pearson. Effect of Dislocations on Breakdown in Silicon p-n Junctions. *Journal of Applied Physics*, 29(7):1103–1110, 1958.

[15] C. R. Crowell and S. M. Sze. Temperature dependence of avalanche multiplication in semiconductors. *Applied Physics Letters*, 9(6):242–244, 1966.

[16] K. G. McKay. Avalanche Breakdown in Silicon. *Phys. Rev.*, 94(4):877–884, May 1954.

[17] A. G. Chynoweth. Ionization rates for electrons and holes in silicon. *Phys. Rev.*, 109(5):1537–1540, Mar 1958.

[18] R.J. McIntyre. A new look at impact ionization-Part i: A theory of gain, noise, breakdown probability, and frequency response. *IEEE Trans. Electron. Dev.*, 46:1623–1631, 1999.

[19] R. Van Overstraeten and H. De Man. Measurement of the ionization rates in diffused silicon p-n junctions. *Solid-State Electronics*, 13(5):583 – 608, 1970.

[20] A. Goetzberger, B. McDonald, R. H. Haitz, and R. M. Scarlett. Avalanche Effects in Silicon p—n Junctions. ii. Structurally Perfect Junctions. *Journal of Applied Physics*, 34(6):1591–1600, 1963.

[21] W.G. Oldham, R.R. Samuelson, and P Antognetti. Triggering phenomena in avalanche diodes. *IEEE Trans. Electron. Dev.*, 19:1056–1060, September 1972.

[22] W. G. Oldham, P. Antognetti, and R. R. Samuelson. New Method for Breakdown Voltage Determination in p-n Junctions. *Applied Physics Letters*, 19(11):466–467, 1971.

[23] A. Akindinov, G. Bondarenko, V. Golovin, E. Grigoriev, Yu. Grishuk, D. Mal'kevich, A. Martemiyanov, M. Ryabinin, A. Smirnitskiy, and K. Voloshin. Scintillation counter with MRS APD light readout. *Nuclear Instruments and Methods in Physics Research Section A: Accelerators, Spectrometers, Detectors and Associated Equipment*, 539(1-2):172 – 176, 2005.

[24] S. Cova, M. Ghioni, A. Lacaita, C. Samori, and F. Zappa. Avalanche photodiodes and quenching circuits for single-photon detection. *Appl. Opt.*, 35(12):1956–1976, 1996.

[25] Claudio Piemonte. A new Silicon Photomultiplier structure for blue light detection. *Nuclear Instruments and Methods in Physics Research Section A: Accelerators, Spectrometers, Detectors and Associated Equipment*, 568(1):224 – 232, 2006. New Developments in Radiation Detectors - Proceedings of the 10th European Symposium on Semiconductor Detectors, 10th European Symposium on Semiconductor Detectors.

[26] G. Ambrosi, P. Azzarello, R. Battiston, G. Di Lorenzo, M. Ionica, G.U. Pignatel, C. Piemonte, G.-F. Dalla Betta, and A. Del Guerra. Time resolving characteristics of hpk and fbk silicon photomultipliers for tof and pet applications. *Nuclear Instruments and Methods in Physics Research Section A: Accelerators, Spectrometers, Detectors and Associated Equipment*, 617(1-3):242 – 243, 2010. 11th Pisa Meeting on Advanced Detectors - Proceedings of the 11th Pisa Meeting on Advanced Detectors.

[27] G. Collazuol, G. Ambrosi, M. Boscardin, F. Corsi, G.F. Dalla Betta, A. Del Guerra, N. Dinu, M. Galimberti, D. Giulietti, L.A. Gizzi, L. Labate, G. Llosa, S. Marcatili, F. Morsani, C. Piemonte, A. Pozza, L. Zaccarelli, and N. Zorzi. Single photon timing resolution and detection efficiency of the irst silicon photo-multipliers. *Nuclear Instruments and Methods in Physics Research Section A: Accelerators, Spectrometers, Detectors and Associated Equipment*, 581(1-2):461 – 464, 2007. VCI 2007 - Proceedings of the 11th International Vienna Conference on Instrumentation.

[28] B. Dolgoshein, V. Balagura, P. Buzhan, M. Danilov, L. Filatov, E. Garutti, M. Groll, A. Ilyin, V. Kantserov, V. Kaplin, A. Karakash, F. Kayumov, S. Klemin, V. Korbel, H. Meyer, R. Mizuk, V. Morgunov, E. Novikov, P. Pakhlov, E. Popova, V. Rusinov, F. Sefkow, E. Tarkovsky, and I. Tikhomirov. Status report on silicon photomultiplier development and its applications. *Nuclear Instruments and Methods in Physics Research Section A: Accelerators, Spectrometers, Detectors and Associated Equipment*, 563(2):368 – 376, 2006. TRDs for the Third Millenium - Proceedings of

the 3rd Workshop on Advanced Transition Radiation Detectors for Accelerators and Space Applications.

[29] A.L. Lacaita, F. Zappa, S. Bigliardi, and M. Manfredi. On the bremsstrahlung origin of hot-carrier-induced photons in silicon devices. *IEEE Trans. Electron. Dev.*, 40:577–582, 1993.

[30] Roger Newman. Visible light from a Silicon $p - n$ Junction. *Phys. Rev.*, 100(2):700–703, Oct 1955.

[31] G. Sciacca, E. abd Condorelli, S. Aurite, S. Lombardo, M. Mazzillo, D. Sanfilippo, G. Fallica, and E.; Rimini. Crosstalk characterization in geiger-mode avalanche photodiode arrays. *IEEE Electron. Dev. Lett.*, 29:218–220, March 2008.

[32] Patrick Eckert, Hans-Christian Schultz-Coulon, Wei Shen, Rainer Stamen, and Alexander Tadday. Characterisation studies of silicon photomultipliers. *Nuclear Instruments and Methods in Physics Research Section A: Accelerators, Spectrometers, Detectors and Associated Equipment*, 620(2-3):217 – 226, 2010.

[33] Y. Du and F. Retière. After-pulsing and cross-talk in multi-pixel photon counters. *Nuclear Instruments and Methods in Physics Research Section A: Accelerators, Spectrometers, Detectors and Associated Equipment*, 596(3):396 – 401, 2008.

[34] A. Vacheret, G. J. Barker, M. Dziewiecki, P. Guzowski, M. D. Haigh, B. Hartfiel, A. Izmaylov, W. Johnston, M. Khabibullin, A. Khotjantsev, Y. Kudenko, R. Kurjata, T. Kutter, T. Lindner, P. Masliah, J. Marzec, O. Mineev, Y. Musienko, S. Oser, F. Retiere, R. O. Salih, A. Shaikhiev, L. F. Thompson, M. A. Ward, R. J. Wilson, N. Yershov, K. Zaremba, and M. Ziembicki. Characterization and Simulation of the Response of Multi Pixel Photon Counters to Low Light Levels. *ArXiv e-prints*, January 2011.

[35] A. Tarolli, G.-F. Dalla Betta, M. Melchiorri, A. Piazza, L. Pancheri, C. Piemonte, and N. Zorzi. Characterization of fbk sipms under illumination with very fast light pulses. *Nuclear Instruments and Methods in Physics Research Section A: Accelerators, Spectrometers, Detectors and Associated Equipment*, 617(1-3):430 – 431, 2010. 11th Pisa Meeting on Advanced Detectors - Proceedings of the 11th Pisa Meeting on Advanced Detectors.

[36] M. Bondani, A. Allevi, A. Agliati, and A. Andreoni. Self-consistent characterization of light statistics. *J. Mod. Opt.*, 56:226–231, 2009.

[37] L. Mandel and E. Wolf. *Optical Coherence and Quantum Optics*. Cambrige University Press, New York, NY, 1995.

[38] A. Agliati, M. Bondani, A. Andreoni, G. De Cillis, and M. G. A. Paris. Quantum and classical correlations of intense beams of light via joint photodetection. *J. Opt. B: Quantum Semiclassical Opt.*, 7:S652–S663, 2005.

[39] G. Zambra, M. Bondani, A.S. Spinelli, and A. Andreoni. Counting photoelectrons in the response of a photomultiplier tube to single picosecond light pulses. *Rev. Sci. Instrum.*, 75:2762–2765, 2004.

[40] M. Bondani, A. Allevi, and A. Andreoni. Light statistics by non-calibrated linear photodetectors. *Adv. Sci. Lett.*, 2:463–468, 2009.

[41] I. Afek, A. Natan, O. Ambar, and Y. Silberberg. Quantum state measurements using multipixel photon detectors. *Phys. Rev. A*, 79(4):043830, Apr 2009.

[42] Alessandra Andreoni and Maria Bondani. Photon statistics in the macroscopic realm measured without photon counters. *Phys. Rev. A*, 80(1):013819, Jul 2009.

[43] R. P. Van Der Marel and M. Franx. A new method for the identification of non-gaussian line profiles in elliptical galaxies. *Astrophisical Journal*, 407:525–539, 1993.

[44] F. T. Arecchi. Measurement of the statistical distribution of gaussian and laser sources. *Phys. Rev. Lett.*, 15:912–916, 1965.

[45] Petra Schwille. Fluorescence correlation spectroscopy and its potential for intracellular applications. *Cell Biochemistry and Biophysics*, 34:383–408, 2001. 10.1385/CBB:34:3:383.

[46] X. S. Xie and J.K. Trautman. Optical studies of single molecules at room temperature. *Annu. Rev. Phys. Chem.*, 49:441–480, 1998.

[47] S. Nie, , and R. N. Zare. Optical detection of single molecules. *Annu. Rev. Bioph. Biomol. Struct.*, 26:567–596, 1997.

[48] Y. Chen, J. D. Müller, P.T.C. So, and E. Gratton. The Photon Counting Histogram in Fluorescence Fluctuation Spectroscopy. *Biophysical Journal*, 77:553–567, 1999.

[49] Alberto Diaspro, Giuseppe Chirico, and Maddalena Collini. Two-photon fluorescence excitation and related techniques in biological microscopy. *Quarterly Reviews of Biophysics*, 38(02):97–166, 2005.

[50] Michael Gösch and Rudolf Rigler. Fluorescence correlation spectroscopy of molecular motions and kinetics. *Advanced Drug Delivery Reviews*, 57(1):169 – 190, 2005. Advances in Fluorescence Imaging: Opportunities for Pharmaceutical Science.

[51] M. Göppert-Mayer. Über Elementarakte mit zwei Quantensprüngen. *Annalen der Physik*, 401:273–294, 1931.

[52] W Denk, JH Strickler, and WW Webb. Two-photon laser scanning fluorescence microscopy. *Science*, 248(4951):73–76, 1990.

[53] K.M. Berland, P.T.C. So, and E. Gratton. Two-photon fluorescence correlation spectroscopy: method and application to the intracellular environment. *Biophys. J.*, 68:694–701, 1995.

[54] P. Schwille, U. Haupts, S. Maiti, and W.W. Webb. Molecular dynamics in living cells observed by fluorescence correlation spectroscopy with one- and two-photon excitation. *Biophys. J.*, 77:2251–2265, 1999.

[55] B. Saleh. *Photoelectron statistics, with applications to spectroscopy and optical communications*. Springer-Verlak, Berlin, 1978.

[56] L. Mandel. Sub-poissonian photon statistics in resonance fluorescence. *Opt. Lett.*, 4(7):205–207, 1979.

[57] L.N. Hillesheim and J.D. Müller. The photon counting histogram in fluorescence fluctuation spectroscopy with non-ideal photodetectors. *Biophys. J.*, 85:1948–1958, 2003.

[58] B. Huang, T.D. Perroud, and R.N. Zare. Photon Counting Histogram: One-Photon Excitation. *ChemPhysChem*, 5:1523–1531, 2004.

[59] T. D. Perroud, B. Huang, Wallace, M. I., and R. N. Zare. Photon Counting Histogram for One-Photon Excitation. *ChemPhysChem*, 4:1121–1123, 2003.